Analysis of Doppler spectra *obtained with* WSR-88D *radar from* non-stormy environment

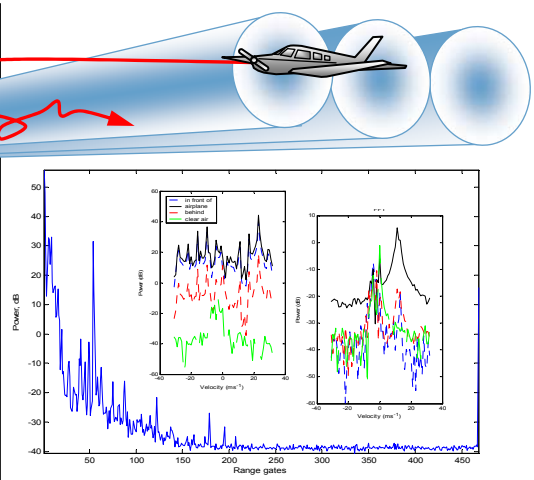

Svetlana Bachmann

February 2004

National Oceanic and Atmospheric Administration
National Severe Storm Laboratory
Norman, Oklahoma

University Of Oklahoma
Cooperative Institute for
Mesoscale Meteorological Studies

UNIVERSITY OF OKLAHOMA

GRADUATE COLLEGE

ANALYSIS OF DOPPLER SPECTRA OBTAINED WITH WEATHER RADAR IN NON STORMY ENVIRONMENT

A THESIS

SUBMITTED TO THE GRADUATE FACULTY

In partial fulfillment of the requirements for the

degree of

MASTER OF SCIENCE

By

SVETLANA MONAKHOVA BACHMANN
Norman, Oklahoma
2004

Preamble

Over the years NSSL has been providing technical information to the National Weather Service. This exchange had many forms, from formal reports and algorithms to consultation and supply of radar data in real time to the Weather Services Forecast Office. After the decision to evolve its network of WSR-88Ds to keep pace with emerging knowledge and technology the NWS provided a spare WSR-88D to NSSL. Hence, NSSL became the principal NOAA Laboratory for evolutionary and revolutionary enhancements of weather radar science and technology. At that time (mid nineties) Doppler Radar and Remote Sensing Research group committed to document in report form all significant innovations, changes, and results deemed of special value for operational applications regardless whether such writing was formally required. This is the fifteenth report in the series since 1997. It deals with identification of non meteorological scatterers in the power spectra of their echoes. Substantial improvement in data quality would ensue if such identification is possible, further it could lead to multipurpose use of weather radars. Data collected during the Homeland Security Experiment in Spring of 2003 are analyzed herein. Allen Zahrai led the team of engineers who designed the new processor and controls of the radar which enabled scanning strategies and recording of time series data. Mike Schmidt ably assisted with Richard Wahkinney made extensive modifications of microwave circuitry and controls.

This paper formed the MS thesis of Svetlana Bachmann whose committee members besides me were Dr. V. DeBrunner, Dr. R.J. Doviak and Dr. T. Yu. The NWS's Office of Science and Technology provided funds some of which were transferred to the Cooperative Institute of Mesoscale Meteorological Studies for support of Svetlana. Thus the report represents our continuous commitment to NWS and is part of a cumulative contribution to the Office of Science and Technology.

February 2004 in Norman

Dusan S. Zrnic

Acknowledgments

Many people have been of assistance in various parts of this project. My advisor Dr. Victor DeBrunner taught me to be hard-working and willful in a struggle for a solution. Dr. Dusan Zrnic's contribution is invaluable in this work, and I acknowledge him for his important ideas, discussions, and for directing me to the paths leading to the solutions. His energy inspired new ideas.

I also acknowledge the advice of Dr. Tian-You Yu and I appreciate his supportive, time-consuming review of my work. I am thankful for fruitful discussions with Dr. Dick Doviak. I acknowledge Dr. Sebastian Torres and Chris Curtis for sharing their experience in radar data acquisition and Matlab radar data processing. I value help of NSSL senior software engineers David Priegnitz and Dan Suppes for their help with the radar analysis tool, and the radar data. I appreciate the time and participation of Donald Burges, NSSL Assistant Director Chief in Warning Research and Development Division.

This work was performed while I was a graduate research assistant at the Cooperative Institute for Mesoscale Meteorological Studies (CIMMS). Finding was provided by the NWS Office of Science and Technology under the Nexrad Program Improvement theme. Further data collection was supported by the National Severe Storms Laboratory/NOAA and U.S. Army Biological and Chemical Defense Systems (U.S. Dept. of Defense). I enjoyed working at National Severe Storm Laboratory (NSSL) with all the nice and supportive people who work there. My great appreciation is to CIMMS, NSSL, and OU School of Electrical and Computer Engineering.

I want to thank my daughter Kristina for allowing me to work on this project.

Contents

Abstract

This thesis provides support in defining potential improvements to Doppler weather radar signal processing techniques by (1) understanding the characteristics of the non-weather scatterers, and (2) adjusting received phase-coded signal phase. The echo from point scatterers (airplanes and birds) in a non-stormy environment is investigated in the time and frequency domains. Further, it is compared to model simulations to build a background for differentiating these echoes from weather signals and to develop procedures for data censoring. The phase coded echo from a stationary point scatterer is examined to determine uncertainties in radar oscillator phase caused by the phase shifter in the WSR-88D radar. The phase shifter is part of a circuit for automatic calibration of the receiver and will be used to generate systematic phase codes for mitigating range velocity ambiguities.

1. Introduction

1.1. Motivation

Weather radars operated by the National Weather Service in the USA are joined in a network to provide spatially and temporally continuous coverage over the whole country. Advances in accuracy of radar signals would significantly improve the radar and radar network performances. Detected signals are processed with many assumptions to simplify interpretation of the echo and enhance features deemed important for identifying significant and/or hazardous phenomena. The results of interpretation are often based on previous observations and matched to the conceptual models. I identify that as a fuzzy approach, creating a blurry picture that is missing detailed information that could be important. There is always clutter in signals and it distorts the purposeful component of the signal. Getting rid of clutter, or compensating for the loss caused by clutter might be possible by applying appropriate filtering and enhancing techniques. To decide on the type of techniques suitable for one case or another it is necessary to accumulate information characterizing echoes and its behavior due to known conditions. My motivation is to study particular details in the echo signal with the goal of extracting more information that would help classify the echoes.

The primary goals of this research are: a) to acquire information from clear-air echoes obtained with an S-band (2-5 GHz 15-8cm) radar; b) to understand echo characteristics of point scatterers in clear-air; c) to create models simulating the echo; and d) to improve the interpretation of radar data by aggregating the information associated with the target solutions (the combination of range, azimuth, course, and velocity at any time) and the spectral signatures of the echoes. This information may

help to advance the radar performance by improving its signal processing techniques, and may assist in developing an approach for differentiating point scatterers. By surveying the echo signal features in time and frequency domains, I attempted to determine a physical principle that regulates the appearance of the echo signal and influences it. I verified the nature of the target signature occurrence and confirmed it mathematically. I investigated the behavior of the signals and characterized them.

1.2. Radar Background

The radar operator may either define a Volume Coverage Pattern (VCP) or interact with the radar's operating computer to define the scan characteristics. Many different VCPs that involve different scan strategies and sampling techniques are employed with the radars used for the meteorological observations. Examples of variables defining the VCP are (1) elevation, the antenna angle above horizontal; (2) antenna rotation rate in degrees per second; (3) Pulse Repetition Frequency (PRF); (4) number of pulses (M) that are transmitted along each radial. Radar transmits a beam of radio frequency energy in discrete pulses which propagate away from the radar antenna at the speed of light. The scatterers backscatter energy so that some of it returns to the radar. Radar pulse volume is defined by wavelength of the transmitted energy, the shape and size of the radar antenna, and the transmitted pulse width. The radar resolution volume determines the region in space that contributes most energy to the returned signal. The radar used in this work is described in Section 2.1. The radar has a narrow Gaussian-shaped beam pattern. Each pulse is mainly contained within a truncated cone, as shown in Figure 1.1. The transmitted beam assumes maximum power along the beam centerline. The half-power circle (Figure 1.1) is the locus of

points where the power of transmitted energy has decreased to one-half of the maximum power. The collection of such circles for all ranges defines a core, which is considered to effectively contain the radar beam. The beam-width is the angular width of the radar beam subtended by this half-power core.

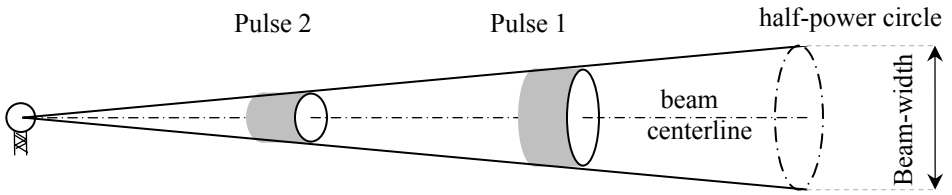

Figure 1.1: Radar beam geometry.
The maximum power of the beam lies along its centerline. Conceptual half-power circle defines the beam-width. All of the transmitted pulses have the same duration. Pulse 1 has a greater volume than pulse 2 because it is farther away from the radar.

Pulsed transmission is used to obtain range and motion information of the scatterer. Long pulses (4.7 μs) have more energy and can be used for probing scatterers at farther ranges but at lower pulse repetition times (PRTs). Short pulses (1.57 μs) can be transmitted at higher PRT and therefore are used to measure unambiguously larger velocities. Typical weather radar transmits megawatts of peak power. After the pulses (concentrated in a narrow beam) are transmitted the electromagnetic energy will be absorbed, diffracted, refracted, and reflected. Reflected from scatterers energy experiences additional absorption, refraction and reflection on the return trip back to the receive antenna. Thus, when a pulse is backscattered from scatterers, only a fraction of the transmitted power is incident on the receive antenna. The radar receiver is very sensitive and is capable of receiving powers as small as 10^{-14} W. The received signals are mixed with a reference signal of the intermediate frequency (57.6 MHz) and

amplified. The echo voltage V backscattered to the radar from a point scatterer has a phase ψ_e with respect to the transmitted pulse. The phase ψ_e from a stationary scatterer is time independent. If the distance between radar and scatterer changes, the phase also changes, creating a phase shift called the Doppler shift. Positive Doppler shift, corresponding to a negative radial velocity, indicates motion toward radar. Negative Doppler shift, related to positive velocity, shows motion of scatterers away from the radar.

The Doppler radar receiver has two synchronous detectors which detect in-phase I and quadrature-phase Q components of the echo signal V. According to Euler's relation the echo voltage can be represented by a two-dimensional phasor diagram in a complex plane (Figure 1.2). The successive values of I-Q samples are measured at equally spaced time intervals creating a time-series sequence.

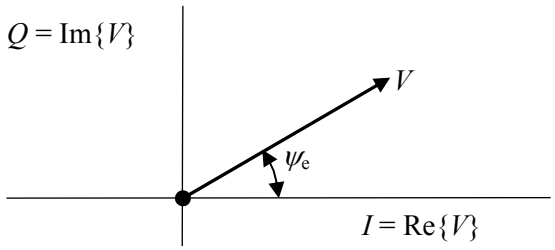

Figure 1.2: Phasor diagram.
The Doppler radar receiver detects in-phase I and quadrature-phase Q components of the echo signal V. I is the real part of the echo voltage V, Q is the imaginary part of V, and ψ_e is echo phase.

I-Q samples of backscattered energy at the same range location for a number of pulses (M) specified by the VCP are processed to generate spectral moments of one range location, as shown in Figure 1.3a. Collection of consecutive range gates makes a

radial. A radial of data may consist of either equally spaced *I*, *Q* samples, or spectral moments (Figure 1.3b). A cut is defined as a scan at a fixed elevation. Cut consists of many radials as shown in Figure 1.3c. Radar data usually include many cuts. Cuts can be scanned with different or constant settings. For example, cuts shown in Figure 1.3d are taken at different elevation angles. When nothing in the radar settings is changed from cut to cut the scan is continuous. Several cuts make a data file according to the VCP or other radar operator requirements.

1.3. Clear-air

Doppler shift allows creation of a picture of "traffic" within the atmosphere. The atmosphere-traffic includes (1) motion of air-masses (winds, clouds, vapor, dust, smoke, etc.), (2) interference from other radio equipment or the sun, (3) movement of aircrafts (airplanes, helicopters, balloons), and (4) passive and/or active displacement of biota (birds and airborne insects). I refer to the atmosphere free of clouds and precipitation as clear-air. Throughout the development of weather radar technology and science, radar echoes from non-precipitation sources have been referred to by several different names: angel echoes and clear-air echoes. These can occur as isolated point or small area scatterers, layers, or volumes of distributed scatterers. Clear-air echoes can appear granular, spotty. Current and recent literature indicates a widely held belief that the primary cause of clear-air echoes is biota. (For example: Campistron, 1975; Wilson, 1994; Rogers et al., 1991; Rabin and Doviak, 1989, and many others). In clear-air reflections can be caused by refractive index fluctuations, biota, aircrafts, and ground clutter. Clear-air echoes caused by point scatterers, e.g., birds, airplanes and ground clutter are investigated in this thesis.

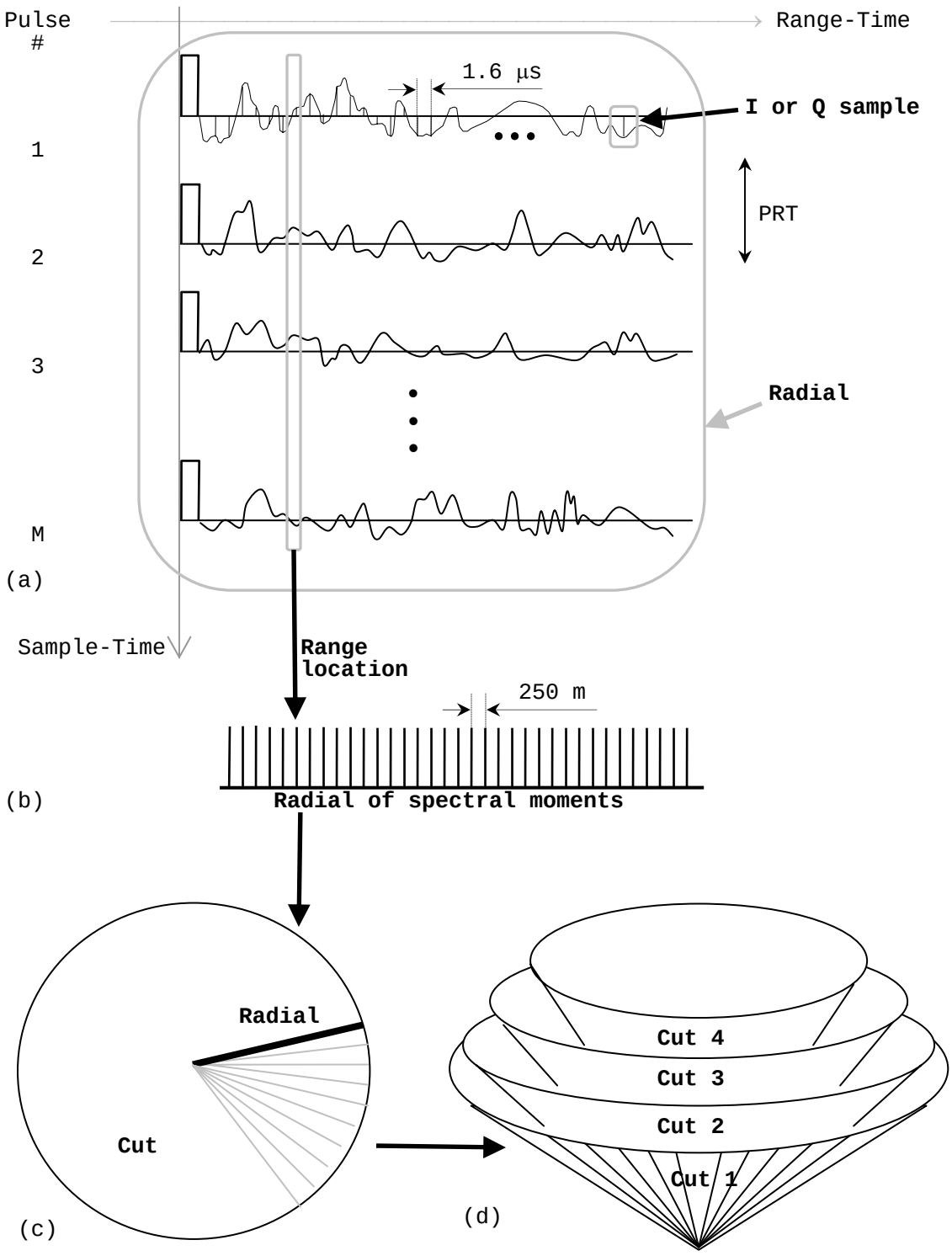

Figure 1.3: *I-Q* samples make the data.
(a) *I-Q* samples of backscattered energy for M pulses; (b) radial of spectral moments, (c) radials in a cut, (d) cuts in a VCP. Note that cuts could be taken at different elevation angles (as shown) or at the same elevation as defined by the VCP.

1.4. Ground Clutter

Ground clutter is the return from obstacles on the ground. The returns from ground scatterers are usually very large with respect to other echoes, and so can be easily recognized (Accu-Weather NEXRAD Dopplar Radar Information Guide, 1995). Ground-based obstacles may be immediately in the line of site of the main radar beam, for instance hills, tall buildings, or towers. Alternatively, the returns may be from objects, which although not directly within the field of view of the main radar beam, are present within one of the side-lobes of the radar beam. In this case, even though the side-lobe power is much lower than that of the main beam, the return may still be large due to the closeness of the obstacle, and/or its large cross section.

Clutter is desired to be mitigated in order to improve the radar performance. For weather radars, signals from biological scatterers, airplanes, and ground scatterers are undesirable; the exception might be signals from passively transported insects which map the motion of air. Contamination by birds is often a noisy signal covering entire low elevation sites and preventing useful weather observations.

1.5. Literature Review

Echoes in clear-air have been documented from early days of radar meteorology [16]. Birds have been implicated as sources of errors in wind profiling radars [14]. Even at close ranges, a narrow beam tracking radar can be affected by bird migration [11]. Recognition of birds in the Doppler radar spectra of surveillance radars should be possible from the beat frequency of the flapping wings [11], but this is not yet practical [16]. Specialized spectral processing with associated recognition algorithms would need to be developed [16].

The third base product of WSR-88D radars, Doppler spectrum width, has been called “the largely ignored step child of Doppler weather radar” [7]. The actual number of investigators regularly using radar to study birds has decreased significantly [11] due to difficulty and costs of experiments [11].

There are no solutions to completely eradicate the range and velocity ambiguity of weather echoes [10]. One of the approaches to reduce the ambiguities uses the frequency domain to separate overlaid echoes and assign each one a correct range [17]. The random phase coding [17], systematic $\pi/4$ and $\pi/2$ phase coding [18], and systematic SZ phase coding [10] techniques have been suggested for the recovery of spectral parameters of the overlaid first- and second- trip echoes. I will examine the phase coded echo from a stationary point scatterer to determine uncertainties in radar oscillator phase caused by the phase shifter in the WSR-88D radar.

2. Data Acquisition

2.1 Radar

KOUN (Figure 2.1) is a research WSR-88D (Weather Surveillance Radar-88 Doppler) radar that is managed and operated by the National Severe Storms Laboratory. The radar frequency is 2705 MHz. A WSR-88D system consists of the antenna, pedestal, radome, tower, klystron transmitter, receiver, minicomputer, signal processor, and radar product generator. The 10-cm wavelength (2.7-3.0 GHz) klystron transmitter transmits with a nominal peak power output of 750 kW. The radar operates with either short or long pulse. The short pulse-width of 1.57 μs is for pulse repetition

Figure 2.1: KOUN Doppler Radar WSR-88D used for data collection in this work.

frequencies (PRF) between 318 and 1304 Hz, and long pulse-width of 4.7 μsec is for PRFs between 318 and 452 Hz. The parabolic antenna has a diameter of 8.5 m (27.9 ft), an antenna main-lobe one-way 3 dB beam-width of approximately 0.95°, and a first side-lobe 27 dB below the main lobe. The signal transmitted by KOUN can be either linear horizontal polarization or simultaneous horizontal/vertical polarization.

2.2. Data Collection and Selection

Time series data were collected using KOUN on the following dates: 12/11/2002, 2/10/2003, 04/02/2003, 26/03/2003, 05/08/2003. Data sets are described in section 2.5. Data are reformatted and displayed on the prototype version of the Radar Analysis Tool (RRAT), which is developed at NSSL. Figure 2.2 shows a typical display of RRAT with plan-position indicator (PPI) on the right side, range-height indicator (RHI) on the top left, and Spectral View window on the lower left. The PPI window of RRAT can display velocity, reflectivity, or spectrum width with different zooming, color scale, and a great variety of options under the tab property. The spectral view of RRAT can be used to display the spectrum at a certain gate or in the gate with its 8 neighbors. The RHI window cursor moves simultaneously with the PPI cursor, showing the location of the gate in the vertical view of the radial and helping to estimate the 3-dimentional location of the resolution volume. The tab Cut shows the changes of data with time, animating the picture. This tool is a great help at browsing through a very large amount of data quickly, but sufficient time is required for loading the data prior to using it. Loading and processing the data may take tens of minutes depending on the size of the radar data file, but processed data can be accessed instantly with a great variety of displaying options. The RRAT was used to search for unusual spectra and unexplained

echoes, to get acquainted with the features of the data, and to choose interesting areas. A list of file names, cut numbers, and the azimuth angles and ranges of the areas of interest was recorded in order to keep track of and to prepare for extraction of the radials containing those areas.

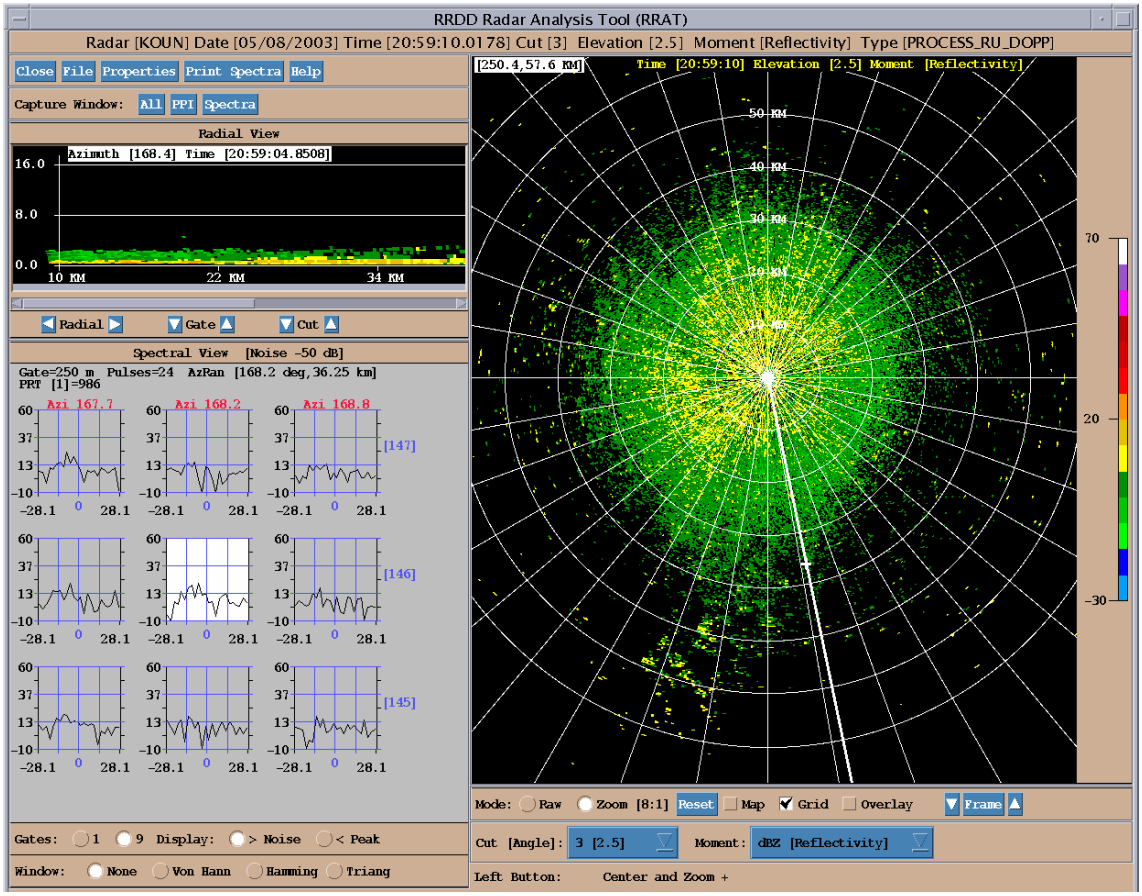

Figure 2.2: Example of the display of the Radar Analysis Tool (RRAT).
Top-left: range-height indicator; lower-left: spectral view window; right-half plan-position indicator; most-right: color-scale bar. Middle spectrum is from the location, marked with the cursor on a highlighted white radial.

2.3 Conversion into MATLAB

The routine RaidRead was developed at NSSL for splitting a raw radar data file into small portions of data and converting these into files of other formats, e.g., MATLAB format data files. A radar data file, consisting of a large number of radials

(N_r) at some number of cuts (N_c), is split into ($N_r \times N_c$) files, creating a separate data file for every radial in the original data. For example, to obtain an area found on March 26 2003 at 16:29, located at azimuth 174^o from the original radar data file r*aw_003_030326_162931.dat*, I used Routine RaidRead to search the DVD for the file name, selected radial, and time of the registered echo. RaidRead extracted radial 174.2^o at the specified time, and, on my request of the data type, converted it into the MATLAB data file with file name *raw_003_030326_162931986_102_02_048_1739.mat*. Both the radar data file name and MATLAB data file name provide information about the data. The description of the notation used for data file names is given below.

2.3.1. Radar data file name notation

The following notation is used by NSSL for the radar data file names:

ttt_num_yymmdd_hhmmss.dat,

where letters represent digits, and number of some letters corresponds to number of digits, with the following implication, *ttt* is the type of the data (raw or base), *num* is the experiment number, *yymmdd* is the date of the scan (year, month, day), and *hhmmssfff* is the time of the scan (hour, min, sec, fraction of sec).

2.3.2. MATLAB data file name notation

The following notation is used by NSSL for the MATLAB data file names:

ttt_num_yymmdd_hhmmssfff_vcp_cc_rad_azim.mat,

where *vcp* is the volume coverage patterns (VCP) that involve different scan strategies and sampling techniques, *cc* is the cut number, *rad* is the radial number, and *azim* is the azimuth angle of the radial (hundreds, tens, ones and tenths of degree).

2.4 Preprocessing

Each file with extension "*.mat*" consists of an array of complex data and a header. A header is a structured array with description of the data. One radial of MATLAB data has dimensions $N \times M$, where N is the number of bins (range gates) and M is the number of pulses. Each radial of data collected on 2/10, 4/02, and 3/26 has dimensions 468×64, and a radial of data from 5/09 has dimensions 592×24.

After reading and plotting many radials (Figure 2.3), I selected the radials with the most pronounced features, e.g., the strongest reflectivity for an airplane return, andcreated collections or batches of data several radials in size for further processing.

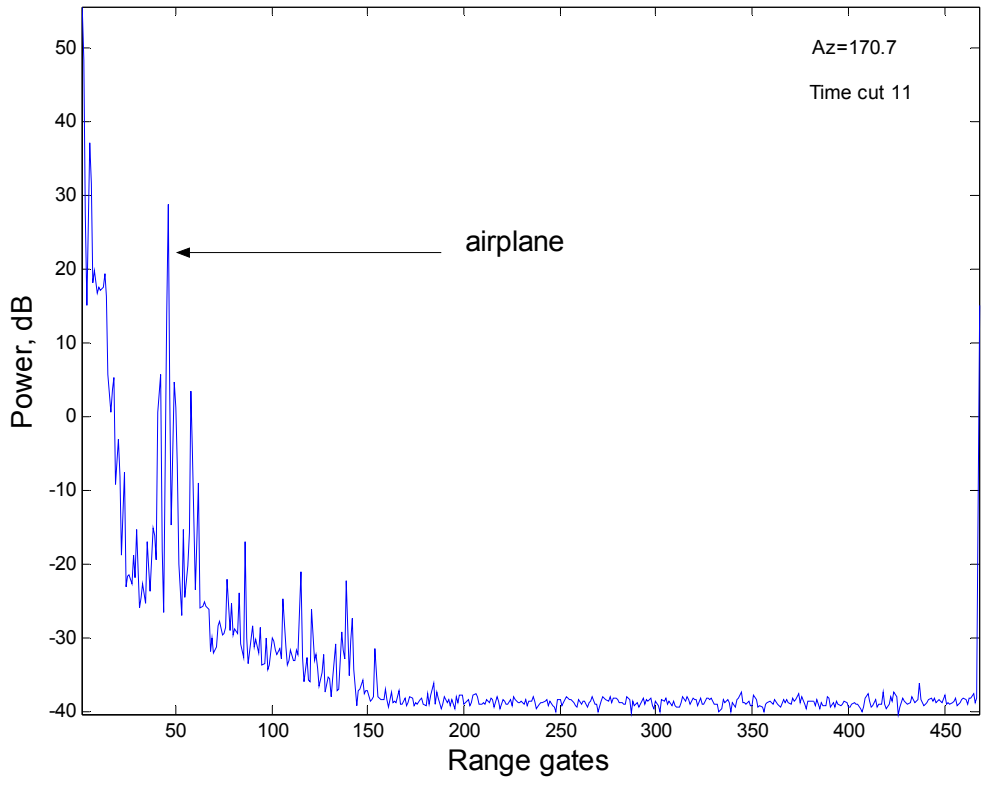

Figure 2.3: Returned power along one radial. The echo from an airplane is indicated. High powers at close ranges are from ground clutter.

The radials for single birds were chosen as described in Section 4.1. The radials for multiple birds were selected randomly (Section 4.3).

Most of the batches consist of neighboring or consecutive radials for several reasons. First, the discrete nature of sampling suggests that a scatterer could be located on the border of a sampling volume that would influence return from neighboring locations. Second, a strong return signal could appear at the adjacent range gates due to the spread of the range-dependent weighting function.

Figure 2.4 summarizes steps performed on a data file in the process of preparing it for analysis. The purpose of data preparation is to allow the loading of data in MATLAB with one command: `load('filename')`.

2.5 Data sets used in this work

2.5.1 Data sets from 2/10, and 4/02

The 2/10 and 4/02 data were obtained with a stationary antenna pointed at azimuth 306° and elevation 0.3°, radiating with PRT 780 μs. Data were collected for the Phase Shifter Test. One record of data consists of 468 consecutive (in range-time) I, Q samples. Each radial has 64 records of such data (64 pulses × 468 ranges). A file of data (*raw_010_030210_165638.dat*) consists of 100 radials (64 × 468 × 100). Both sets include data collected with and without phase coding. There was no precipitation on both dates. However the wind conditions were different: 3 ms^{-1} in February, and 10 ms^{-1} gusting to 15 ms^{-1} in April. This data is used in Chapter 5.

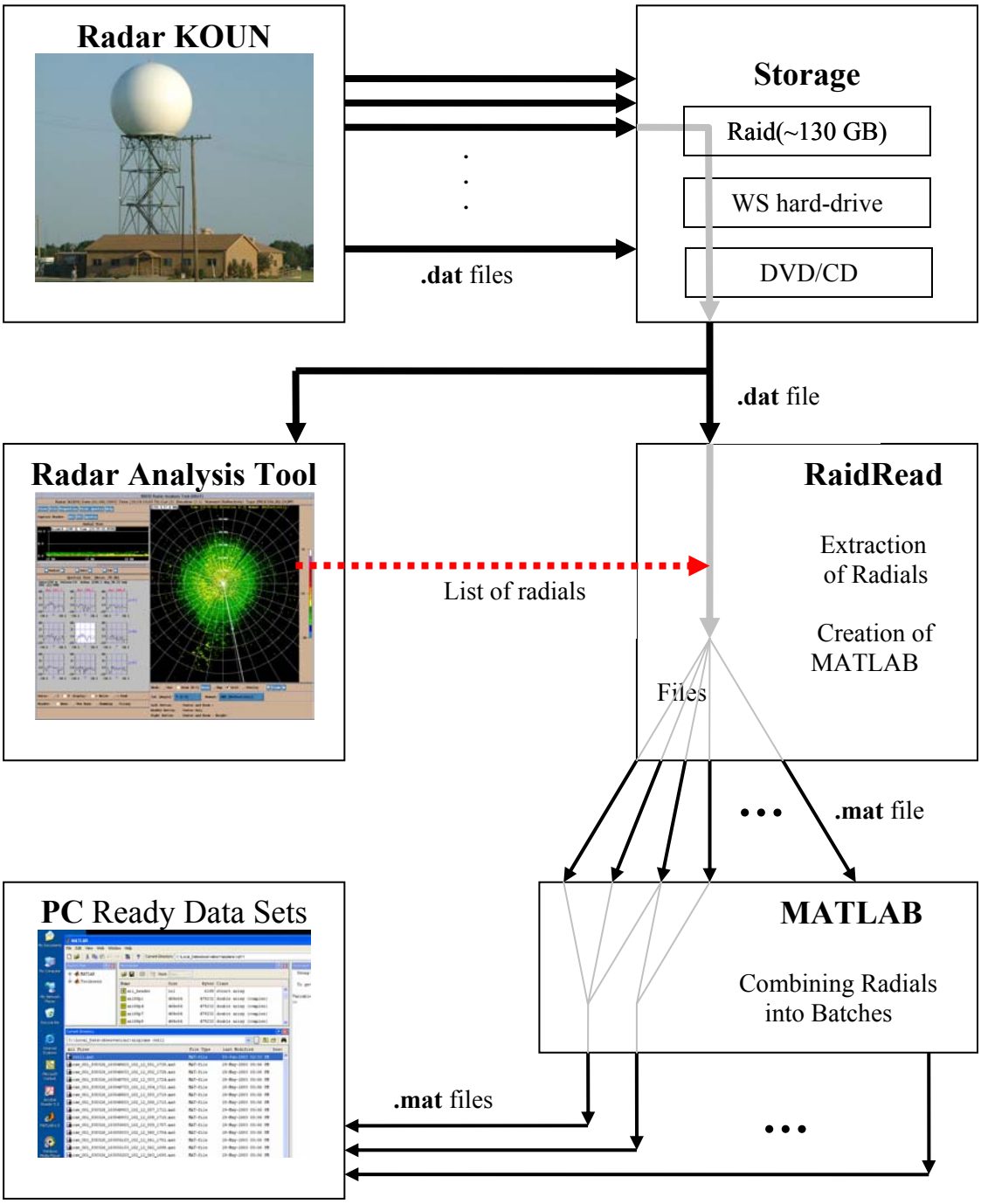

Figure 2.4: Data Preparation
The time series data were collected by KOUN radar. Collected data stored on Raid (~130GB), read by ReadRaid to a workstation hard-drive, and archived on DVD/CD. The files of raw radar data were explored by means of Radar Analysis Tool. MATLAB data files were created with RaidRead. MATLAB data files were composed into batches of consecutive radials and prepared for analysis.

2.5.2 Data set from 3/26

The 3/26 data were obtained with an antenna scanning a sector at azimuth angles 150° through 190°. All data were collected with PRT 780 μs, at constant elevation 1.5°. Data were collected for the Homeland Defense Radar Test.

There was no precipitation on March 26. I looked briefly at several hours of data and did not have any particular reason to prefer one data file over another. Every file consists of 20 time cuts 2.5 minutes long. A file (*raw_003_030326_102921.dat*) with data collected from 10:29 until 10:32 was selected. Similar results were found from the rest of files. Figure 2.5 shows reflectivity and velocity PPI of RRAT from one time cut of the data.

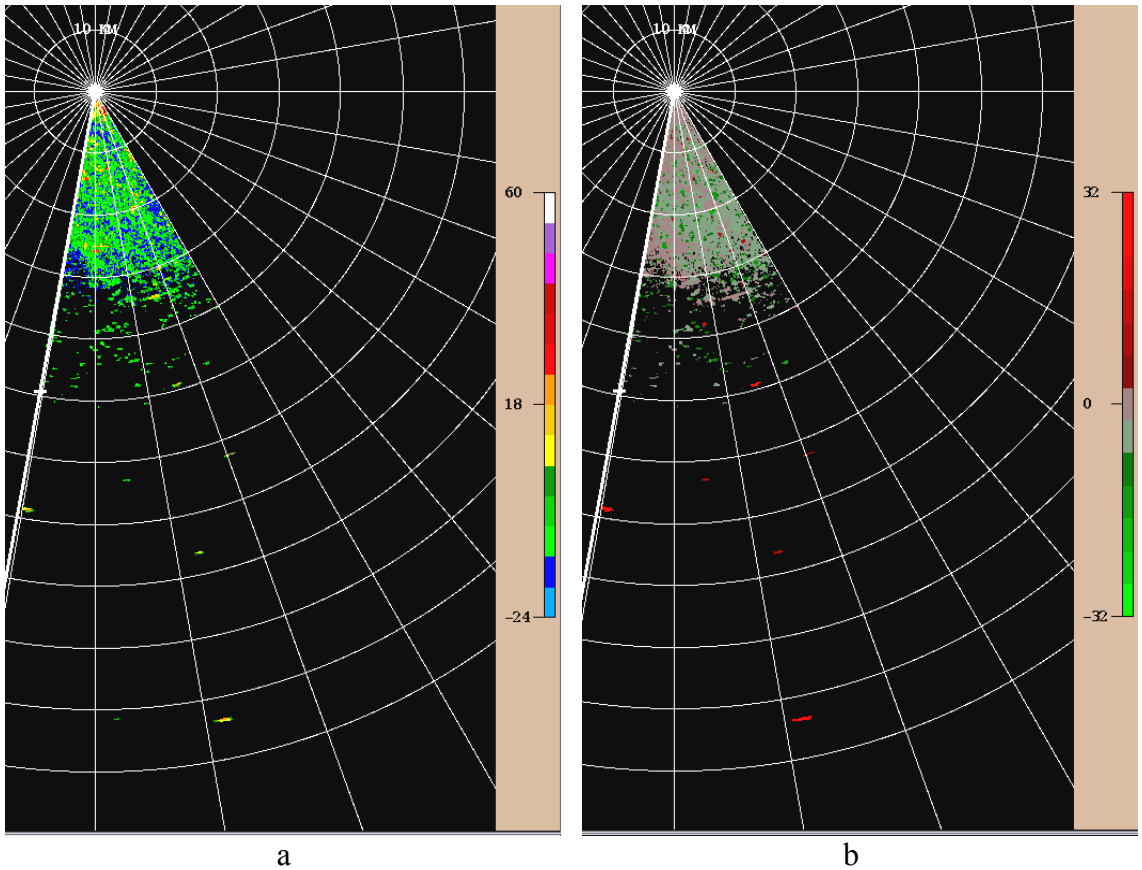

a b

Figure 2.5: One cut of data 3/26: (a) Reflectivity, (b) Velocity.
Note that range rings here are 10 km apart.

PRT determines maximum unambiguous range and maximum unambiguous velocity. Maximum unambiguous range R_{max} is 117 km, calculated according to the formula

$$R_{max} = c\, T_s / 2, \tag{2.7.1}$$

where c is the speed of light ($c = 3\times10^8$ ms^{-1}), T_s is PRT. Maximum unambiguous velocity v_{max} is 32.05 m s^{-1}, found according to the formula

$$v_{max} = \frac{\lambda}{4 \cdot PRT}, \tag{2.7.2}$$

where λ is the wavelength ($\lambda = 10$ cm).

Echoes from aircrafts, birds, insects, and ground clutter were expected in this data set. Echoes found in this data are summarized in Table 2.1. Each row describes the attributes of echoes found in the scan specified in column Range. The echo region is described by its shape and values of its reflectivity (Z) and velocity (v). Assumption on the type of echo is made according to its location (range) and description (shape, reflectivity and velocity values simultaneously with the neighborhood evaluation). Tracking several aircraft, I found the airplane flying for the Homeland Security Test. I focus attention on this so-called Airplane-1, and another unknown Airplane-2 in Chapter 3. Data with bird signatures is examined in Chapter 4.

Note that the category Airplanes in Table 2.1 includes a group Jet Airplanes. The Jet Airplanes group can be differentiated because of the large velocities that could be estimated from time-cut animation (tracking) and due to the high altitudes of these strong point scatterers.

Table 2.1: Echoes in clear-air scan 3/26.

Range	Echo Description		Assumption
	Shape	Reflectivity and Velocity	
Less then 5 km	Area	*Z*: high (20 to 40 dBZ) *v*: zero	Ground Clutter: Buildings, Water-towers, Trees
Less then 30 km	Large area (most of the scan)	*Z*: below 0 dBZ *v*: in the range 0 to 5 ms^{-1}	Wind blows toward the radar from south – south-east
	Point	*Z*: high (30 to 40 dBZ) *v*: zero	Ground Clutter: TV and Radio Towers
	Point and small area	*Z*: weaker (less then 10 dBZ) *v*: with non-zero, and non-wind values	Birds and Insects
15-30 km	Point	*Z*: 30-40 dBZ *v*: a lot different from surroundings	Airplanes
More then 30 km	Point	*Z*: 10-30 dBZ *v*: non zero velocities	Jet Airplanes
At different ranges	Point and small area	*Z*: weak (less then 10 dBZ) *v*: non-zero, and non-wind values	Birds and Insects

2.5.3 Data set from 5/08

The data from 5/08 were obtained with a full 360° scan of rotating and rising antenna. One file of data (*raw_005_030509_015646.dat*) consists of 14 cuts at different elevation angles from 0.1° to 19.5° as shown in Table 2.2.

On 8 May 2003, after a tornadic super-cell, biological scatterers lighted up KOUN displays for several hours between 2-5 UTC (9 May 2003). The time series data files were taken at about 2 UTC on May 9 2003, or at 10 PM of May 8, local time.

Table 2.2: Elevation Angles and PRT of different cuts of data 5/08

Cut	0	1	2	3	4	5	6	7	8	9	10	11	12	13
Elevation, °	.1	.5	1.5	2.5	3.5	4.5	5.5	6.5	7.5	8.7	10	12	14	19.5
PRT	Long			Short 986.67 μsec										

The return from the birds would be easier to see from the pulses sent with short PRT and at low elevation angle. Cut 03 is taken at the lowest elevation (2.5°) with shorter PRT. The reflectivity PPI of cut 3 is shown in Figure 2.2. Maximum unambiguous range R_{max} is 148 km. Maximum unambiguous velocity v_{max} is 25.3 m s^{-1}. This data is analyzed in Chapter 4.

3. Airplanes

The track-while-scan (TWS) systems deployed on the military radars use the combination of range, azimuth, course, and speed at any one time, known as the target's solution, to predict possible location of the target at the next observation. During each antenna sweep, the system attempts to correlate all returns with existing tracks. The TWS systems may confuse two different targets if their tracks cross each other. This motivated my research of the target signatures. The purpose of this chapter is to extract information from the available radar data containing airplane echoes, with an intention to discover a systematic structure in the echo spectra that possibly contains information characterizing the airplane. The approach involved investigation of the reflectivity, velocity, and spectra patterns of airplane returns, simulation of discovered features, and verifying results by the actual available information. A main goal is to find distinguishable features that can define an airplane signature and ultimately remove these from weather echoes.

3.1 Tracking

Airplane-1 was flying in the center of the scanned sector at ranges from 9 to 15 km. It was moving north toward the radar at the time of cuts 0 through 15, then turned east and started moving south, away from the radar. Airplane-2 entered the volume of the scan from the west at the time of the 10th cut at a range of approximately 9 km and kept flying north-west, gradually turning north, as shown in the radar trajectory Figure 3.1. The locations of the airplanes at different time cuts are tracked and given in the columns Range and Azimuth of Table 3.1 for Airplane-1 and Table 3.2 for Airplane-2. Both airplanes are at the same range about 10 km south from the radar during the 13th

Table 3.1: Reflectivity factors for Airplane-1

Cut	Time t (h:m:s)	Target Range r (km)	Azimuth Angle θ (°)	Beam Height h (m)	Reflec-tivity Z (dBZ)	Equivalent Reflectivity Z_e (mm^6m^{-3})	Reflectivity Per Volume $\eta\times10^9$ ($mm^6m^{-3}m^{-4}$)	Cross section σ_b (m^2)
0	10:29:21	14.63	172.5	383	46.5	44668	127.13	0.998
1	10:29:33	14.36	172.7	376	49.0	79433	226.06	1.710
2	10:29:39	13.87	172.1	363	56.0	398107	1133.01	7.995
3	10:29:48	13.60	172.7	356	47.5	56234	160.04	1.086
4	10:29:56	13.12	171.7	343	50.5	112202	319.32	2.016
5	10:30:03	12.86	172.3	337	48.5	70795	201.48	1.222
6	10:30:10	12.59	171.3	329	44.5	28184	80.21	0.466
7	10:30:19	12.10	171.9	317	44.0	25119	71.49	0.384
8	10:30:26	11.87	171.0	310	49.5	89125	253.65	1.311
9	10:30:34	11.63	171.4	304	43.0	19953	56.78	0.282
10	10:30:42	11.13	170.6	291	43.5	22387	63.71	0.290
11	10:30:50	10.91	170.8	286	42.5	17783	50.61	0.221
12	10:30:57	10.39	169.8	272	43.0	19953	56.78	0.225
13	10:31:05	10.13	170.4	265	40.0	10000	28.46	0.107
14	10:31:12	9.87	169.6	258	34.0	2512	7.15	0.026
15	10:31:21	9.35	169.8	244	24.0	251	0.71	0.002
16	10:31:28	9.36	167.3	245	35.0	3162	9.00	0.029
17	10:31:36	9.60	166.6	251	40.5	11220	31.93	0.108
18	10:31:43	9.87	165.8	258	42.0	15849	45.11	0.161
19	10:31:50	10.35	167.4	271	46.0	39811	113.30	0.445

Table 3.2: Reflectivity factors for Airplane-2

Cut	Time t (h:m:s)	Target Range r (km)	Azimuth Angle θ (°)	Target Height h (m)	Reflec-tivity Z (dBZ)	Equivalent Reflectivity Z_e (mm^6m^{-3})	Reflectivity Per Volume $\eta\times10^9$ ($mm^6m^{-3}m^4$)	Cross section σ_b (m^2)
8	10:30:26	9.6	190.2	251	42	15849	45.11	0.233
10	10:30:42	9.91	187.7	259	44	25119	71.49	0.325
11	10:30:50	9.95	188.2	260	39	7943	22.61	0.099
12	10:30:57	10.2	184.6	267	58	630957	1795.69	7.110
13	10:31:05	10.14	184.3	256	53	199526	567.85	2.137
14	10:31:12	9.87	181.5	258	53	199526	567.85	2.029
15	10:31:21	9.58	181.3	250	39	7943	22.61	0.073
16	10:31:28	9.35	178.7	244	43	19953	56.78	0.183
17	10:31:36	9.11	178.9	239	45	31623	90	0.304
18	10:31:43	8.61	178.4	225	47	50119	142.64	0.510
19	10:31:50	8.36	179.3	219	50	100000	284.6	1.118

time cut as indicated in Figures 3.2a and 3.2b. To track the airplanes the following steps were performed. The position of the strong point reflectivity associated with non-zero velocity at one time cut was noted. The next time cut was searched for a matching point, which is assumed to be located at some range and azimuth angle close to the location of previously registered point. The obtained points were connected as shown in Figure 3.1, and the solid lines show the paths of airplanes as indicated. Numbers 0 through 19 near the data points show time cuts.

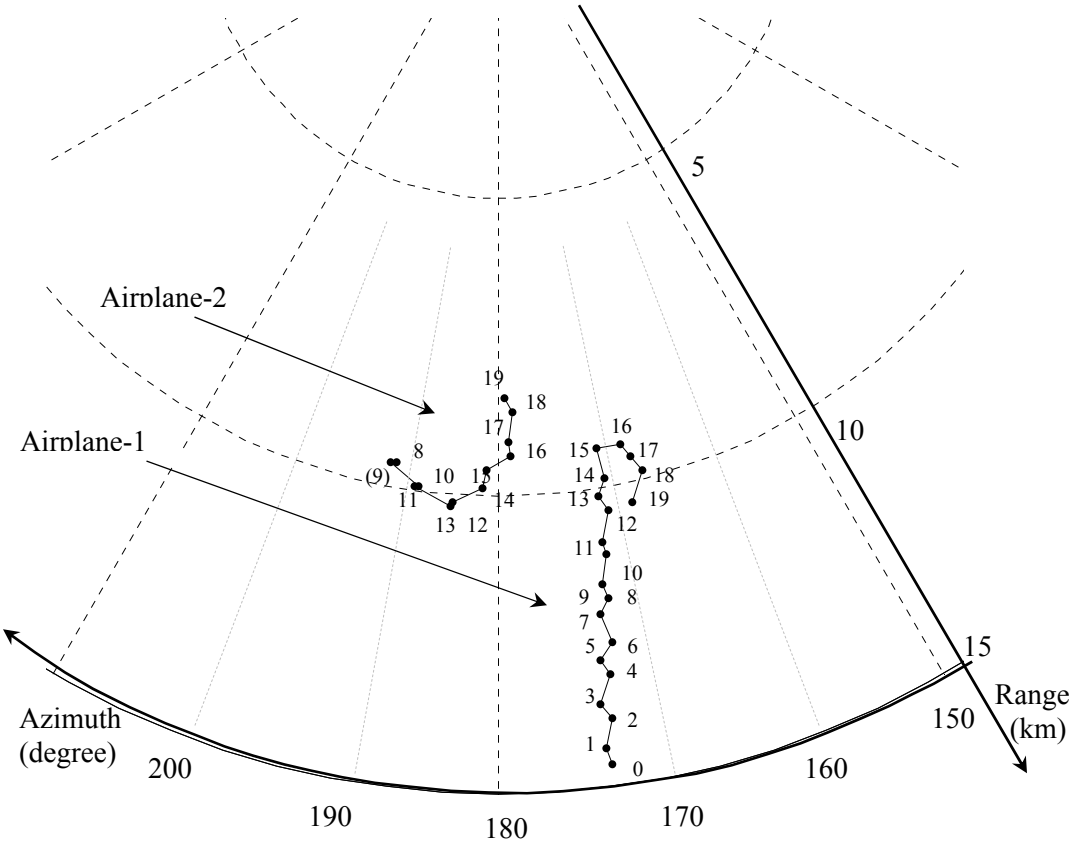

Figure 3.1: Trajectory of the airplanes.
The radar is located above the figure. Axis range shows the distance from the radar. Airplane-1 is flying toward the radar for most of its path. Airplane-2 is turning. At the 13th time cut both airplanes are located at the same range. A 1° azimuth angle corresponds to 261.8 m at a range of 15 km, and to 157.1 m at 9 km range.

The oscillations in the paths of the airplanes in Figure 3.1 are likely due to the backlash of the antenna that occurs during scanning a sector back and forth as opposed to the full 360° scan. Backlash is caused by the lag in gears, servo mechanism and encoders. The lag is not fully compensated, and hence shows as an offset between azimuths obtained in clockwise and counter-clockwise motion. In some cases the oscillations increased because of inaccurate reading of the data from the computer screen (Figure 3.2). Data points 0 through 19 were read from reflectivity PPI, similar to the one shown in Figure 3.2a. Every numbered point is associated with the center of the highest reflectivity, estimated by eye, as explained in Figure 3.3. In this figure a part of the reflectivity PPI with the Airplane-1 echo is magnified to show in detail pixels corresponding to radar resolution volumes. One pixel is a rectangle 250 m long and 0.5° wide. Several pixels circled in Figure 3.3a show more than 30 dB reflectivity

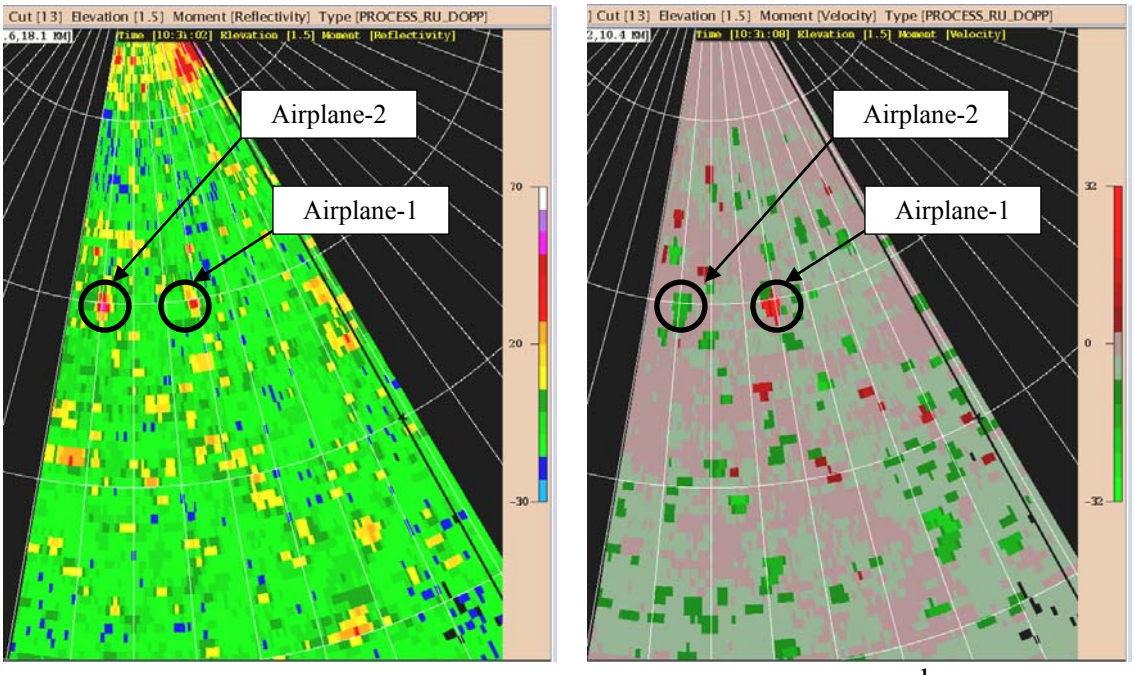

a b

Figure 3.2: 13th time cut of data 3/26 on the PPI of RRAT:
(a) Reflectivity. (b) Velocity. Circles near 10 km range ring are used to show the locations of Airplane-1 and Airplane-2. Note that range rings here are 5 km apart.

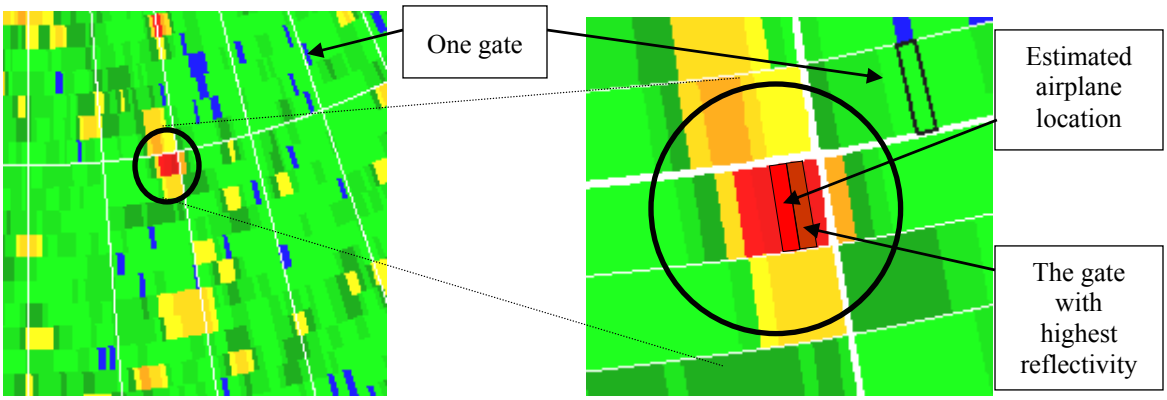

Figure 3.3: Estimation of an airplane location from the reflectivity PPI.
A part of reflectivity PPI with circled airplane echo, magnified to show gates in detail. The color-scale is the same as in Figure 3.2a. Pixels in the center of the circle have reflectivity values more then 40dBZ. The pixel to the right of center shows the largest value of reflectivity. Nevertheless, the center of the high reflectivity area is estimated to be the airplane location. It is done to avoid possible ground clutter and/or additional scatterer contamination

values. Four adjacent pixels in a row have values more then 40 dB; therefore, this row is likely to be the range of the airplane. Figure 3.3b shows that the pixel with highest reflectivity (darkest color) is not in the center of the area. However, the center of the area of high reflectivity values is estimated to be the azimuth angle of the airplane location. The reading approximation introduces ±250 meters error.

3.2 Speed estimation

3.2.1 Doppler shift and velocity of a target

The phase of an echo ψ_e from a stationary scatterer is time independent [3]

$$\psi_e \equiv -4\pi r/\lambda + \psi_t + \psi_s, \qquad (3.2.1)$$

where λ is the transmitted energy wavelength (m), r is the scatterer range (m), ψ_t is the transmitter phase shift (radians), and ψ_s is the phase shift upon scattering (radians). When the distance between radar and scatterer changes in a time dt, the phase also changes, creating a phase shift called the Doppler shift

$$\omega_d = \frac{d\psi_e}{dt} = -\frac{4\pi}{\lambda}\frac{dr}{dt} = -\frac{4\pi}{\lambda}v_r\,, \tag{3.2.2}$$

where v_r is the velocity of a scatterer, and ω_d is the radial Doppler frequency (radians per second). Knowing that $\omega_d = 2\pi f_d$, where f_d is the Doppler frequency in Hz, (3.2.2) can be rewritten as

$$f_d = -2\,v_r/\lambda\,. \tag{3.2.3}$$

Positive Doppler shift, corresponding to a negative radial velocity, indicates motion toward the radar. Negative Doppler shift, related to positive velocity, shows motion of a scatterer away from the radar. Signal is sampled at intervals T_s, so the phase change of the echo $\Delta\psi_e$ over the interval T_s is a measure of the Doppler frequency. From the Nyquist sampling theorem, to recover all Fourier components of a periodic signal, it is necessary to sample more than twice as fast as the highest frequency. The Nyquist frequency f_N, a frequency above which a signal must be sampled to assure its full reconstruction, is $(2T_s)^{-1}$. Therefore, all Doppler frequencies between $\pm f_N$ would indicate a correct Doppler shift, and frequencies higher then f_N are ambiguous with those between $\pm f_N$. To avoid ambiguity the radial velocities must be within the limits of $\pm v_{max}$. Note a zero velocity will be observed when a scatterer moves in a direction perpendicular to the radar beam.

3.2.2 Velocity of airplanes

The antenna scanned 20 cuts in 2 minutes 26 seconds. The time between two consecutive cuts is 5 seconds for an even-odd-pair and 10 seconds for an odd-even-pair. The time between every consecutive-odd or consecutive-even pair of cuts is 15 seconds. Speeds of airplanes may vary from cut to cut. The radial velocities of airplanes were

estimated in two ways. One is roughly from the display (PPI) and the other is from the reconstructed trajectory. The two estimates of the 13th cut are shown in Table 3.3.

Table 3.3: Estimated speeds of airplanes in terms of radial velocity at the 13th time cut.

	Airplane-1		**Airplane-2**	
Radial Velocity	From Trajectory, ms^{-1}	From PPI, ms^{-1}	From Trajectory, ms^{-1}	From PPI, ms^{-1}
Cut 13	Toward, 40	Away, 24 or toward, 40	Toward, 15	Toward, 13

A radial velocity can be thought of as a projection of a 3-dimensional velocity vector (range-height-azimuth) on the beam axis. Therefore, the actual speed of an airplane is greater than the radial velocity. The velocity value displayed on PPI for Airplane-2 agrees with that estimated from the trajectory. As for Airplane-1, there is a strong disagreement. The PPI velocity of Airplane-1 is 24 ms^{-1}, and for some cuts is even smaller, e.g. about 16 ms^{-1}. Moreover, according to the value of the PPI velocity, Airplane-1 is moving away from the radar, which contradicts the estimated trajectory. The velocities are aliased due to relatively small span of unambiguous velocities from –32 ms^{-1} to 32 ms^{-1}. The Airplane-2 velocities lie within the unambiguous interval. Figure 3.4a shows a velocity wheel with $v_{max} = \pm 32$ ms^{-1}, and the black arrow pointing to 24 ms^{-1}. It is not possible to determine whether this arrow rotated clockwise or counter-clockwise from zero to stop at 24 ms^{-1}. Figure 3.4b shows the same wheel as in Figure 3.4a, but with velocity values from 0 to negative $2v_{max}$. It is easy to see from Figure 3.4 that positive 24 ms^{-1} dealiases into negative 40 ms^{-1}. Moreover, 40 ms^{-1} is not necessarily the correct answer. It is unknown how many times the arrow circled

before it stopped, or how many times the velocity aliased. The true velocity of a scatterer v can be found mathematically as

$$v = -(2nv_{max} - v_{observed}), \tag{3.2.4}$$

where n is a positive or negative integer, $v_{observed}$ is the observed aliased velocity of a target. v_{max} is positive for displayed positive velocities and negative for displayed negative velocities. According to formula (3.2.4) any of the following values could be the radial velocity of Airplane-1 during the 13th time cut: {–24, –88, –152, …}, or {40, 104, 168, …} ms^{-1}. Assuming that the speed of a small airplane is less then 64 ms^{-1}, and knowing that the airplane stayed at the same height and the direction of the flight was toward-radar, the radial velocity of Airplane-1 during the time of the 13th cut

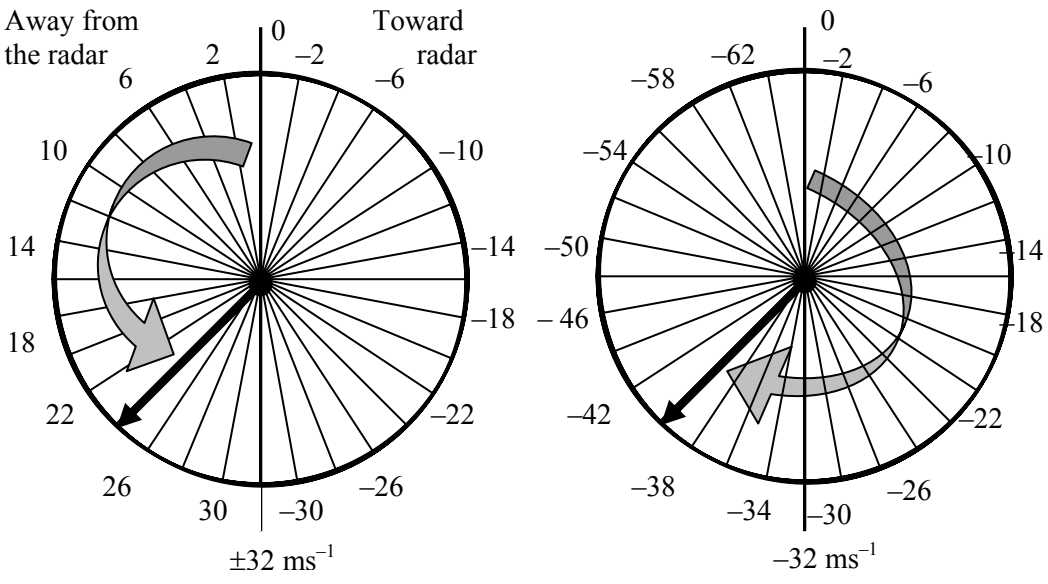

a b

Figure 3.4: Illustration of the velocity folding.
(a) Velocity wheel with $v_{max} = \pm 32$ ms^{-1}. Positive velocities on the left side of the clock indicate motion away from the radar. Negative velocities on the right side of the clock indicate motion toward radar. The black arrow points to positive 24 ms^{-1} with the positive sign indicating away-from-radar motion.
(b) Velocity wheel with v in the range from –0 to –64 ms^{-1}. The black arrow is at the same position as on the wheel in (a). It points to negative 40 ms^{-1}, indicating toward-radar motion.

is estimated to be 40 ms^{-1}. The actual speed of Airplane-1 can be estimated geometrically from its trajectory to be between 40 and 55 ms^{-1}. However, the speed of Airplane-2 cannot be estimated geometrically because the change of the altitude of its flight is unknown. The 2-dimensional speed (range-azimuth) of Airplane-2 is about 55 ms^{-1}.

3.3 Radar cross section of airplane

The reflectivity Z in RRAT is found according to the weather radar equation for distributed scatterers. However, a distant airplane is a point-scatterer, not a distributed scatterer. The reflectivity should be recalculated. Reflectivity for distributed scatterers Z (dB) is converted from the logarithmic scale into the equivalent reflectivity Z_e (mm^6m^{-3}) according to the formula

$$Z_e = 10^{\frac{dBZ}{10}}. \tag{3.3.1}$$

The backscattering cross section per unit volume η (m^2m^{-3}) can be found comparing two radar equations for distributed scatterers containing equivalent reflectivity and reflectivity respectively.

The radar equation for distributed scatterers can be written as

$$\overline{P}(r_0) = \frac{P_t g^2 g_s \eta c \tau \pi \theta_1^2 \lambda^2}{(4\pi)^3 r_0^2 l^2 l_r 16 \ln 2}, \tag{3.3.2}$$

where $P(r_0)$ is power at the output of the radar receiver from a scatterer (W), r_0 is the scatterer range (m), P_t is the transmitted power (W), g is the antenna gain, g_s is the net gain of the T/R (transmit/receive) switch, the synchronous detector, and the filter-amplifier (i.e., the entire receiver chain), c is the speed of light (~ 3 x 10^8 ms^{-1}), τ is the

pulse length (s), θ_l is the angular beam-width (radians), l is the total loss factor due to attenuation from hydrometeors and atmospheric gases, (close to 1), l_r is the bandwidth loss factor, a function of shape of the transmitted pulse and the receiver frequency response, which is also called the receiver loss. The radar equation for distributed scatterers can be also written using the equivalent reflectivity factor Z_e:

$$\overline{P}(r_0) = \frac{P_t g^2 g_s c\tau\pi^3\theta_1^2 |K|^2 Z_e}{2^{10}\lambda^2 r_0^2 l^2 l_r \ln 2}, \tag{3.3.3}$$

where $|K|^2$ is the magnitude squared of the parameter related to the complex index of refraction of water. Rearranging (3.3.2) for η gives

$$\eta = \frac{2^{10}\pi^3 r_0^2 l^2 l_r (\ln 2)\overline{P}}{P_t g^2 g_s c\tau\pi\theta_1^2\lambda^2} = \frac{2^{10} r_0^2 l^2 l_r (\ln 2)\overline{P}}{P_t g^2 g_s c\tau\theta_1^2}\frac{\pi^3}{\pi\lambda^2} = A\cdot\frac{\pi^2}{\lambda^2}, \tag{3.3.4}$$

where A is a value not affected by assumption on the nature of a scatterer.

Rearranging (3.3.3) for Z_e gives

$$Z_e = \frac{2^{10}\lambda^2 r_0^2 l^2 l_r (\ln 2)\overline{P}}{P_t g^2 g_s c\tau\pi^3\theta_1^2 |K|^2} = \frac{2^{10} r_0^2 l^2 l_r (\ln 2)\overline{P}}{P_t g^2 g_s c\tau\theta_1^2}\frac{\lambda^2}{\pi^3|K|^2} = A\cdot\frac{\lambda^2}{\pi^3|K|^2}. \tag{3.3.5}$$

Substituting A from (3.3.5) into (3.3.4) gives the reflectivity

$$\eta = \frac{Z_e\pi^3|K|^2}{\lambda^2}\cdot\frac{\pi^2}{\lambda^2} = \frac{Z_e\pi^5|K|^2}{\lambda^4}. \tag{3.3.6}$$

The radar equation for a point scatterer can be written as

$$\overline{P}(r_0) = \frac{P_t g^2\lambda^2\sigma_b f^4(\theta,\phi)}{(4\pi)^3 r^4 l^2}\frac{g_s}{l_r}, \tag{3.3.7}$$

where σ_b is the cross section (m^2), and $f^4(\theta,\phi)$ is the two-way antenna pattern function. The return power $P(r_0)$ is the value measured by radar receiver, no matter how it was backscattered. The equations (3.3.2) and (3.3.7) can be combined

$$\overline{P}(r_0) = \frac{P_t g^2 g_s \eta c \tau \pi \theta_1^2 \lambda^2}{(4\pi)^3 r_0^2 l^2 l_r 16 \ln 2} = \frac{P_t g^2 \lambda^2 \sigma_b f^4(\theta,\phi)}{(4\pi)^3 r^4 l^2} \frac{g_s}{l_r}. \quad (3.3.8a)$$

The similar parts can be canceled

$$\frac{P_t g^2 \lambda^2 g_s}{(4\pi)^3 r^2 l^2 l_r} \cdot \frac{\eta c \tau \pi \theta_1^2}{16 \ln 2} = \frac{P_t g^2 \lambda^2 g_s}{(4\pi)^3 r^2 l^2 l_r} \cdot \frac{\sigma_b f^4(\theta,\phi)}{r^2}, \quad (3.3.8b)$$

which simplifies to

$$\frac{\eta c \tau \pi \theta_1^2}{16 \ln 2} = \frac{\sigma_b f^4(\theta,\phi)}{r^2}. \quad (3.3.8c)$$

For a scatterer in the center of the beam $f^4(\theta,\phi) = 1$. Rearranging terms in equation (3.3.8c), the cross section can be found

$$\sigma_b = \frac{\eta c \tau \pi \theta_1^2 r^2}{16(\ln 2)}. \quad (3.3.9)$$

The cross section can also be found from equations (3.3.3) and (3.3.7), using similar cancellation and rearranging:

$$\sigma_b = \frac{Z_e |K|^2 c \tau \pi^6 \theta_1^2 r^2}{\lambda^4 16(\ln 2)}. \quad (3.3.10)$$

The cross-section values found using equations (3.3.9) and (3.3.10) are identical. Table 3.1 summarizes the calculated results for Airplane-1, and Table 3.2 shows results for Airplane-2. Note that Airplane-2 was not detectable before the 8th and during the 9th time cuts. The following values are used for the calculations: $\lambda = 0.1$, $|K|^2_{water} = 0.93$, $\tau = 1.57\times10^{-6}$, $\theta_l = 0.95°(\pi/180)$. The column "Cross section" of Table 3.1 shows the results for Airplane-1, and the same column of Table 3.2 gives the Airplane-2 cross-section values. The cross section for each airplane's detection is slightly different due to airplane orientation, the location of the airplane within the resolution volume,

and possible presence of other scatterers. The cross-section values are likely underestimated because the computations assume that an airplane is located in the center of the resolution volume.

The bending of the beam at ranges 5 to 15 km from the radar can be ignored. The geometry is approximated by a right triangle *XYZ*, shown in Figure 3.5. The hypotenuse $XZ = r$ is the range of the target located at point *Z*. The angle $\angle ZXY = \alpha$ is the elevation angle of the antenna. The leg $ZY = h$ is the height of the beam centerline above the antenna, as indicated in Figure 3.5. The height of the beam centerline above the ground can be calculated as a sum of the radar antenna height *H* and $h = r \sin\alpha$. The height of the antenna above the ground is a constant that can be accounted for at any time; therefore, it is ignored for now. The height *h* of the beam centerline above the antenna, calculated for Airplane-1 detections, is given in column 5 of Table 3.1, and the same of Airplane-2 is given in column 5 of Table 3.2.

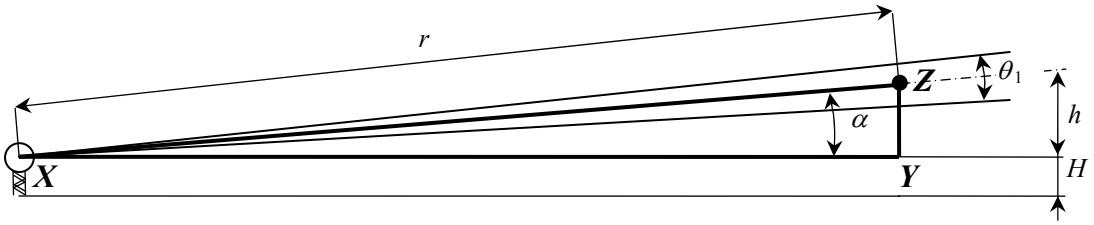

Figure 3.5: Beam geometry at close ranges. The target is shown as a black dot. The target range *r* is assumed to be between 5 and 15 km, so that the beam is not bending. α is the elevation angle, θ_1 is the beam-width, *h* is the height of the beam centerline, and *H* is the height of the antenna above the ground.

The position of the scatterer within the radar beam can be estimated if the cross-section of the target is assumed to be a constant. Then, from equation (3.3.8c) the values of the antenna pattern function $f^4(\theta,\phi)$ can be estimated. The unit value of the two-way antenna pattern function corresponds to scatterer located exactly on the

centerline of the beam in a given resolution volume. A smaller value of $f^4(\theta,\phi)$ corresponds to scatterer located farther away from the centerline of the beam. But the assumption that the cross section does not change is not valid for a turning or tilting airplane.

There is another way to estimate the position of the scatterer within the radar beam. Examining only even or only odd time cuts helps to avoid jumps caused by the lag in antenna positioning system, thus smoothing the path. Figures 3.6a and 3.6b show two views of the Airplane-1 echoes. Only odd time cuts are shown. Each disk shaped area represents a resolution volume with the registered echo. Airplane-1 echoes from the 1st and the 3rd time cuts are registered within the same beam, or radial, as shown in Figure 3.6b. All other echoes are located in the different beams. The radar sends beams of 1°-width with a step of about 0.4°. Overlapping of the beams causes detection of a scatterer by neighboring beams. The stronger return is detected in the beam where the scatterer is closest to its centerline. Geometrically the conical surface of one beam can be cut by two vertical planes parallel to the beam centerline and intersecting the beam at the lines where the neighboring overlapping beams cross each other. Only the part of the beam limited by the vertical planes contains the target. Then, the vertical cut of the beam perpendicular to the beam centerline has an area of the cropped disk as shown in Figure 3.7. Knowing that (1) the height of the beam centerline at the Airplane-1 ranges varies from 250 meters to 350 meters, as will be shown in Figure3.8, (2) the altitude of the airplane was about 350 - 400 meters, and (3) the largest estimated Airplane-1 cross section was during time cut 2 (Column Cross Section, Table 3.1), I assume that during time cut 2 Airplane-1 was located on the beam centerline in the

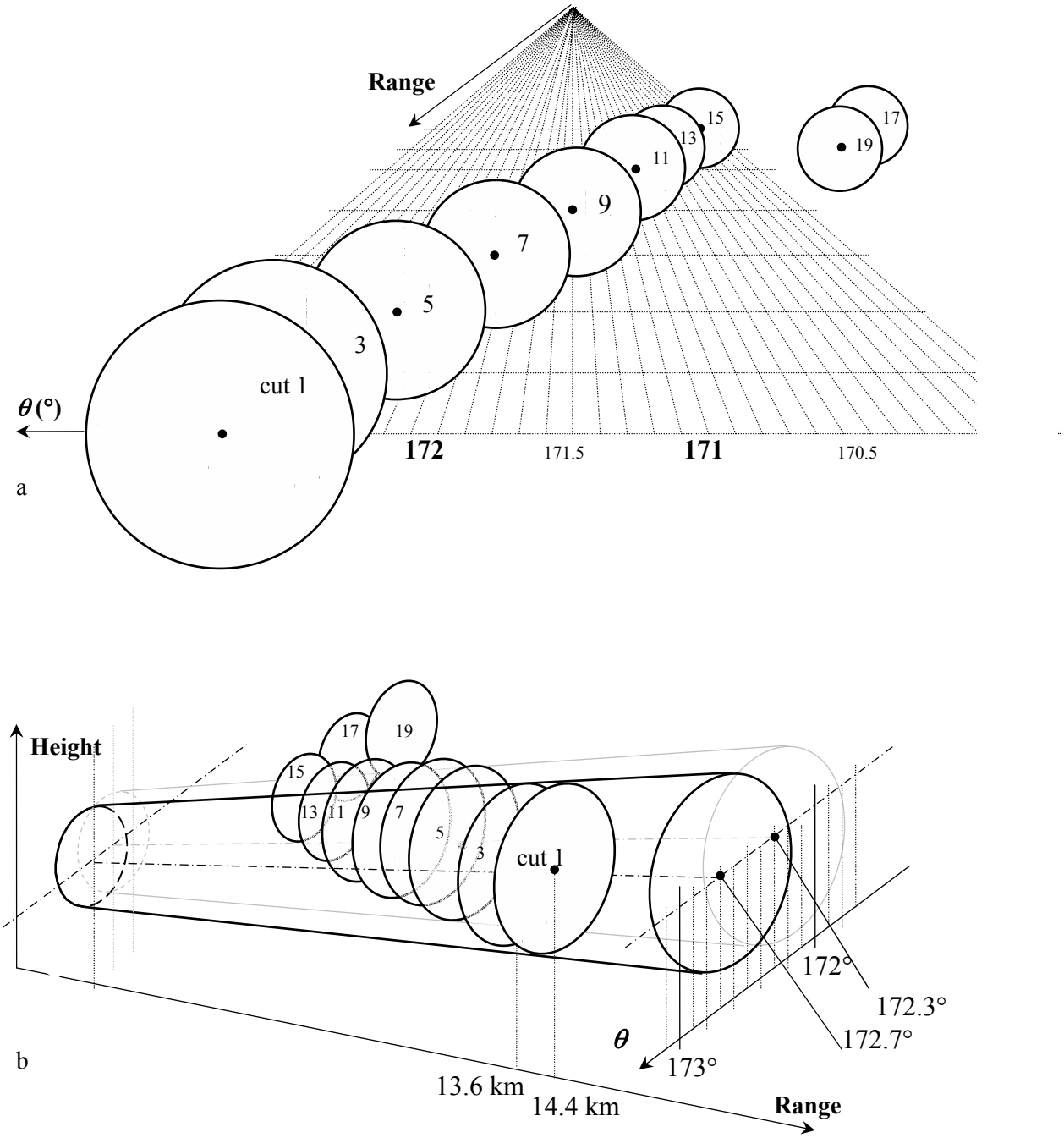

Figure 3.6: Areas of 1°-beams at ranges and radials registered Airplane-1 echo.
(a) View from south looking toward the radar. Circles show one degree border of the beam.
(b) View from west-southwest. Cuts 1 and 3 are in the same radial 172.7°, as indicated. Cut 15 is the closest to the radar. Only 2 beams are shown for simplicity.
Note that a circle represents a center slice of the resolution volume 250 m wide.

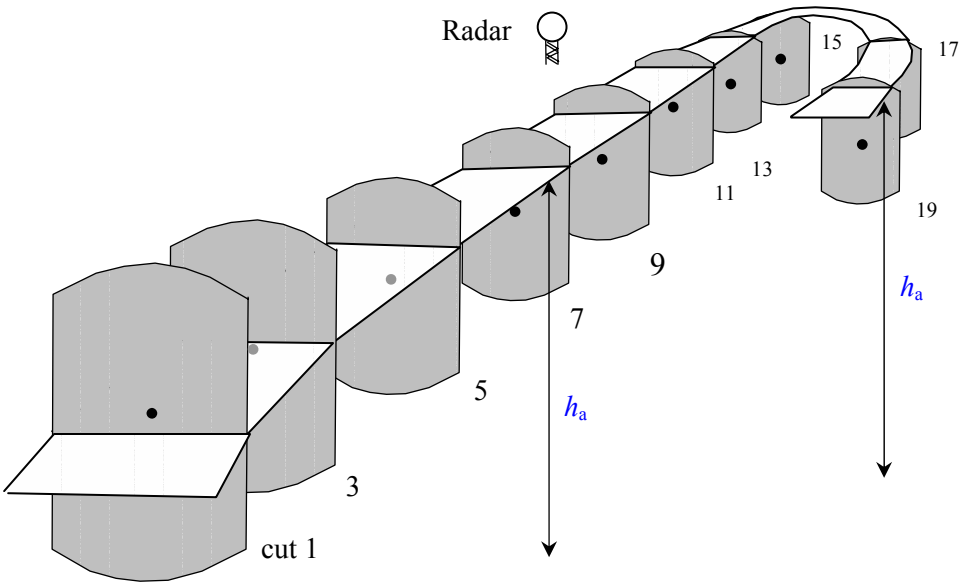

Figure 3.7: Airplane path estimated in 3 dimensions.
Every shaded area is a cropped circle, representing a vertical cut of the 1° beam propagating from the radar out of the page, with elevation angle 1.5°. Beams are sent with a step of about 0.4°. Overlapping of the beams allows cropping of an area of a circle to the indicated shape. The dot in the center of each shaded area represents the centerline of the beam. A horizontal plane intersects every cut at the altitude h_a = 363 m above the radar antenna.

middle of the resolution volume, and therefore, it was navigating at the altitude h_a = 363 m above the antenna. The maximum power of the radar beam is concentrated along its centerline. Then, the 3-dimensional trajectory reveals that Airplane-1 is located above the beam at the 15th time cut, or above the half-power surface, explaining the small cross section value during cut 15 (Column Cross Section, Table 3.1).

3.4 Fitting cross section to Gaussian

The radar beam pattern is represented by a Gaussian function $A \exp(-x^2/2\sigma_b^2)$, where A is the amplitude, and $\sigma_b = \theta_1/16\ln 2$. The echoes of Airplane-1 at time cut 15 are smaller then the echoes at other time cuts because the airplane was located farther away from the center of radar beam. The maximum value of σ_b for Airplane-1 at the 2nd time most likely corresponds to its location in the centerline of the resolution

volume, or on the very top of the Gaussian curve, approximating the radar beam shape. It is hard to fit cross-section values to one Gaussian curve because the target was detected in different 1°-beams (Figure 3.6) due to the spread of the weighting function. The altitude and range of the Airplane-1 are shown in Figure 3.8. The dashed line shows the beam centerline with marked ranges of the Airplane-1 echoes. Dotted lines above and below the beam centerline show the half-power border of the beam. The airplane altitude is denoted by a solid line, while its range for every time cut is indicated by circles. As indicated by numbers corresponding to the time cuts, the airplane moves from right to left (time cuts 0 through 15), and from left to right (time cuts 16 to 19). Ascending angle γ_i is defined as the elevation angle of a target at T_i. The distance between two consecutive positions of Airplane-1 can be found in terms of degrees of ascent $\Delta\gamma_i$ of the ascending angle γ_i, as shown in Figure 3.9. The ascent $\Delta\gamma_i$ can be found by subtracting the ascending angle γ_i created by a target at T_i from the ascending angle γ_{i+1} created by a target at T_{i+1}

$$\Delta\gamma_i = [\sin^{-1}(h_a / r_i) - \sin^{-1}(h_a / r_{i+1})]180/\pi. \quad (3.3.12)$$

The calculated ascending reading angles are given in Table 3.4. Negative values mean that target Airplane-1 has turned and the angle descends.

Table 3.4: Ascending angles of Airplane-1

Between Time cuts	**Angle, degrees**	**Between time cuts**	**Angle, degrees**	**Between time cuts**	**Angle, degrees**
0-1	0.0267	7-8	0.0333	14-15	0.1173
1-2	0.0512	8-9	0.0362	15-16	-0.0024
2-3	0.0298	9-10	0.0804	16-17	-0.0556
3-4	0.0560	10-11	0.0377	17-18	-0.0593
4-5	0.0321	11-12	0.0955	18-19	-0.0978
5-6	0.0347	12-13	0.0514		
6-7	0.0669	13-14	0.0541		

The cross-section values spaced with the appropriate angular distances are shown in Figure 3.10a as numbered dots. Solid lines show three Gaussian curves with amplitudes 8, 2, and 1. The Gaussian curve corresponding to the cross-section two square meters fits data points the best. The actual cross-section of a small craft as seen by the radar is in the range 2 to 4 square meters [19]. The value 8 square meters is an outlier probably caused by presence of additional scatterers in the resolution volume (e.g. birds, other airplane), or favorable position of the aircraft.

A 5-point average of the cross-section data with dropped outlier (cut 2) is shown in Figure 3.10b in solid line. The dashed line is used to show the fitted Gaussian curve. The dotted line is used to show the same Gaussian curve, shifted to fit the values corresponding to the negative ascending angles, or to the time when the airplane turned around and started moving away from the radar. I observed several clusters of data in Figure 3.10b, e.g. {7, 9, 11, 13}, or {8, 10, 12}. Note, that a cluster contains the data points from either odd or even time cuts. Therefore, a possible good outcome caused by the backlash of the antenna is ignored, e.g. {0, 3, 5, 8} make a distinct curve, but it is ignored.

To understand the nature of these clusters, I imagined the Gaussian 2-dimension "hat", because the actual 3-dimension Gaussian is too hard to visualize. Any vertical cut of the "hat", shown in Figure 3.11, is a 1-dimension Gaussian curve. The target is moving on through the "hat" from one curve to another, drawing spatially farther, or closer to the top of the "hat".

At the 13^{th} time cut, a time when airplanes were at the same range, the cross-section of Airplane-2 is larger than that of Airplane-1. By analyzing the flight of the

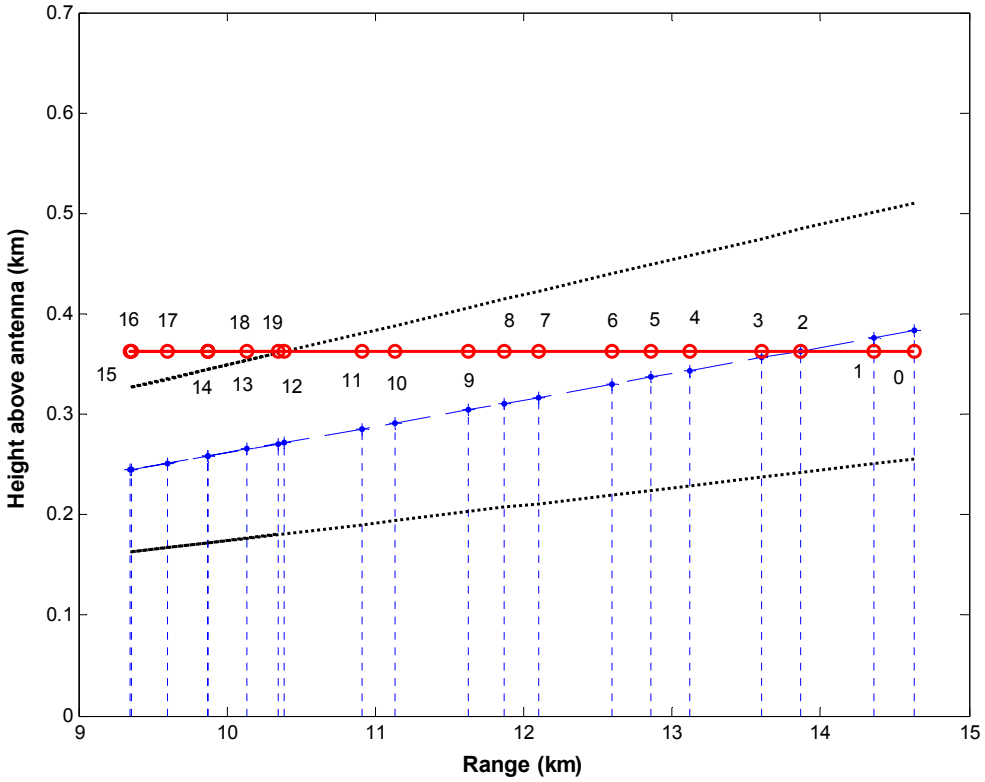

Figure 3.8: Side view of the Airplane-1 trajectory.
Beam centerline is shown with a dashed line. Dotted lines above and under beam centerline indicate the half-power border of the beam. Crosses on the beam centerline show the ranges of the echoes from Airplane-1. Altitude of the airplane is shown with a solid line. The numbered circles indicate estimated position of the Airplane-1. Numbers stand for the time cuts of the readings.

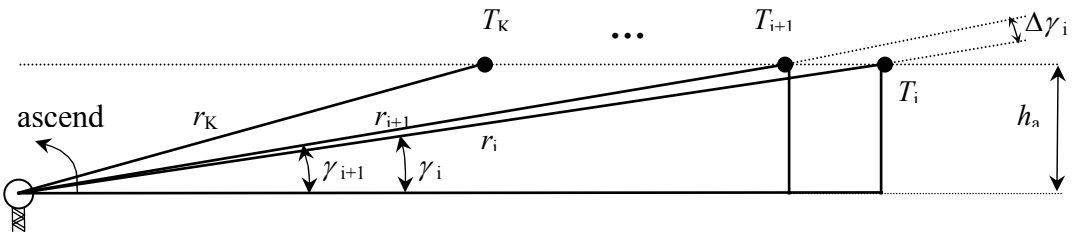

Figure 3.9: Ascending angle.
The top dotted line shows a constant height above the antenna. Ascending angle γ_i is defined as the elevation angle of a target at T_i. Ascending angle γ_{i+1} is the elevation angle of a target T_{i+1}. The values of i vary from 1 to K depending on the time cut. Ascent $\Delta\gamma_i$ is the difference angle of elevation between target at T_i and T_{i+1}.

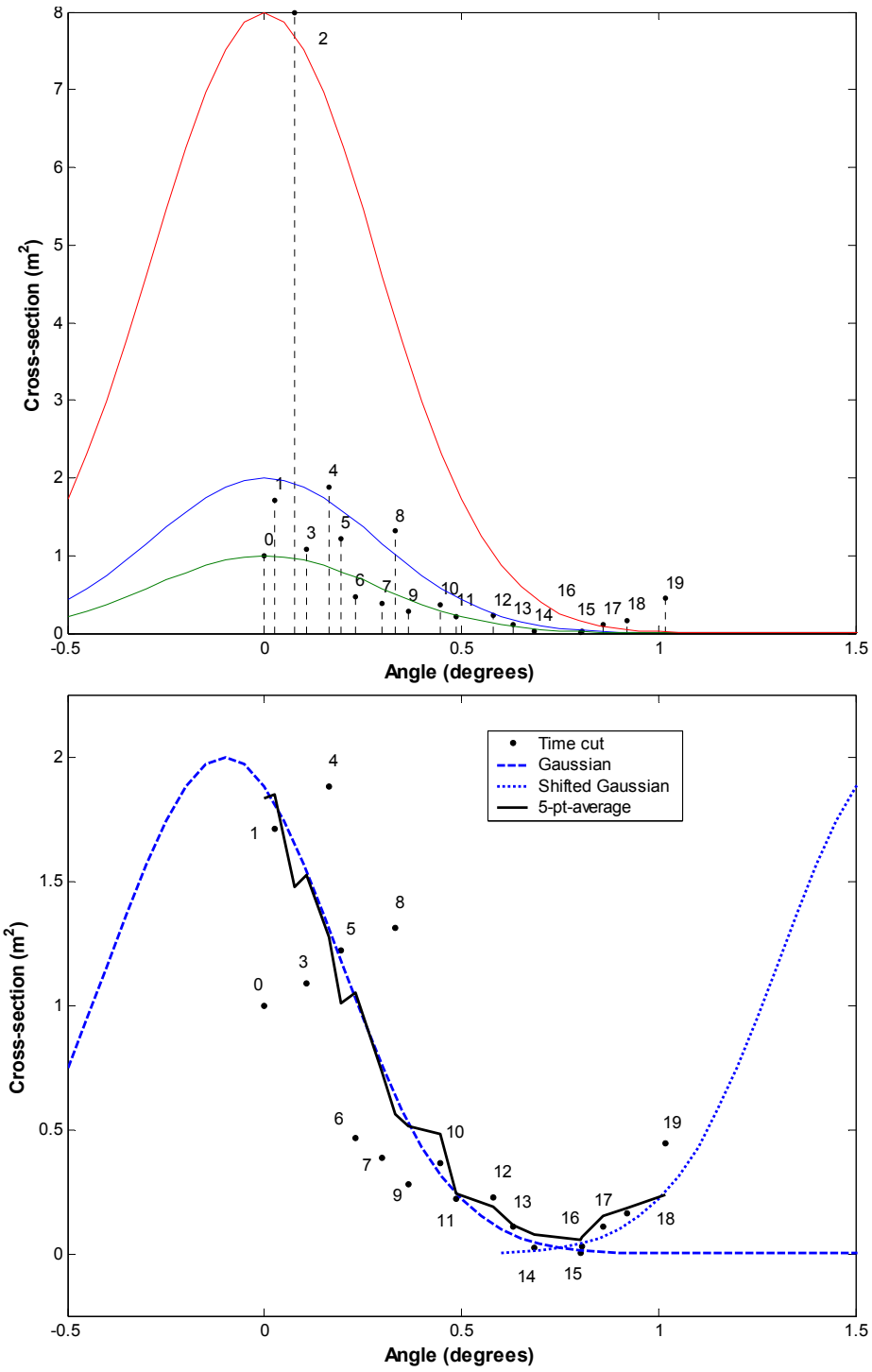

Figure 3.10: Fitting Cross-section to Gaussian curve.
(a) Viewing 3 curves: top curve is 8 $\exp(-x^2/2\sigma_b^2)$, middle curve is 2 $\exp(-x^2/2\sigma_b^2)$, and bottom curve is $\exp(-x^2/2\sigma_b^2)$. The outlier might occur because of the presence of other scatterers in the resolution volume (e.g. other scatterers).
(b) 5-point average with dropped maximum value fits very well the Gaussian curve with amplitude 2. Note that Time cut 15 is the turning point.

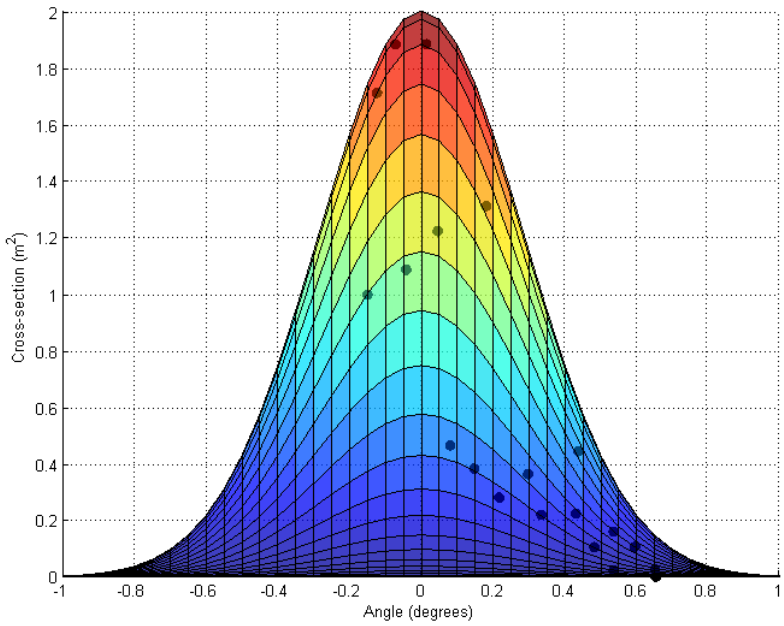

Figure 3.11: Gaussian "hat" with fitted cross-section values.
The cross-section data points are shown as black dots. Each cut of the "hat" is a 2-dimensional Gaussian.

Airplane-2, I noticed a change of its cross-section depending on the position of the airplane. For example, the cross-section of Airplane-2 is the greatest at cuts 12, 13, and 14. During these time cuts Airplane-2 is turned sideways to the radar. As expected and in agreement with optical cross section the EM cross section of an aircraft side is larger then its front or back looking cross section.

3.5 Spectra

A spectrum $X(e^{j\omega})$ of a discrete signal $x[n]$ provides the information about the composition of the signal from complex exponentials, and can be represented by a linear combination of sinusoids at different frequencies

$$X(e^{j\omega}) = \sum_{n=-\infty}^{+\infty} x(n)e^{-j\omega n} . \qquad (3.5.1)$$

The deterministic autocorrelation r_{xx} of a discrete signal $x(n)$ is defined as

$$r_{xx}(l) = \sum_{n=-\infty}^{+\infty} x^*(n)\, x(n+l),\ \ l = 0, \pm 1, \pm 2, \ldots, \tag{3.5.2}$$

where the parameter l (lag) is the time-shift. A power spectrum or spectral density of a signal is obtained by the Fourier transform of an autocorrelation function. It is a non-negative real-valued function of frequency. The power spectrum of the radar echo energy is a one-sided DFT (Discrete Fourier Transform) and it is called the Doppler spectrum. The finite sequence is weighted by a non-rectangular window function to reduce coupling of strong spectral components into adjacent weaker ones. A raised cosine, or Von Hann window is used in this thesis and it is given by the formula

$$W(l) = 0.5 + 0.5\cos\left[\left(l - \frac{M-1}{2}\right)\frac{2\pi}{M}\right], \tag{3.5.3}$$

where M is the size of the window.

The spectra of Airplane-1 obtained using uniform window function and the Von Hann window are shown in Figure 3.11a and 3.11b, respectively. The radial for analyses at each time cut is chosen in agreement with the value of the azimuth angle in Table 3.1. A gate at the range indicated in Table 3.1 is considered to be the gate with the airplane. Two gates neighboring in range with the airplane gate are called *in front of*, and *behind* the airplane regardless of the flight direction. The gate *in front of* the airplane is defined as the gate closer to the radar, and the gate *behind* the airplane is the gate farther from the radar. A *clear-air* is defined as the gate with (1) the return power lower then its surroundings, and (2) the range location somewhat closer to the radar then Airplane-1 range. Airplane-1 spectra are shown with solid lines. The *clear-air* spectra are shown with dashed lines. The dotted lines show spectra at the gate *in front*, and *behind* Airplane-1.

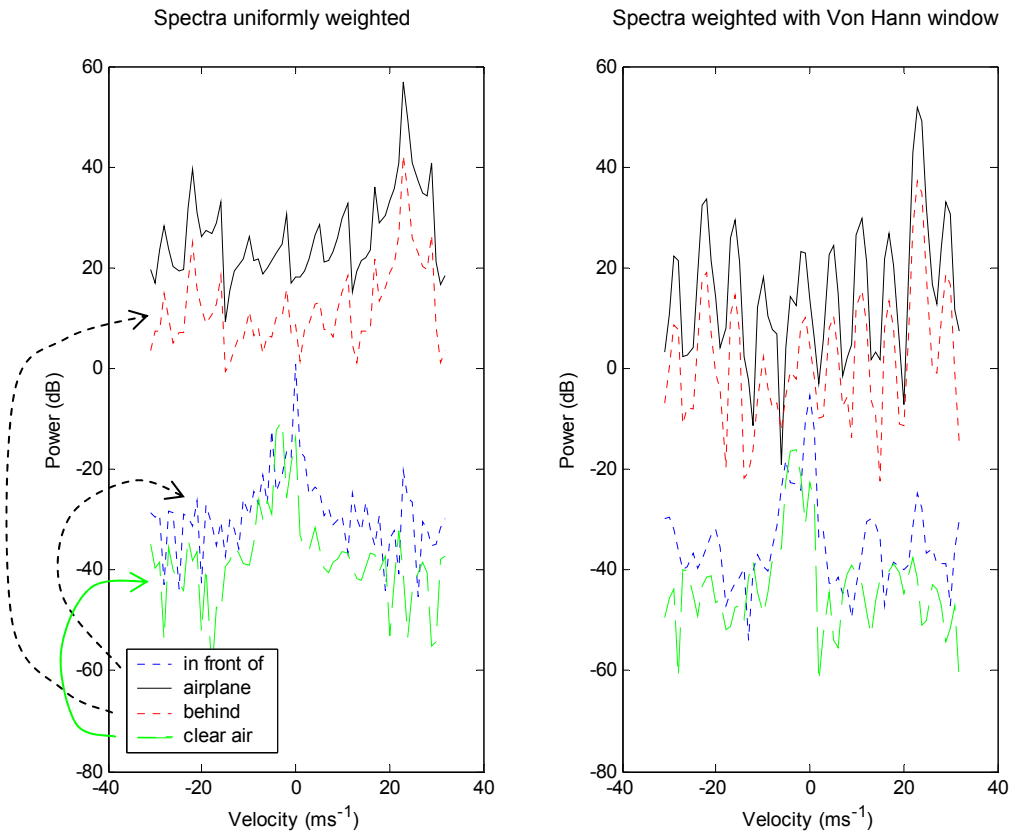

Figure 3.11: Spectra from the Airplane-1-gate at Cut 2 (Table 3.1), the gates *in front of* and *behind* the Airplane-1-gate and spectrum of *clear-air*: (a) uniformly weighted spectra, (b) weighted by the Vonn Hann window. Solid line indicates spectra of the gate with Airplane-1. Dotted lines show spectra at the gates *in front of* and *behind* the Airplane-1 gate. Dashed line is for *clear-air*. *In front of* the gate spectrum shows *clear-air*. *Behind* the gate spectrum repeats the airplane spectrum with smaller amplitude, due to the spread of the range dependant weighting function. Spectra shows 10 well pronounced peaks due to modulation caused by propeller rotation.

For each time cut figures similar to Figures 3.11a and 3.11b were generated and analyzed. For some cuts the spectrum at the gates *in front* of and *behind* the airplane gate shows similar shape to the airplane gate but with smaller amplitude. This is due to the spread of the skirt of the range-dependent part of the composite weighting function. The *clear-air* spectra in all 20 cuts show similar Gaussian-shape curve centered between –3 and –5 ms^{-1}. As noted in Section 2.5.2, the wind was blowing from south –

south-east at about 5 ms^{-1}. The peak corresponding to velocity 24 ms^{-1} indicates that Airplane-1 is moving at either 24 ms^{-1} away from the radar or 40 ms^{-1} toward radar, as described in Section 3.2.2. The *clear-air* spectrum is 40dB below the airplane spectrum. Another interesting common feature in the Airplane-1 spectrum is 10 well pronounced peaks, with one maximum. All 20 spectra have similar signature with a slight variation of amplitudes and fluctuations of the location of maxima. The peaks are spaced by 6 to 7 ms^{-1} interval. The 10 peaks could help to distinguish these spectra from other types of scatterers.

For comparison, similar analyses are done for Airplane-2. All eleven spectra of Airplane-2 echoes are similar to the one shown in Figures 3.12a. The solid line indicates the spectrum from the airplane gate. The dotted lines indicate spectrum from the gates *in front* of and *behind* Airplane-2. The dashed line is the spectrum of the *clear-air*. There are several similarities in the Airplane-1 and the Airplane-2 spectra. A range dependant repetition of the spectrum is observed in both cases. The radial component of the wind speed is the same for both cases. The maximum in the airplane spectra corresponds to the radial velocity of Airplane-2, similar to what was observed in Airplane-1 case. Unlike Airplane-1, the spectra of Airplane-2 do not exhibit modulations. It could be that Airplane-2 propellers are small compared to the dimensions of the airplane, or it is a jet airplane. The spectra from neighboring gates repeat the airplane spectrum with smaller amplitude, due to the spread of the range dependant weighting function. The peak at zero velocity in the *clear-air* spectra is due to the ground clutter. Animating spectra time allows observing fluctuations and distinguishing between little changes in the airplane spectra from the unique features

that are approximately constant. The extracted features would define the airplane signature. Thus, the types of airplanes may be distinguished by their spectra, if they indeed have the unique signatures.

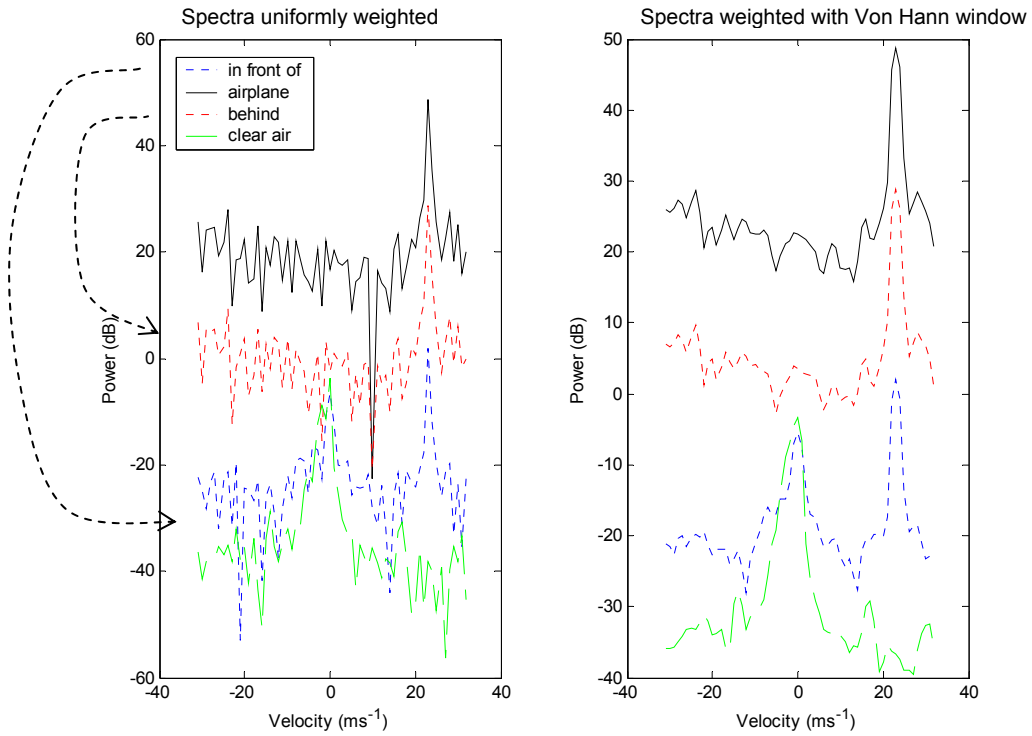

a b

Figure 3.12: Spectra from the Airplane-2-gate at Cut 10 (Table 3.2), the gates *in front of* and *behind* the Airplane-1-gate and spectrum of *clear-air*: (a) uniformly weighted spectra, (b) weighted by the Vonn Hann window. Solid line indicates spectra of the gate with Airplane-2. Dotted line shows spectra at the gates *in front* and *behind* the Airplane-1 gate. Dashed line is for *Clear-air*. The spectra from neighboring gates repeat the airplane spectrum with smaller amplitude, due to the spread of the range dependant weighting function

3.6 Modulations

In Section 3.4 modulation is apparent in spectra of Airplane-1. It is hypothesized that these modulations are likely caused by propeller rotation. In each spectrum there are 10 almost equally spaced maxima. The spacing between two consecutive peaks is approximately between 6 and 7 ms^{-1}.

In the Homeland Security Experiment document CR1 Test Plan of 19 Mar 2003, it is stated that the aircraft used in the experiment is a Cessna 188 AgWagon, shown in Figure 3.13. Such airplanes have 235 to 300 horsepower and 2-bladed propellers. In this section simulations are used to demonstrate that similar modulation can be produced. Airplane-2 is an unknown aircraft, and the discussion on it is closed due to uncertainty of all the discoveries and inability to prove or contradict the results.

Figure 3.13: Cessna 188 Ag Wagon. The propeller has 2 blades.

If a propeller is spinning at 2400 rpm or 40 revolutions per second, then any blade of the propeller passes a specific point in the arc 40 times every second. It would take 0.025 seconds for a blade to make one revolution. The signal from a flying airplane with a propeller is affected by many factors: (1) the speed of flight and the position of the airplane in the volume of scan, (2) the propeller rotation speed, (3) the weather factors affecting flight (shaking due to winds, shear), and (4) moving of the airplane parts, as ailerons (movable outside edges of the wing, that turn the plane), flaps (part of the wing that can move down to act as brakes), and elevator (tail part of the plane that moves to make the plane pitch up or down). In this work, only a simple model is used, shown in Figure 3.14. In other words, the weather and the moving parts except the propeller could be neglected.

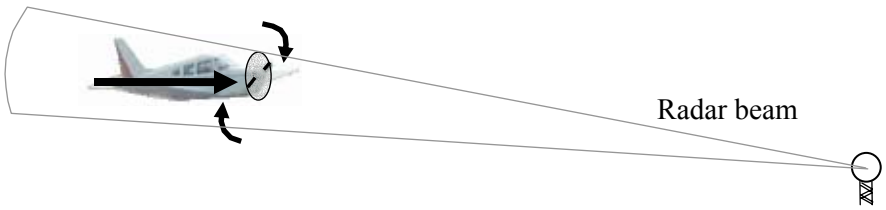

Figure 3.14: Simple model for detection of a signal modulated by a 2-bladed propeller. Radar beam radiates toward the airplane (bold velocity vector) moving forward, and the rotating propeller (black curved arrows).

A received signal $y(k)$ produced by an airplane with a constant speed, and a rotating propeller can be written in the form

$$y(k) = A\exp(jk\omega_d) + B\exp(jk(\omega_d - \omega_1)) + B\exp(jk(\omega_d + \omega_1)), \qquad (3.7.1)$$

where A is amplitude caused by the airplane's main body, B is amplitude of a signal reflected from the propeller, ω_d is the Doppler shift due to the airplane movement, ω_1 is the shift caused by propeller blade (moving toward or away from the radar, curved arrows in Figure 3.14). The propeller causes reflections which in turn create modulations if the airplane is not flying along beam axis. Even if the plane is aligned on the average with the beam axis, instantaneous deviations due to pitch and yaw will be present. The Doppler shift from the propeller depends on the location of dominant scatterers. If the scatterers are equally strong along the propeller then the shift will have a distribution between 0 (corresponding to propeller center) and the maximum value at the end of propeller blade. The simplified model herein assumes dominant scatterers are confined at some distance from the center hence the modulation can be represented with a single sinusoid $\omega_1 = C\sin(\alpha t)\big|_{t=kT}$, with an amplitude C, and $\alpha = 2\pi(rpm/60 \times blades)$, where *rpm* is the propeller speed in revolutions per minute, *blades* is the number of the blades on the propeller, and sampling rate $T = 7.8\times10^{-4}$. White noise is added to the signal. The modeled signal is sampled at the radar PRF, and the DFT of

the result is taken. Spectral signatures are investigated using several propeller speeds from 1000 up to 5000 rpm, different airplane speeds from 40 to 55 ms^{-1}, and different amplitude values *A*, *B*, *C*. It was found that observed spectra can be reproduced in simulation when a speed of 41 ms^{-1}, a 2-bladed propeller rotating at 2400 rpm were used. The resulting signal and its spectrum are shown in Figures 3.14a and 3.15 respectively.

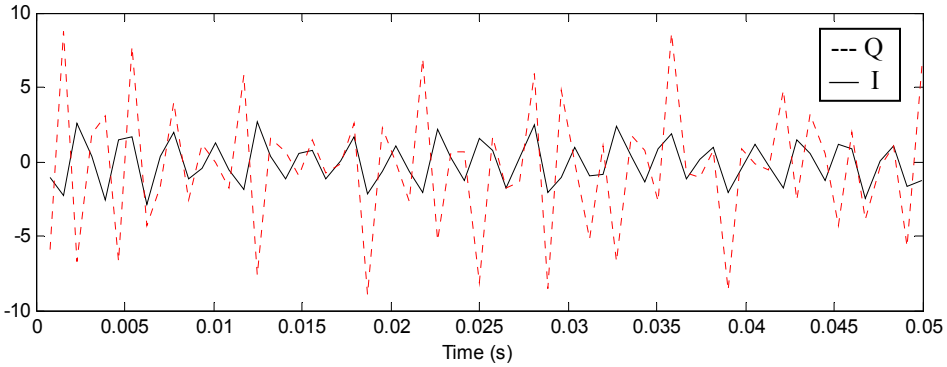

a

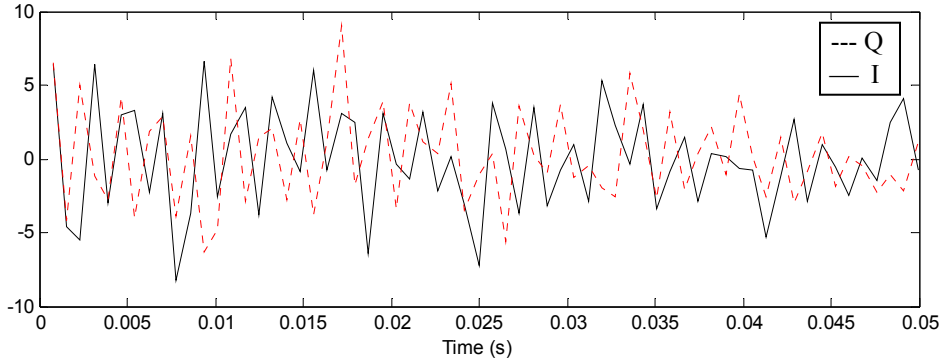

b

Figure 3.14: I-Q samples of (a) the actual signal from airplane registered during 5th time cut in the 54th range location of radial 171.9°, (b) simulated signal, obtained from the sampling at radar PRF of a continuous signal, modeled by a craft moving at 41m/s with a 2-bladed propeller rotating at 2400 rpm. The amplitudes of the simulated airplane body and propeller returns are 2 and 0.5 respectively (A=2, B=.5, C=248).

Simulation result has demonstrated that an airplane echo contains the signature of propeller rotation. A more complicated model of an airplane would include (1) a

function of the airplane cross-section change due to tilt and turn, and (2) a function of airplane speed variation.

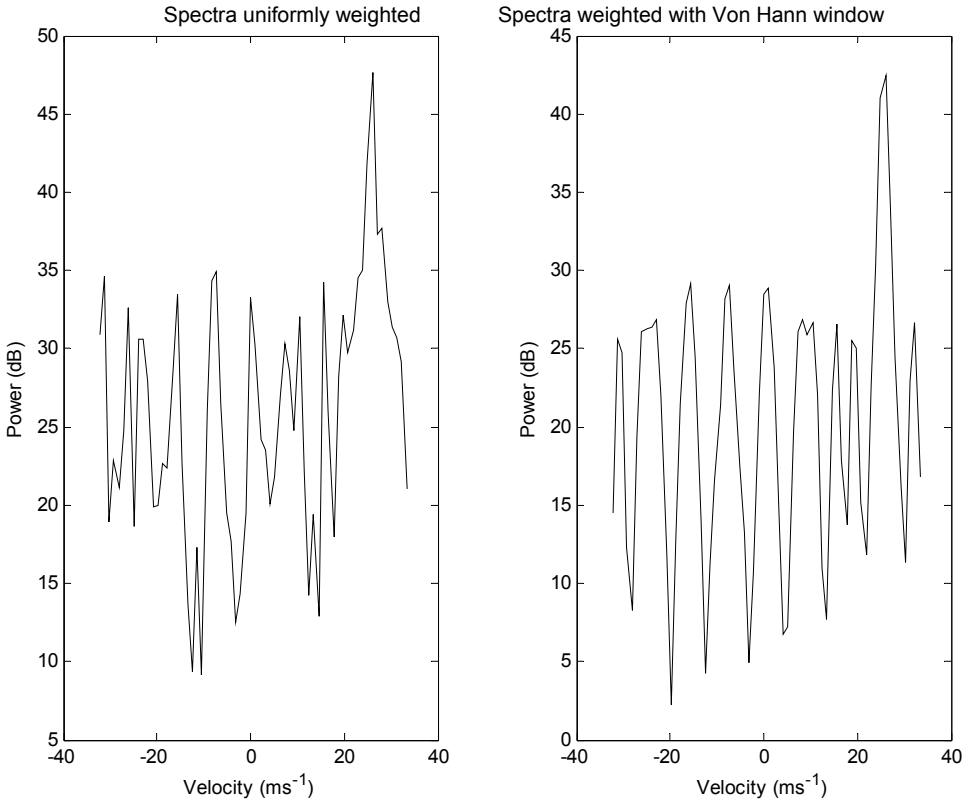

a b

Figure 3.15: Spectra of the simulated signal from a craft moving at 41ms^{-1} with a 2-bladed propeller rotating at 2400rpm: (a) uniformly weighted; (b) weighted by the Von Hann window.

3.7 Conclusion

An airplane has features in its spectra corresponding to the physical specifications of the craft. Airplanes could be distinguished by their spectra. The simple model of the airplane replicated spectral characteristics of Cessna 188 Ag Wagon.

4. Birds

The goal of this section is to investigate spectra of birds. These bird spectrum signatures could be used in distinguishing these echoes for filtering the weather signals, or obtaining information for ornithological studies.

4.1 Single Birds from data set 3/26

The same data as used in Chapter 3 include bird echoes. The velocity and reflectivity PPIs shown in Figures 3.2a and 3.2b contain a number of specks with nonzero velocities (not related to the wind speed) corresponding to small reflectivity values. These specks might be birds. An example of the returned power along the 178.6° radial is shown in Figure 4.1a for all 468 range locations and in Figure 4.1b for only 85 range locations to magnify features.

The pointers in Figure 4.1b indicate ground clutter and birds. It is not possible to distinguish the nature of the return looking at the returned power peaks. The decision on the nature of the scatterers can be made either by (1) spectral analysis/velocity estimation or by (2) visual analysis of the real part of voltage. The evidence of ground clutter in Doppler spectra is a peak at zero velocity. The evidence of ground clutter in the time domain is a slowly varying, almost DC signal. The *I* components of the received *I*-*Q* samples (Figure 4.2), corresponding to some of the peaks in Figure 4.1b, demonstrate significant visual differences that may be used to classify observed peaks on ground clutter returns and returns from birds. Figure 4.2a shows sinusoid signals that are most likely returned from birds. Figures 4.2b and 4.2c demonstrate ground clutter signals and contaminated signal from both birds and ground clutter, respectively. There are 3 strong presumable bird returns in the observed radial presented in Figure

4.1b: (1) an echo from range 6.2 km (gate 28), (2) an echo from 7.6 km (gate 34), and (3) an echo from 11.5 km (gate 49). I assume these returns are birds, though they might be the sidelobe returns from vehicles on the ground. The spectra of these gates weighted with the Von Hann window are displayed in Figure 4.3.

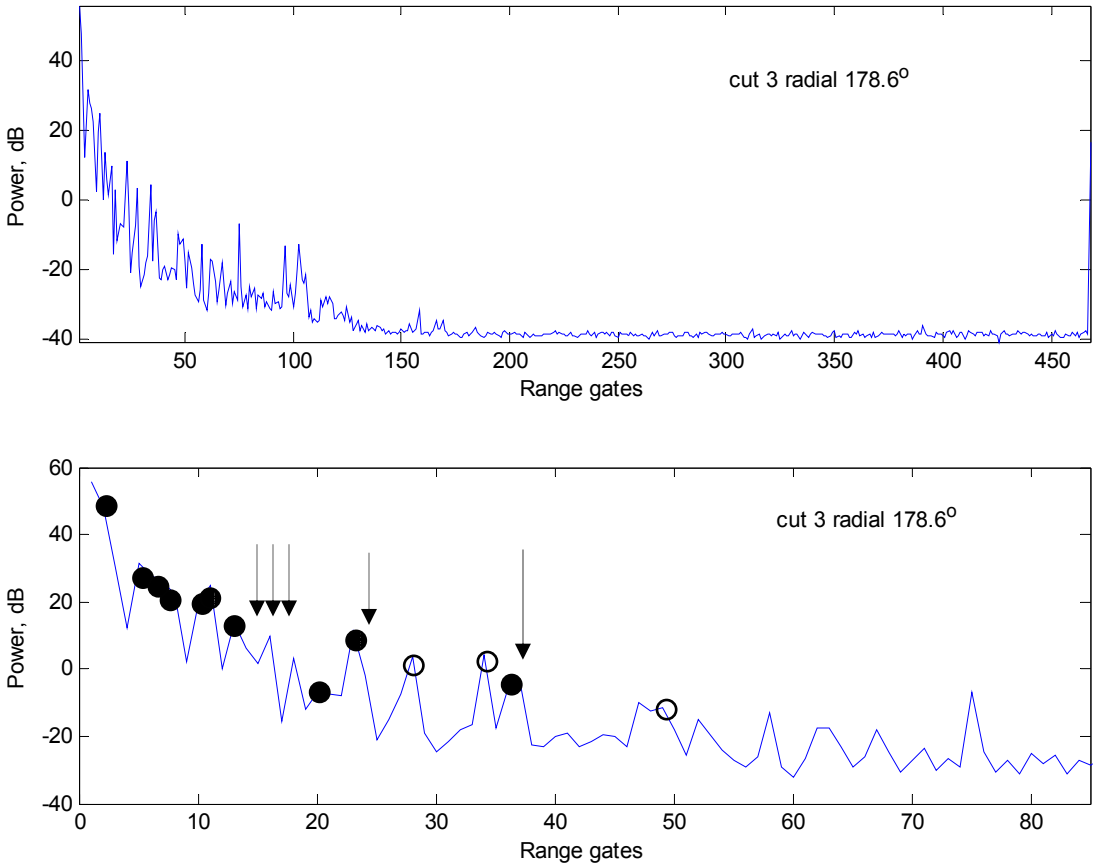

Figure 4.1: The return power of the radial 178.6° at time cut 3.
Top: All 468 range locations.
Bottom: 85 range locations. Only close ranges considered. The ground clutter returns are indicated by solid circles. The bird(s) returns are indicated by clear circles. The bird contaminated by ground clutter returns are indicated by arrows.

Evaluating spectra and voltages, I have chosen a bird that is closest to the radar and called it Bird-1. To investigate the behavior of the signal depending on the direction of the bird's flight, I have chosen another bird from a different radial and

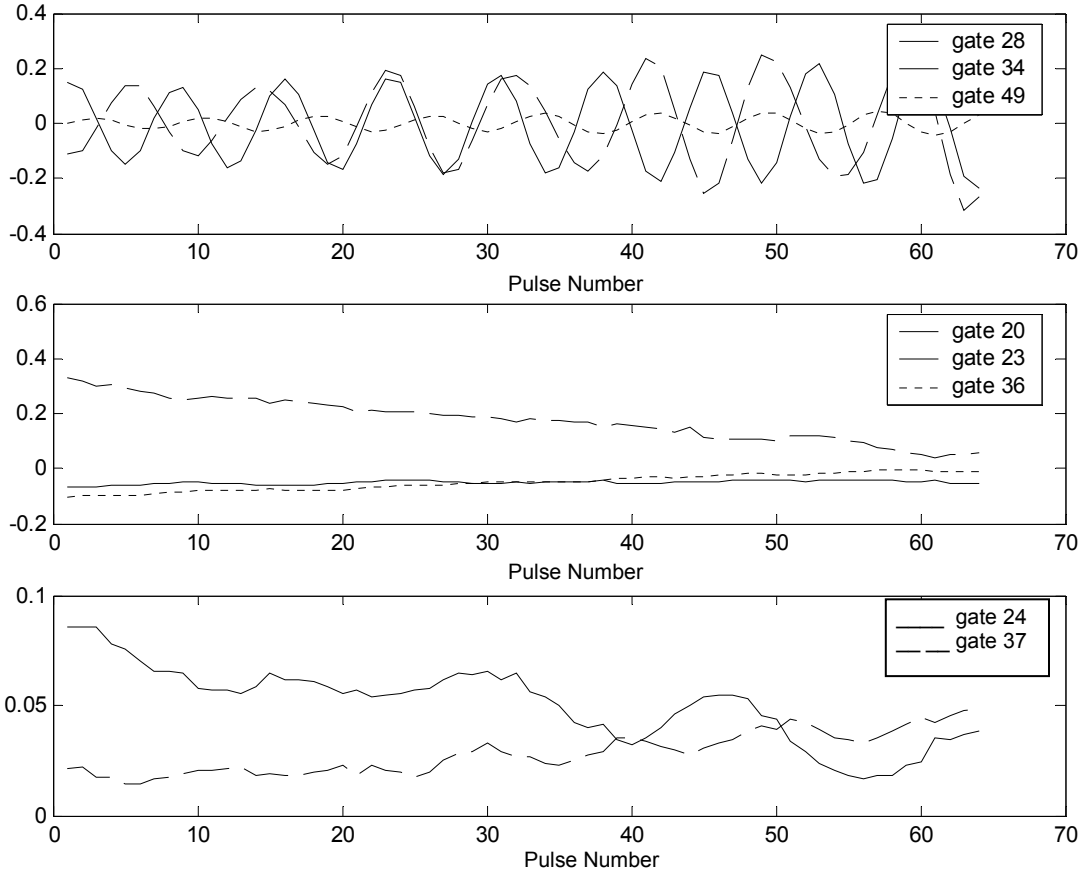

Figure 4.2: The real part of return voltage of the radial at 178.6° from: (top) birds, (middle) ground clutter; (bottom) bird contaminated by the ground clutter.

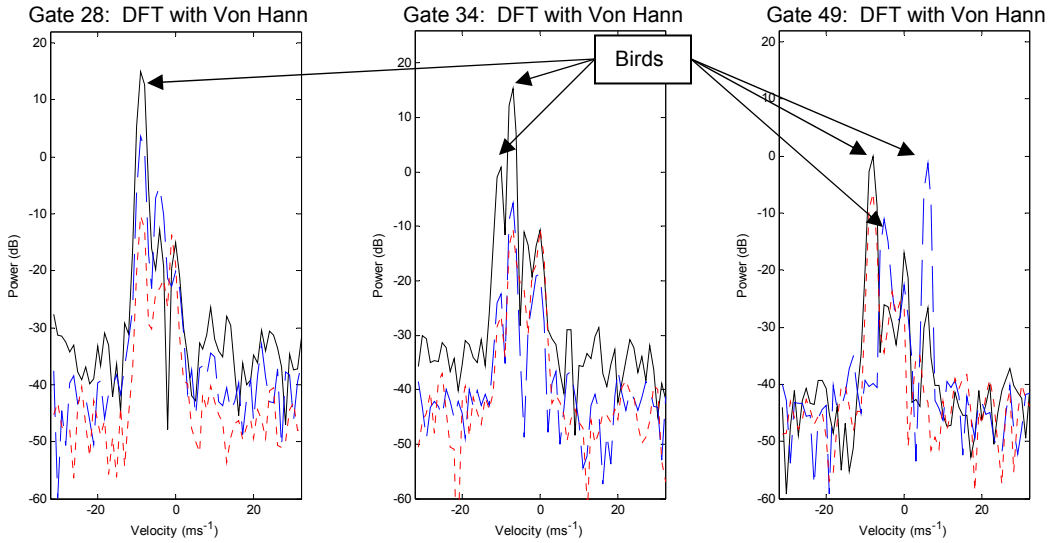

Figure 4.3: Spectra of birds in radial 178.6° at time cut 3.
All shown spectra are weighted with the Von Hann window. The solid line indicates the spectrum at the gate with the bird. The dotted and dashed lines show the spectra in front of, and behind the gate with the bird respectively.

called it Bird-2. Bird-2 was moving in the direction somewhat opposite to that of Bird-1. Bird-2 was flying against the radial velocity component of the wind, while Bird-1 was flying with the radial velocity components of the wind.

4.1.1 Tracking

Tracking of birds was similar to airplane tracking described in Section 3.1 because at close ranges (5 to 8 km) the reflectivity of bird echoes is relatively strong (about 15 dBZ) and easily seen on the reflectivity display of RRAT. The trajectories of Bird-1 and Bird-2 are shown in Figure 4.4. The Bird-1 track is almost straight, but the Bird-2 trajectory is complex. During the 7^{th} time cut Bird-2 is being carried by the wind. The reflectivity, azimuth and range values of Bird-1 and Bird-2 are given in Table 4.1 and Table 4.2 respectively. The spectra of Bird-1 and Bird-2 for several time cuts are shown in Figures 4.5 and 4.6 respectively. It is interesting to note that all 20 (one for each cut) Bird-1 spectra look very similar, each having a single prominent maximum. However Bird-2 spectra vary. Bird-2 is flying straight only during time cuts 0 through 6. During the time of the 7th through 19th time cuts, the spectra of Bird-2 changes could be due to diving, circling, and accelerating of the bird, and contamination by other birds, as described in Section 4.2. The overall speeds of flight estimated from bird trajectories are 10.3 ms^{-1} for Bird-1 and 6.9 ms^{-1} for Bird-2, a little bit larger than the radial velocities estimated from spectra 9 ms^{-1} for Bird-1 and 6 ms^{-1} for Bird-2. As expected, the bird flying against the radial velocity of the wind goes slower.

4.1.2 Cross section

The cross sections of the birds were calculated according to equation (3.3.9). The cross section values of Bird-1 are about 1000 times smaller than those of the airplanes,

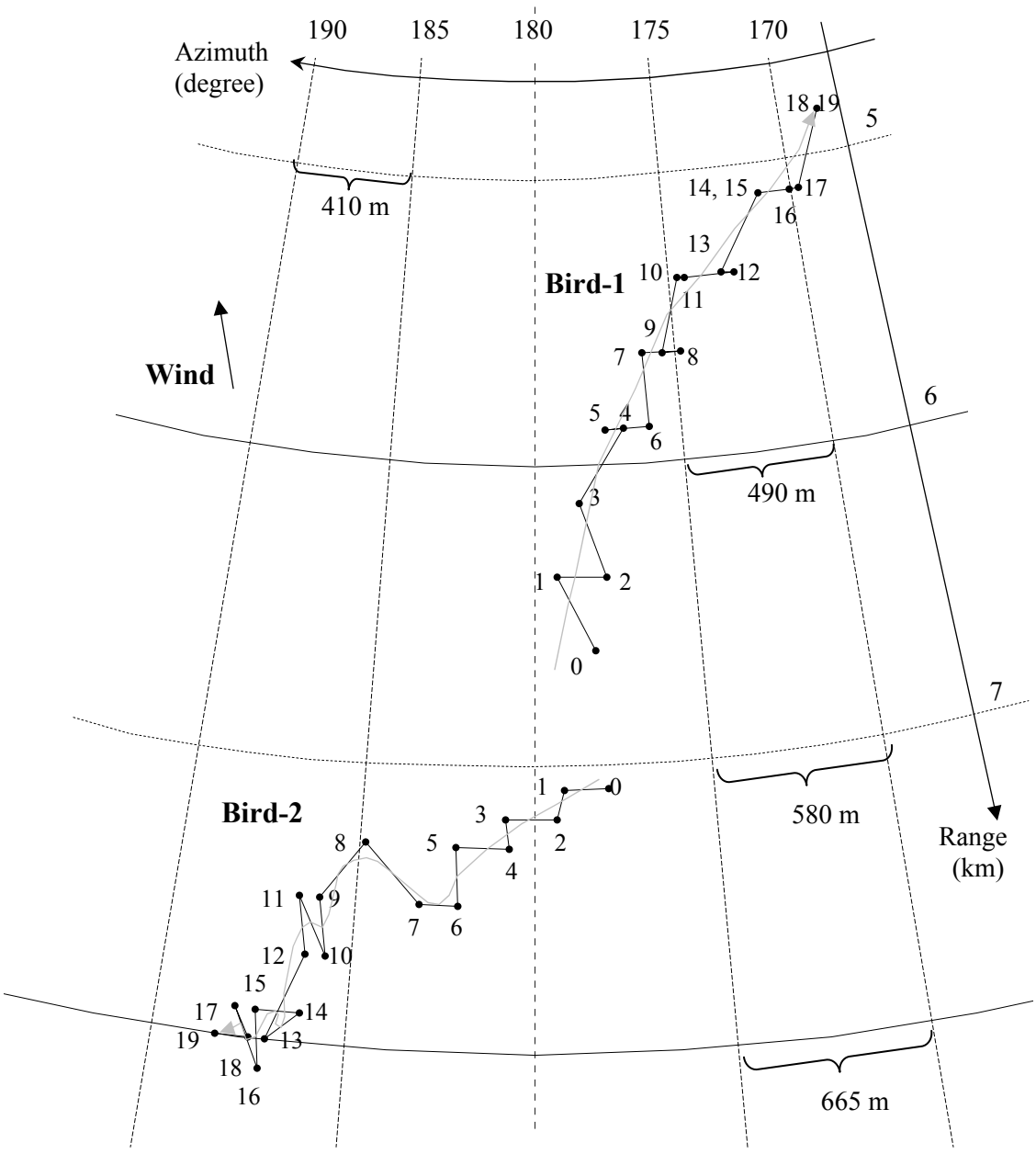

Fig 4.4: The trajectories of Bird-1 and Bird-2.
The direction of the wind is indicated. A 1° azimuth angle corresponds to 133 m at a range 8 km, and to 83 m at a range 5 km.

and fluctuate from 0.1×10^{-4} to 5.7×10^{-4} m^2. The variation (factor of 57) could be due to the bird orientation and its location in the resolution volume. The cross section value of Bird-2 exhibit similar behavior up to the 10th time cut; however, the variations in cross

section for later cuts are considerable. Large cross section values for time cuts 15, 16 and 17 imply presence of ground clutter or other birds in the resolution volume. The spectra for these time cuts are described in Section 4.2.

The spectrum of a single flying bird that is free from other scatterers consists of a narrow large maximum centered at the bird's radial velocity. Figure 4.7 displays such spectra for Bird-1 in the top two plots and for Bird-2 in the bottom two plots. The spectra to the left are from uniformly weighted time-series and the spectra to the right are obtained with the Von Hann windows. The solid line shows the spectrum at the gate with the bird. The dotted lines show spectra in neighboring gates. Maximum values in each plot correspond to the radial velocity of the bird.

The contribution due to the wing beating is not possible to distinguish. The double peak of Bird-2 (Figure 4.7 bottom left) is probably an indication of the presence of another bird in the resolution volume with a slightly larger radial velocity.

It is possible to identify the wind velocity from the uniformly weighted spectra for Bird-1, though it is not obvious. The spectra weighted with the Von Hann window demonstrates a well defined peak at –4 ms^{-1} with power –12 dB at the Bird-1 location and with power up to –5 dB at a neighboring to the Bird-1 range location. This peak is the wind velocity (Section 2.5.2). The wind velocity peak is easy to observe in both Bird-2 spectra.

Ground Clutter returns in Figure 4.7 are centered at zero velocity values and are small (in this particular radial) in comparison to the bird returns.

Table 4.1: Reflectivity and cross-section of Bird-1

Cut	Time t (h:m:s)	Target Range r (km)	Azimuth Angle θ (°)	Radial Velocity v (m/s)	Reflectivity Z (dBZ)	Equivalent Reflectivity Factor Z_e (mm^6m^{-3})	Reflectivity Per Unit Volume $\eta\times10^9$ ($mm^6m^{-3}m^{-4}$)	Cross-section σ_b (m^2)
0	10:29:21	6.63	178.2	12	4	3	0.007	0.1×10^{-4}
1	10:29:33	6.38	179.3	13	6	4	0.011	0.2×10^{-4}
2	10:29:39	6.38	177.8	12	16	40	0.113	1.7×10^{-4}
3	10:29:48	6.13	178.6	12	16	40	0.113	1.6×10^{-4}
4	10:29:56	5.88	177.1	16	18	63	0.180	2.3×10^{-4}
5	10:30:03	5.88	177.7	12	22	159	0.451	5.7×10^{-4}
6	10:30:10	5.88	176.2	16	20	100	0.285	3.6×10^{-4}
7	10:30:19	5.63	176.3	8	20	100	0.285	3.3×10^{-4}
8	10:30:26	5.63	175.0	12	18	63	0.180	2.1×10^{-4}
9	10:30:34	5.63	175.6	12	18	63	0.180	2.1×10^{-4}
10	10:30:42	5.38	174.9	12	14	25	0.072	0.8×10^{-4}
11	10:30:50	5.38	174.6	12	16	40	0.113	1.2×10^{-4}
12	10:30:57	5.38	172.8	10	14	25	0.072	0.8×10^{-4}
13	10:31:05	5.38	173.3	8	14	25	0.072	0.8×10^{-4}
14	10:31:12	5.13	171.5	0	22	159	0.451	4.4×10^{-4}
15	10:31:21	5.13	171.5	12	20	100	0.285	2.8×10^{-4}
16	10:31:28	5.13	170.3	10	20	100	0.285	2.8×10^{-4}
17	10:31:36	5.13	170.0	0	20	100	0.285	2.8×10^{-4}
18	10:31:43	4.88	168.7	10	20	100	0.285	2.5×10^{-4}
19	10:31:50	4.88	168.7	8	22	159	0.451	3.9×10^{-4}

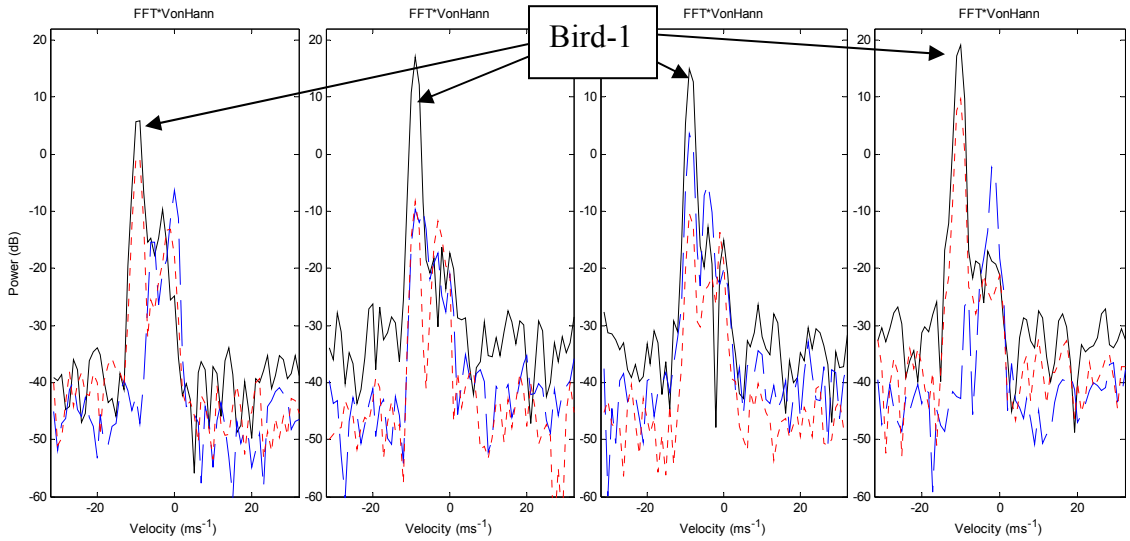

Figure 4.5: Bird-1 spectra. The locations of echoes for indicated cuts are given in Table 4.1. The solid line shows spectrum at the gate with Bird-1. The dotted and dashed lines show spectra from the neighboring gates. All spectra are weighted with the Von Hann window.

Table 4.2: Reflectivity and cross-section of Bird-2

Cut	Time t (h:m:s)	Target Range r (km)	Azimuth Angle θ (°)	Radial Velocty v (m/s)	Reflec-tivity Z (dBZ)	Equivalent Reflectivity Factor Z_e (mm^6m^{-3})	Reflectivity Per Unit Volume $\eta\times10^9$ ($mm^6m^{-3}m^{-4}$)	Cross-section σ_b (m^2)
0	10:29:21	7.1	178.0	+14	10	10.00	0.03	1×10^{-4}
1	10:29:33	7.1	179.2	+10	19	79.43	0.23	4×10^{-4}
2	10:29:39	7.2	179.4	+12	12	15.85	0.05	1×10^{-4}
3	10:29:48	7.2	180.8	+7	19	79.43	0.23	4×10^{-4}
4	10:29:56	7.3	180.7	+10	7	5.01	0.01	2×10^{-4}
5	10:30:03	7.3	182.1	+12	16	39.81	0.11	1×10^{-4}
6	10:30:10	7.5	182.0	+6	11	12.59	0.04	1×10^{-4}
7	10:30:19	7.5	183.0	+7	13	19.95	0.06	1×10^{-4}
8	10:30:26	7.3	184.5	+14	22	158.49	0.45	9×10^{-4}
9	10:30:34	7.5	185.6	+14	21	125.89	0.36	7×10^{-4}
10	10:30:42	7.7	185.3	+16	25	316.23	0.90	20×10^{-4}
11	10:30:50	7.5	186.1	+16	21	125.89	0.36	7×10^{-4}
12	10:30:57	7.7	185.8	+10	21	125.89	0.36	8×10^{-4}
13	10:31:05	8.0	186.6	+10	21	125.89	0.36	8×10^{-4}
14	10:31:12	7.9	185.8	+5	23	199.53	0.57	13×10^{-4}
15	10:31:21	7.9	186.9	+8	30	1000.00	2.85	65×10^{-4}
16	10:31:28	8.1	186.7	+8	34	2511.89	7.15	172×10^{-4}
17	10:31:36	7.9	187.4	+8	34	2511.89	7.15	163×10^{-4}
18	10:31:43	8.0	187.0	-13	30	1000.00	2.85	66×10^{-4}
19	10:31:50	8.0	187.8	-16	30	1000.00	2.85	66×10^{-4}

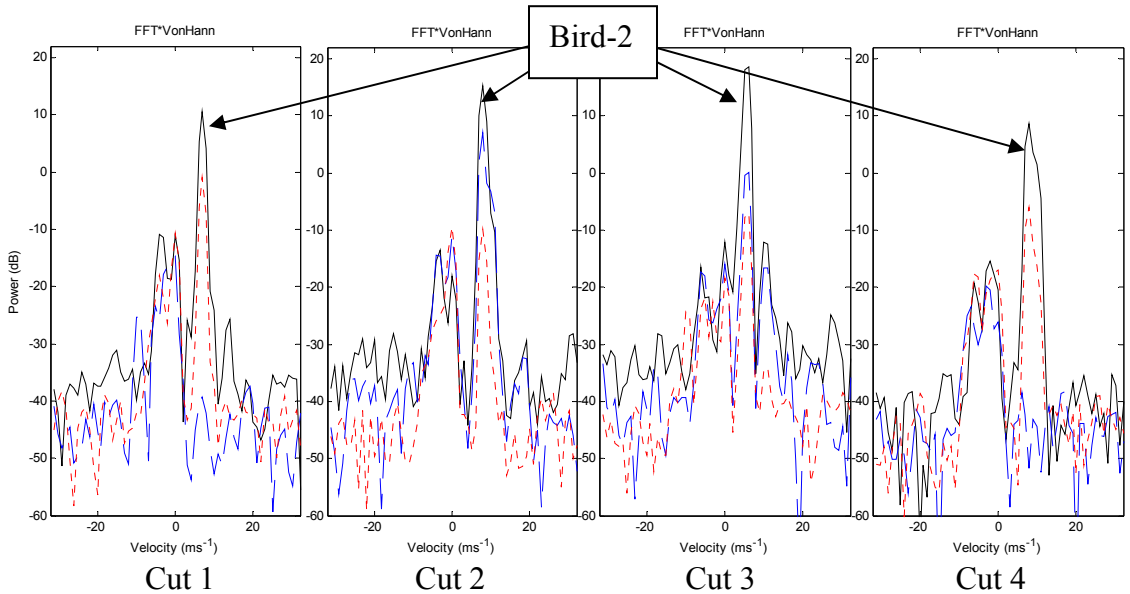

Figure 4.6: Bird-2 spectra. The locations of echoes for indicated cuts are given in Table 4.2. The solid line shows spectrum from the gate with Bird-2. The dotted and dashed lines show spectra from the neighboring gates. All spectra are weighted with the Von Hann window.

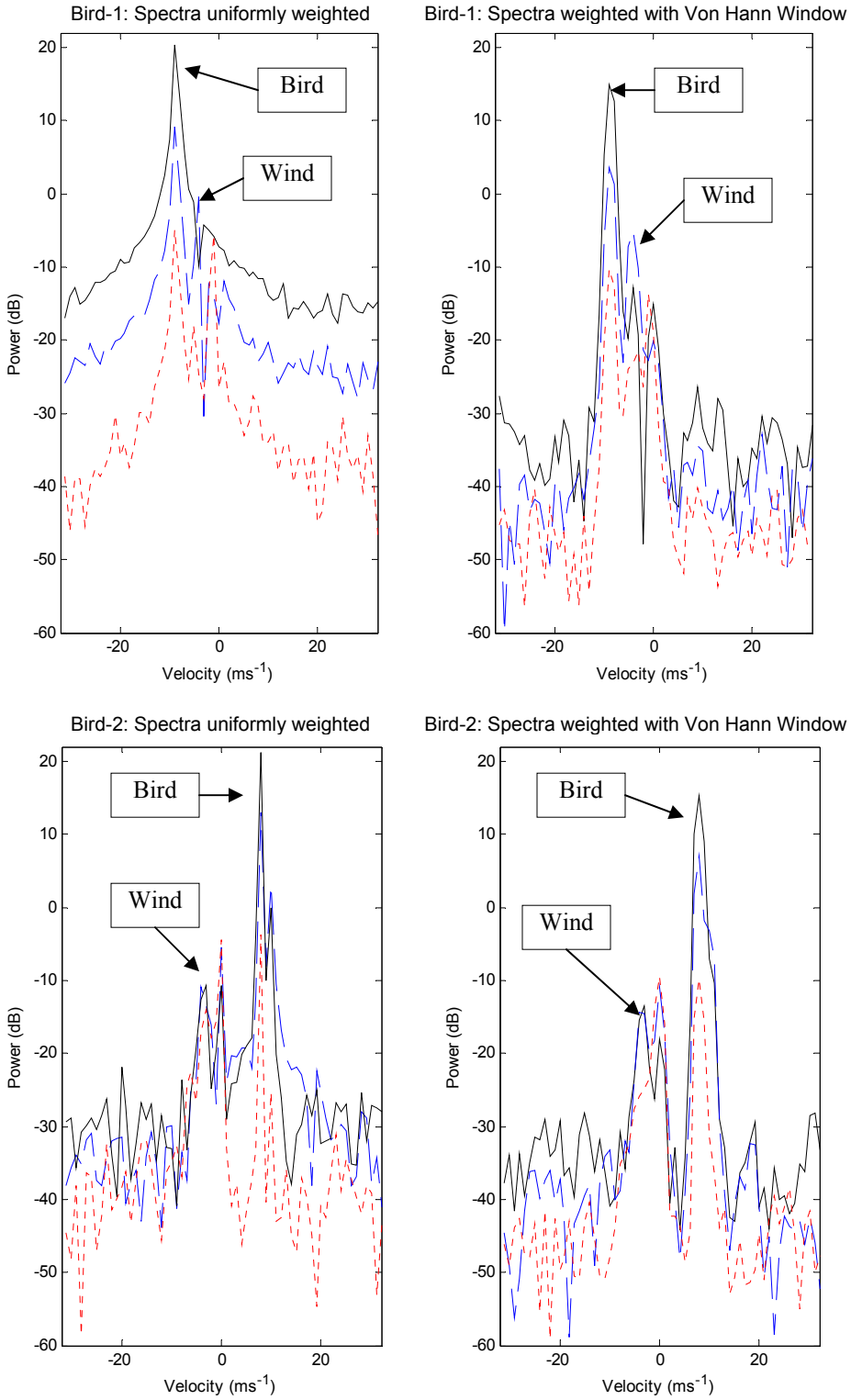

Figure 4.7: Single bird spectra. Spectra to the right are weighted with the Von Hann window. The solid line shows the spectra from the gate with the bird. The dotted lines show spectra from neighboring gates. Maximum in each plot corresponds to the radial velocity of the bird.

4.1.3 Simulation

A simple model of a flying bird is shown in Figure 4.8.

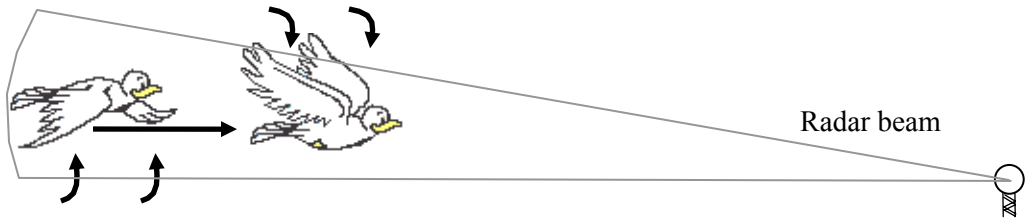

Figure 4.8: Simple model for detection of a signal scattered by a bird.
The radar beam hits the bird (bold black arrow) moving forward, and the wings moving up or down (black curved arrows) as indicated.

The underlying assumption is that the bird's cross section periodically changes with a position of the wings. Therefore the amplitude of the return can be approximated with a constant part due to the bird's body and a modulating part caused by the wings, as expressed in the following equation

$$y(k) = (A + B\sin\omega_1 k)\cos\omega_d k + j(A + B\sin\omega_1 k)\sin\omega_d k\,. \qquad (4.7.1)$$

A is the amplitude of a flying bird, B is the amplitude of a signal modulated by a wing beat, ω_d is the Doppler shift due to the bird movement, and ω_1 is the shift caused by wings moving up and down. Wings are thought to flap simultaneously, and therefore the shift is modeled as a sinusoid $\omega_1 = C\sin(2\pi F_{\text{beat}} t)\,|_{\,t = kT}$, where F_{beat} is the frequency of the beating wings, C is the amplitude, and $T = 7.8\times10^{-4}$. White noise is added to the signal (SNR ~30 dB). The modeled signal is sampled, and the discrete Fourier Transform (DFT) of the result is taken.

The variables in the simulation are wing beat frequency, and the values of amplitudes A, B, C. The shape of the spectrum for a signal without noise changes as follows. Define an extra peak on the slope of the peak corresponding to the radial velocity of a bird as a wing-beat-spike. A signal modulated by wing beating

demonstrates appearance of wing-beat-spikes on the slopes of the spectral peak for frequencies more then 8 Hz (Figure 4.9a, and 4.9b). Unfortunately large birds wings beating frequencies are less then 2 Hz which cannot be distinguished from the obtained spectra (Figure 4.9c and 4.9d).

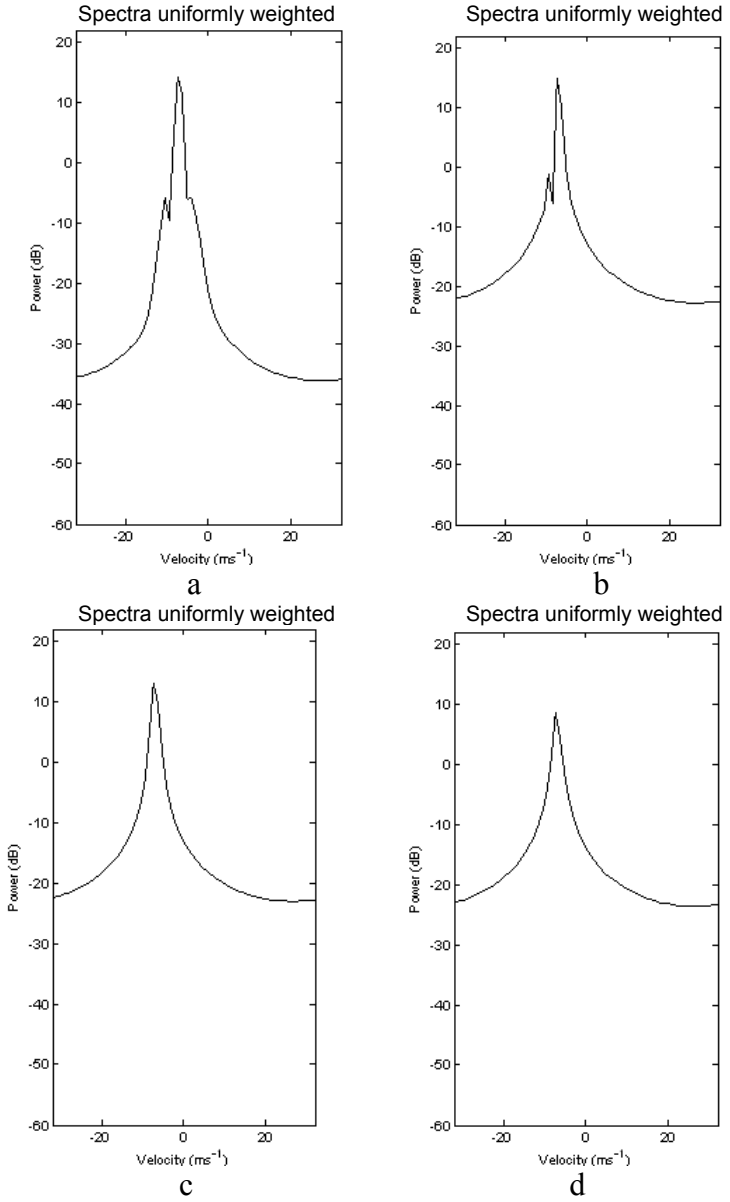

Figure 4.9: Wing beating simulation without noise. Velocity of the simulated bird 7ms^{-1}, wing beating frequency: (a) 12 Hz, (b) 8Hz, (c) 2 Hz, (d) 1Hz. An extra peak on the slope of the peak corresponding to the radial velocity of a bird is defined as a wing-beat-spike. The wing-beat-spikes are observed only at wing beating frequencies less then 2 Hz.

A bird signal was simulated with different radial velocities, wing beating frequencies (Figure 4.10 top), amplitudes of the bird body (Figure 4.10 bottom), and amplitudes of the wings.

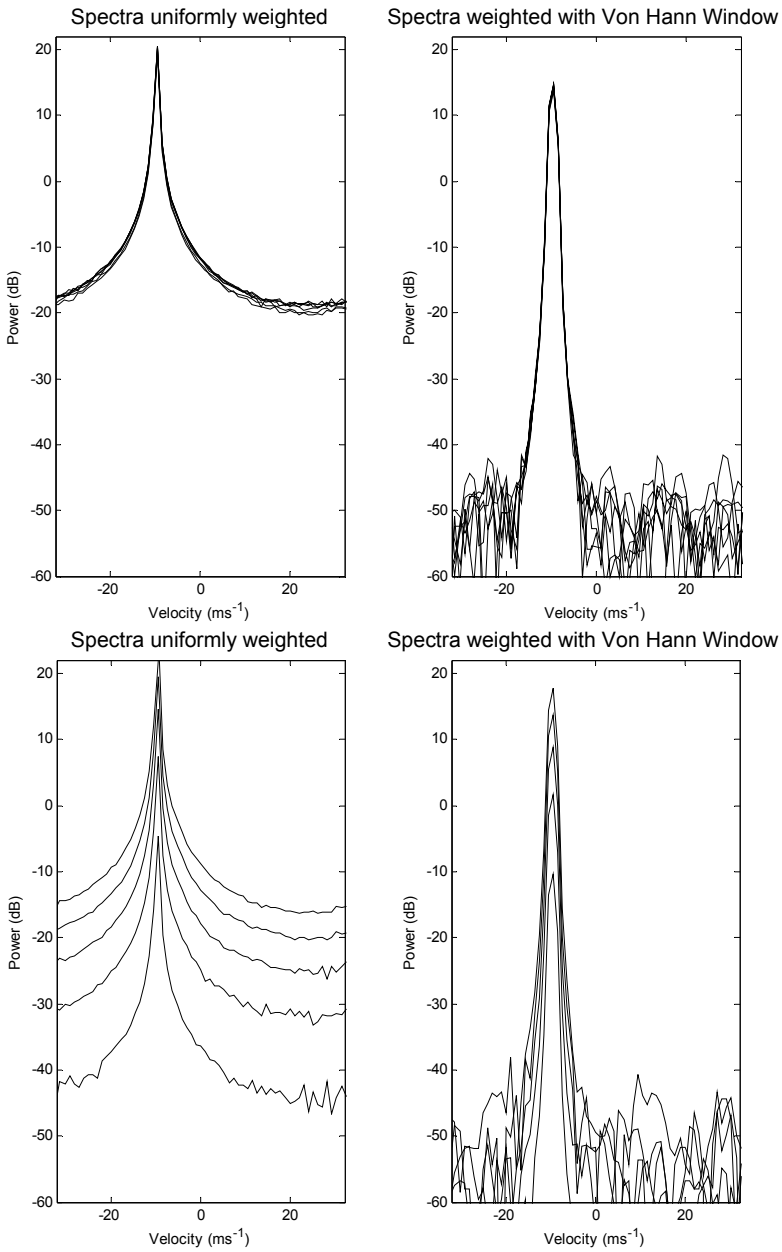

Figure 4.10: Example of variables for Bird-1 simulation with noise. Velocity of the simulated bird is 9 ms^{-1}.
Top: Wing beating frequencies are in the range from 0.1 Hz to 8 Hz;
Bottom: Amplitudes of the bird body are from 0.1 to 0.5.
The spectra to the left are uniformly weighted, while the spectra to the right are weighted with the Von Hann window.

The wing beating frequency cannot be observed in presented spectra. The strength of the radial velocity peak in spectra depends on the bird's body amplitude. Larger bird shows stronger signal with the same SNR. The best matches of the modeled spectra for Bird-1 and Bird-2 are shown in Figure 4.11a and 4.11b, respectively.

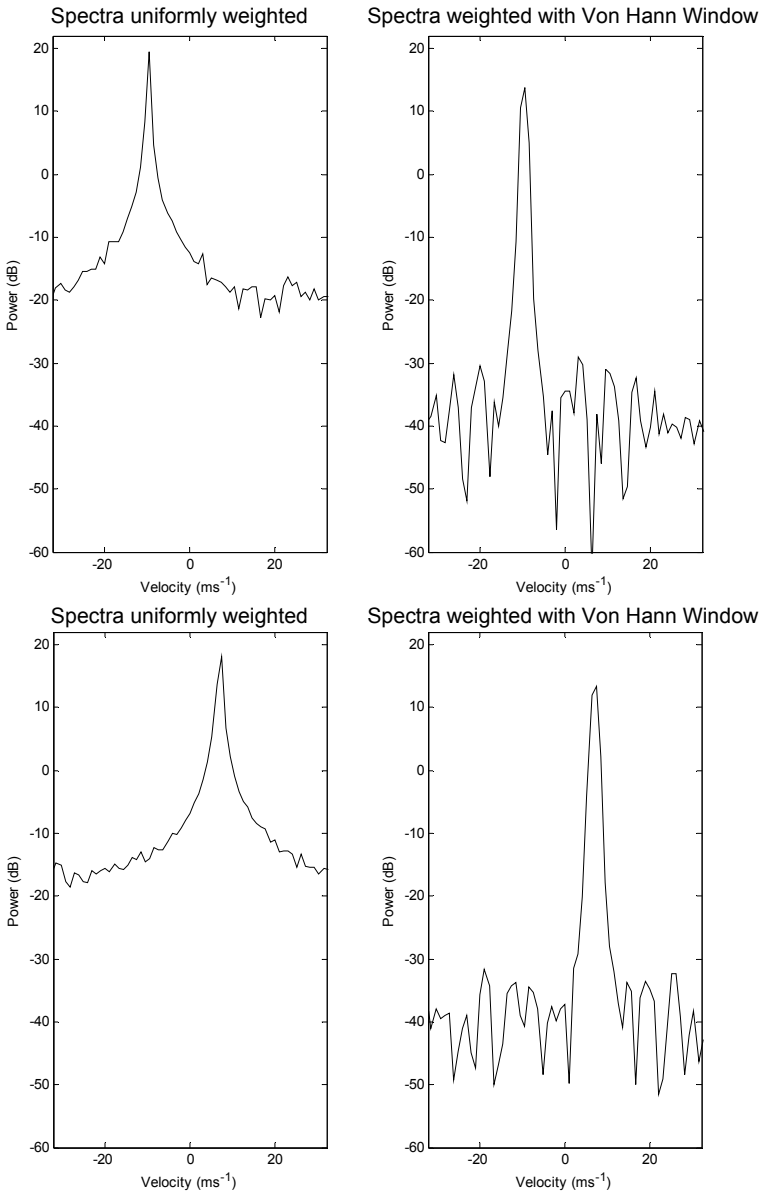

Figure 4.11: Birds simulation.
Top: Bird-1 spectra: radial velocity 9.6 ms^{-1} (A=0.4, B=0.1, C=1).
Bottom: Bird-2 spectra: radial velocity 6.9 ms^{-1} (A=0.1, B=0.3, C=1).
The spectra to the left are uniformly weighted, while the spectra to the right are weighted with the Von Hann window.

The modeled Bird-1 and Bird-2 radial velocities are 9.6 ms^{-1} and 6.9 ms^{-1}, respectively. The amplitudes for Bird-1 are A=0.4, B=0.1, C=1, when those for Bird-2 are A=0.1, B=0.3, C=1. Bird-1 is simulated to have big body and small wings (ratio 4/1), when Bird-2 has a small body and large wings (ratio 1/3). But overall, Bird-1 is supposed to be a little larger then Bird-2 (ratio 4/3) and this can be seen from the spectra.

Clear-air wind can be included in the simulation as shown in Figure 4.12. The spectrum of Bird-1, shown in Figure 4.7 in the top plots is matched with the spectrum of the modeled signal with additive wind 4 ms^{-1}, bird radial velocity 7 ms^{-1}.

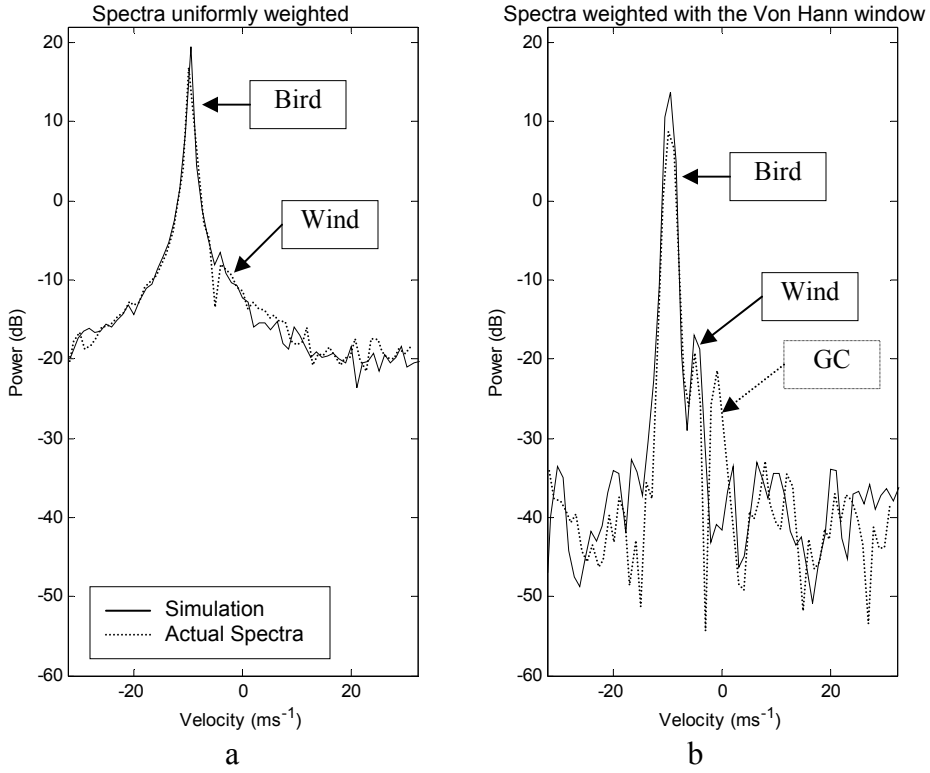

Figure 4.12: Bird-1 with the wind simulation.
(a) Spectrum of Bird-1 uniformly weighted.
(b) Spectrum of Bird-1 weighted with the Von Hann window.
Solid line indicates simulated spectrum. Dotted line shows actual spectrum. Note presence of the ground clutter (GC) in the actual spectrum. Bird- and wind- radial velocities are indicated.

4.2 Multiple Birds from data set 3/26

Several spectra of multiple birds taken at the locations with registered Bird-2 echo are shown in Figure 4.13. All spectra are weighted with the Von Hann window.

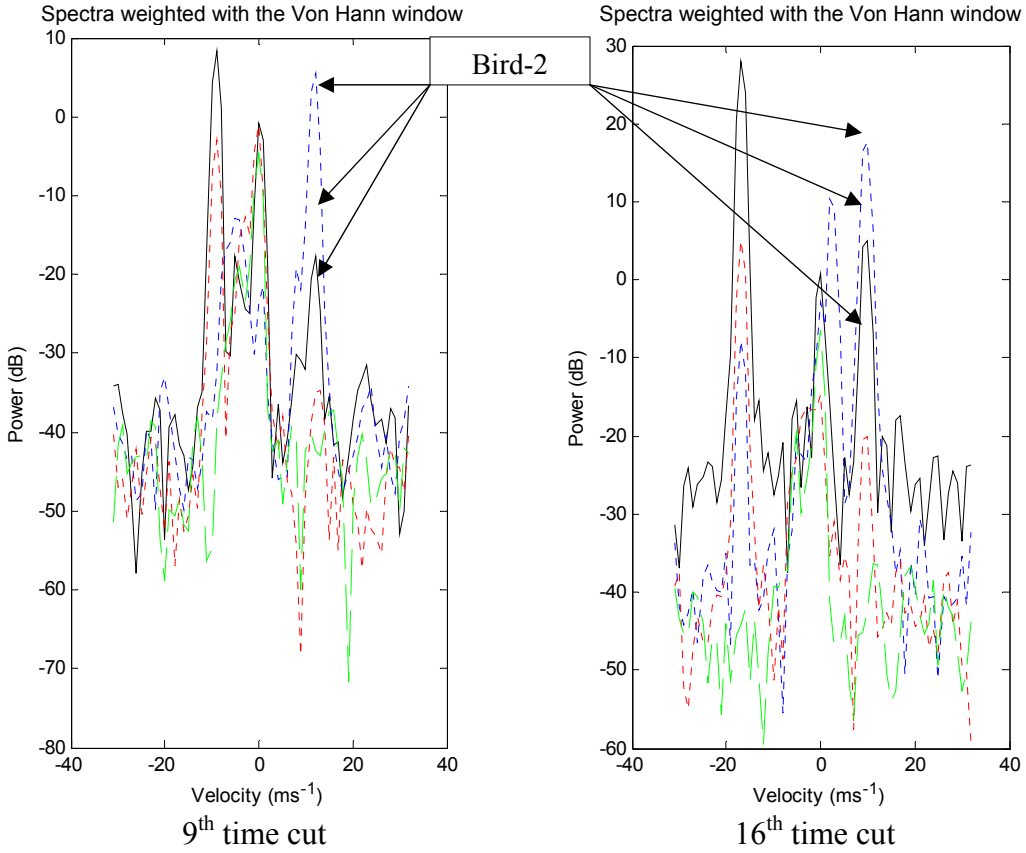

Figure 4.13: Multiple birds' spectra. All spectra are weighted with the Von Hann window. The solid line shows the spectra at the gate with the registered bird. The dotted lines show spectra in neighboring gates. The dashed line shows clear-air spectrum. Local maxima in each plot correspond to the radial velocity of birds.

The local maxima corresponding to zero velocity are assumed due to ground clutter. Other local maxima correspond to the radial velocity of the birds. Obviously, one of the maxima (indicated by arrow) is contributed by Bird-2 tracked in Section 4.1. The solid lines in the spectra for the 9th and the 16th time cuts and their neighbors show several birds flying in different directions, and ground clutter. Due to the spread of the range dependant weighting function, the spectrum at a gate is affected by the signals in the

neighboring gates. In other words, a point scatterer is detectable in its neighboring resolution volumes. This phenomenon causes the spectra for the 16th time cut in Figure 4.13 to show a repetition (in neighboring gates) of peaks for Bird-2 flying at about 15 ms^{-1} toward radar, and a repetition of peaks for another bird moving at about 10 ms away from the radar. There is another peak in this spectra corresponding to the radial velocity about 5 ms^{-1} away from the radar. This one does not display repetition in neighboring gates probably because it is on the edge of the neighborhood of the detectable cluster.

4.3 Multiple Birds from data set 5/8

Data 5/8 was collected after a tornadic super-cell. The PPI of RRAT (Figure 4.14a and 4.14b) shows small reflectivity values ranging from -5dBZ to +15dBZ at ranges up to 40 km, and velocities with values from -32 ms^{-1} to +32 ms^{-1}. A part of PPI is magnified to display features (Figure 4.14c and 4.14d). The sounding (Table 4.3) shows that the wind speed was varying from 32 knots to 35 knots (16.5 – 18 ms^{-1}), and then calmed down to 24 knots. Radar meteorologists claimed that these echoes are from biological scatterers and the wind from South.

Table 4.3: Sounding 72357 OUN Norman Observations at

Time & Date	Height, m	Direction, degree	Speed, Knot	Reference http://weather.uwyo.edu/cgi-bin/sounding?region=naconf&TYPE=TEXT%3ALIST&
12Z 5/8 2003	610 686 914	170 170 180	34 32 35	YEAR=2003&MONTH=05&FROM=0812&TO=0900&STNM=72357
00Z 5/9 2003	610 719 814 914	210 215 222 230	24 22 21 19	YEAR=2003&MONTH=05&FROM=0900&TO=0912&STNM=72357

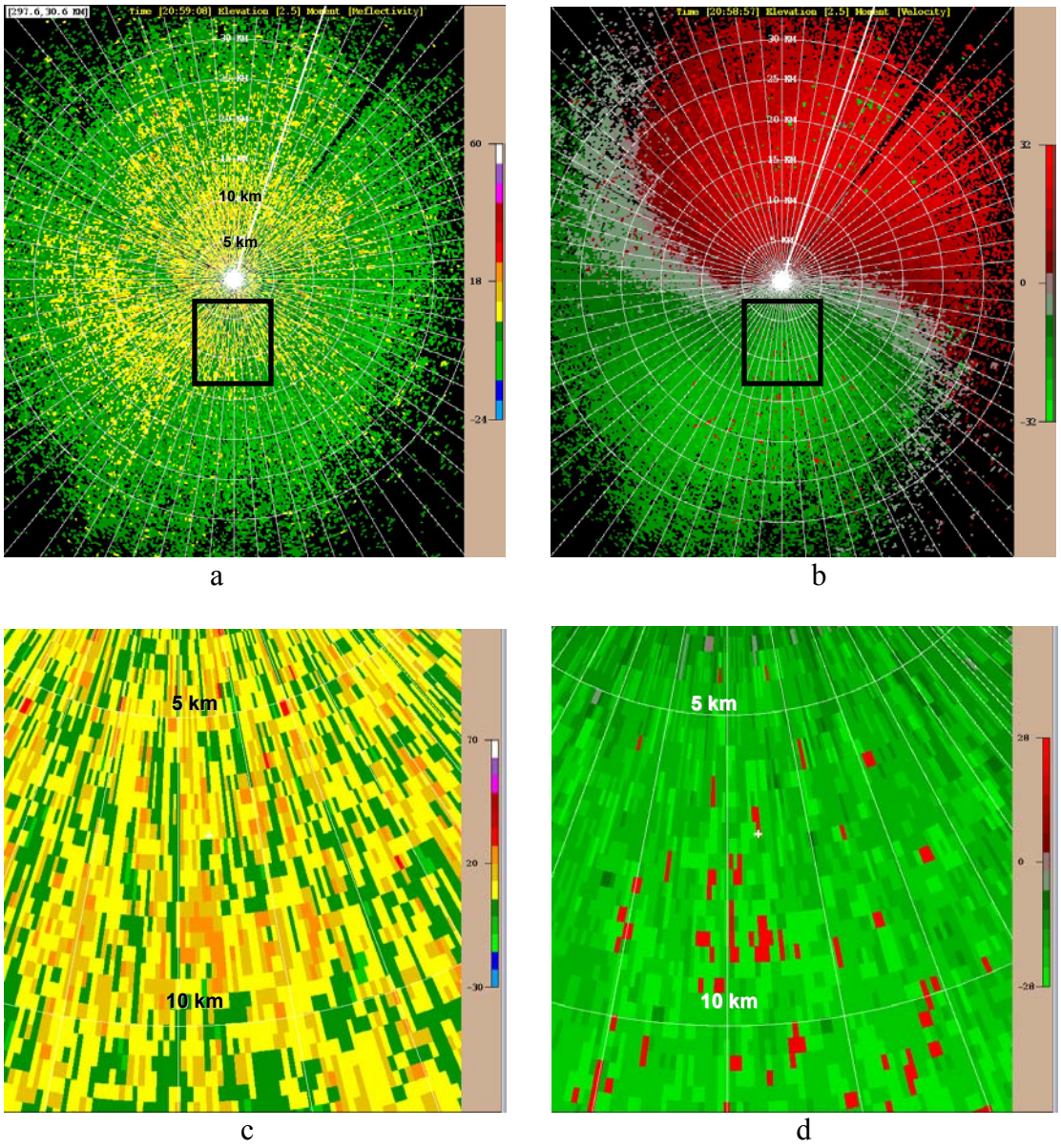

Figure 4.14: Cut 3, elevation 2.5°, PRT 986 μs.
(a) Reflectivity PPI. (b) Velocity PPI. Areas between 5 and 10 km south from the radar as indicated by squares in (a) and (b) are magnified in (c) and (d). Range rings are 5 km apart.

Radial 176° and its neighbors 175.5° and 176.5° are chosen arbitrarily to explore the echo features. Echo power along the chosen radials is shown in Figure 4.15. The beam's elevation is 2.5°; therefore, only close ranges (5-10 km, corresponding to 20th

through 40th range gates, and height below 1 km) are considered for observing how the velocities of birds influence the wind estimates.

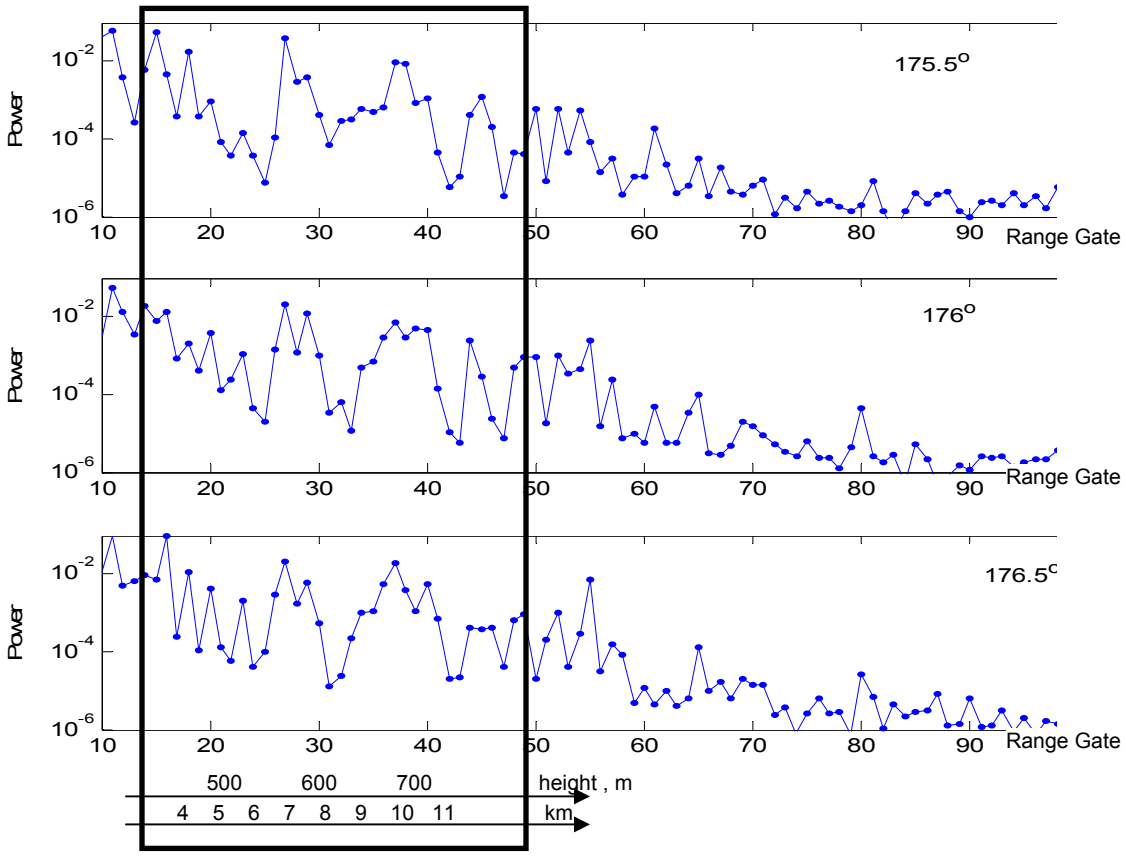

Figure 4.15: Return Power for 3 neighboring radials 175.5°, 176°, 176.5°

The spectra in the figures below are organized in the following manner. Each row of figures displays the spectra at the stated range gate and its 8 neighbors (Figure 4.16).

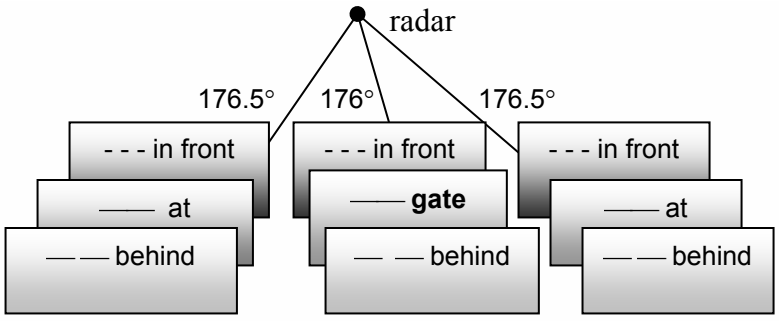

Figure 4.16: The concept 9 neighbors. Radar is radiating toward the reader.

The spectra of the gates evaluated in Table 4.4 are estimated.

Table 4.4: The target solutions for several gates of the chosen radials

Range gate	Range, km	Height, M	RRAT Z, dB			RRAT Velocity, ms^{-1}			Ground Clutter observation in spectra, Z, dB
			175.5°	176°	176.5°	175.5°	176°	176.5°	
15	3.5	450	4	10	7				Above 10
16	3.75	460	4	10	7	-13	-16	-12	Above 10
18	4	490	5	5	6	-12	-14	-15	Below 0
22	5	510	8	8	12	-21	-18	-14	Below 0
23	5.5	530	1	3	1	-14	-18	-17	Below 0
27	6.25	570	9	16	9	-27	-27	-27	Below-10
29	6.75	590	8	10	11	28	-24	-27	None
32	7.5	620	11	5	14	-26	-20	-20	Below -20
34	8	650	12	17	19	-18	-27	-26	Below-20
36	8.75	670	26	22	25	27	27	27	Below -5
37	9	690	25	21	20	-28	28	27	Below-5
39	9.25	710	17	20	21	-23	-25	-27	None
40	9.5	720	12	9	11	-19	-21	-27	None
44	10.5	760	5	3	10	-20	-20	-26	Below -15
45	10.75	770	3	4	16	-20	-20	22	Below -20
48	11.5	810	8	16	20	-24	27	27	Below -20

All spectra demonstrate broad multiple peaks of low power. Each spectrum shows a peak at a velocity of approximately -20 ms^{-1}. Slow small change in spectral peak intensity between -10 and -15 dBZ and gradual change in velocity of the peak from -16 ms^{-1} to -20 ms^{-1} convinced me to assume that the peak is caused by the wind. The assumed wind velocity values are smaller than those in Table 4.4. The zero-velocity peak that was observed in many spectra corresponds to ground clutter and is visible in all 9 neighbors. The other peaks are due to birds, e.g. gate 15 (–22 ms^{-1}), gate 16 (–22 ms^{-1}), gate 18 (–22ms^{-1}, -25 ms^{-1}), gate 29 (–26 ms^{-1}), gate 32 (–10 ms^{-1}), gate 34 (+22 ms^{-1}, –10 ms^{-1}), and so on. The velocities of birds are larger than those of the wind and cause higher estimates in Table 4.4 and on the velocity displays. The spectra of the gate 27th 9-neighbohood (Figure 4.17) show that the wind velocity is

distinguishable from the bird velocities. For resolving data contaminated by migrating bird velocity it is necessary to inspect the spectra for 2 (or more) peaks.

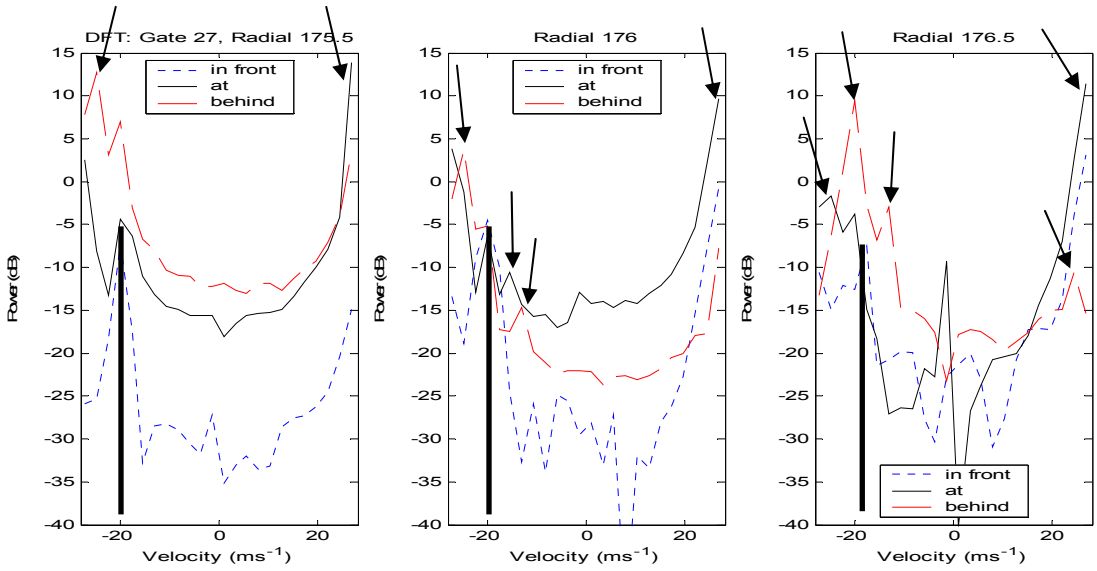

Figure 4.17: Distinguishing between wind and birds velocities.
Solid bold line indicates the wind velocity. Birds are shown with arrows. All spectra are weighted with the Von Hann window. The spectra are displayed using the 9-neighborhood concept presented in Figure 4.16.

4.4 Conclusion

Bird echoes can be recognized and modeled, therefore the impact of the bird presence in the weather signal can be investigated. The beating of the wings cannot be observed in the regular spectra due to limited resolution however it needs to be studied with a stationary antenna.

Understanding of bird flight physics can help prepare adaptive techniques to filter a bird echo from the weather signal and to enhance bird signatures for ornithological studies. The wind data contaminated by migrating birds can be resolved by eliminating bird-caused peaks in the spectra, because bird velocities usually differ from the wind velocity. Maximum velocity in velocity azimuth display can be used for separation. Point birds can be easily seen in spectrum.

5. Ground Clutter

The purpose of this chapter is to show how a ground clutter signal can be used to check radar performance and even improve it. The return from the tower (Figure 5.1) is used to test the phase shifter of the radar. The structure is located at latitude 35°23′27″ and longitude 97°45′25″ (Jct. Hwy. 92 and 152 Mustang, OK). Ground elevation is 413.6 meters. Overall height above ground is 151.2 meters. Overall height above mean sea level is 564.8 m.

Figure 5.1: The tower.

In [10] it was established that a phase shifter rms (root mean square) noise less than 0.2° is sufficient for good performance of the systematic SZ coding scheme. The achieved phase is stable but differs from the commanded phase. In the time series data

collected with the KOUN radar, the phases of the phase shifter differ from the exact SZ phases. Hence the following two issues concerning the phase shifter are pertinent for the SZ phase coding scheme: (1) what phases to use for decoding the time series data, and (2) how to determine these exact phases in the operational system, i.e. from pulse to pulse measurement or via periodic calibration. In principle the phase stability of the system can be obtained from the measurement of the transmitted pulse. But this was not yet available on the KOUN radar. Therefore, closed loop measurements were performed on the return echoes to determine the exact phases for decoding the phase coded data. The antenna was stationary at the direction of the tower, and radiated pulses with PRT of 780 μs. Phase coded and non-coded time series data of echoes from the tower were recorded. Two data sets are discussed in this work. One was obtained on Feb 10, 2003 (02/10) and the other on April 2, 2003 (04/02) with the antenna pointed at azimuth 306 degree, and elevation 0.3 degree. A radial of time series data consists of 468 *I-Q* samples consecutive in range-time and one record contains 64 radials of such data. The power of the return signal in logarithmic units for one such record of the first set is in Figure 5.2a and of the second set it is in Figure 5.3a. The test set for the estimation of the phase change consists of 100 records.

5.1. Tower from data 2/10

There was no precipitation and a very light wind (about 3 ms^{-1}) on February 10. The 119^{th} range gate (29.125 km) in Figure 5.2a samples what is considered a strong (signal to noise ratio SNR of about 50 dB) return signal from a well defined point scatterer. This signal at 29.125 km from the antenna was chosen for estimating the stability and repeatability of the phase sequence generated by the phase shifter. The

commanded phase used for phase-coding of the transmitted signal is given in degrees in the Appendix (Table A.1, column 2). All phases are in the range –180° to 180°. The arguments for computing the phase of the returned signals were constructed from computations listed in Table 5.1, where *i* refers to a record number. The estimated mean of measured phases is an average of *N* sample phases

$$\Psi_{\mathrm{k}} = \frac{1}{N}\sum_{i=1}^{N} \arg\left(V_1 \cdot V_k^*\right), \tag{5.1}$$

where $N = 100$, $k = \{1, 2, 3, ..64\}$ is the radial separated from the first radial by k PRTs, it corresponds to the k^{th} phase shift of the switching code. Computed phases Ψ_{k} are given in Table A.1, column 3. Differences $\Delta\Psi_{\mathrm{k}}$ between the original commanded and calculated mean phase sequences are quite small and indicate how close the values of the phases are. These differences are shown in Table A.1, column 4. The maximum difference is less then 1.14° and the rms $\Delta\Psi_{\mathrm{rms}}$ of the differences is 0.67°. The standard deviation of the estimated phases is shown in Table A.1, column 5 for each designated phase of the code. The rms of standard deviation is less then 0.74 degrees. Average bias, which is the average of all values in column 4, is 0.02°.

Argument of the first pulse with conjugate of every other pulse, used for computing the phase of the return signal samples is shown in Table 5.1

Table 5.1: Argument for computing the phase

i	**Phase of the**				**Phase in general**
	1st pulse	**2nd pulse**	**…**	**64th pulse**	
1.	Arg(V_1V_1*)	Arg(V_1V_2*)	…	arg(V_1V_{64}*)	arg(V_1V_k*)
2.	Arg(V_1V_1*)	Arg(V_1V_2*)	…	arg(V_1V_{64}*)	arg(V_1V_k*)
:	:	:		:	:
100.	Arg(V_1V_1*)	Arg(V_1V_2*)	…	arg(V_1V_{64}*)	arg(V_1V_k*)

Coded data is decoded for the first trip echo according to

$$V_k[decoded] = V_k \cdot \exp\left(j\Psi_k \cdot 2\pi/360\right), \tag{5.2}$$

where Ψ_k is phase in degrees, and could be either commanded or estimated. The absence of exact match between the sequences of the commanded and the estimated phases might lead to an error propagation in decoding of the coded data, and, therefore to degradation of performance. To quantify the effects of this error on the spectra the data was decoded by using commanded phase and estimated phase sequences.

Let the sequence of the DFT of decoded data be F_k , e.g., F_k = DFT{V_k [*decoded*]}. The average power spectra of the obtained sequences over 100 records is then found according to

$$S_k = \frac{1}{N}\sum_{i=1}^{N}\left|F_k\right|_i^2 . \tag{5.3}$$

The average power spectra for the commanded phase, and computed phase are shown in Figure 5.2b. The signal to total spectral noise ratio *SNR* can be defined

$$SNR = |V_1|^2 / \sum_{i=2}^{64}\left|V_i\right|^2 , \tag{5.4}$$

where the DC coefficient V_1, or the maximum value in power spectra is a vector, that fluctuates due to the phase instability. V_1 oscillate a little less for the signal decoded with estimated phases, which can be seen from Table 5.2 section 5.3, showing the calculation results. The decoding with the estimated phase allowed achieving an improvement in the SNR of the returned signal, summarized in Table 5.2.

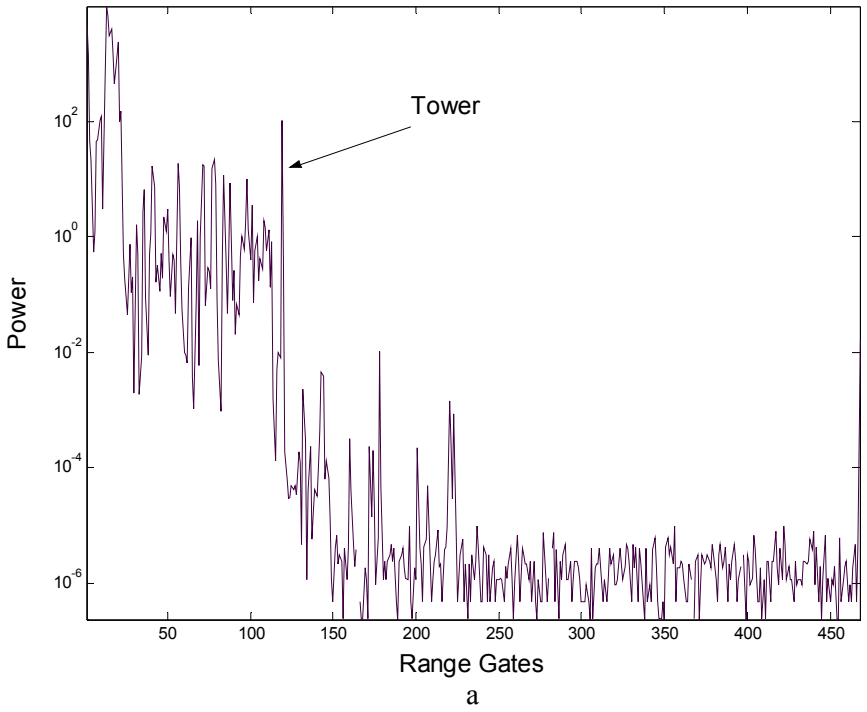

a

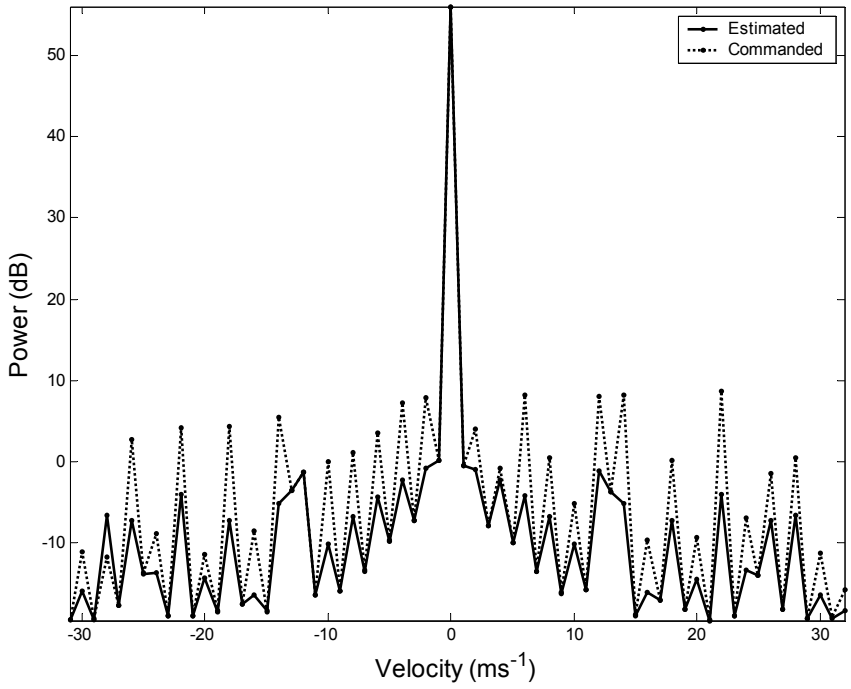

b

Figure 5.2: Data 2/10.
(a) The power of the return signal for one record 2/10. The tower is located at the 119th range gate 29.1 km from the antenna. (b) The power spectra of the indicated tower. The dotted line shows the averaged spectrum of the signals decoded with commanded phase, and the solid line shows the spectrum of the signal decoded with the estimated phases.

5.2. Tower from data 4/02

To confirm the result of the section 5.1 another set of data 4/02 was obtained on a different day with a stationary antenna pointed at approximately the same azimuth, and elevation angles. There was no precipitation on this date; however, the wind conditions were different from 2/10. There were registered winds of 10 ms^{-1} gusting to 15 ms^{-1}. The power of the return signal in logarithmic units is shown in Figure 5.3a. The average power spectra of the tower return decoded with commanded and estimated phases are shown in Figure 5.3b. The values of the commanded and estimated phases and their difference are given in the Table A2 of appendix. The maximum difference is less then 0.66° and the rms of the differences $\Delta\Psi_{rms}$ is 0.23°. Standard deviation of estimated phases is shown in Table A.2, column 5 for each designated phase of the code. The rms of standard deviation is 0.56°. Average bias is 0.04°.

Estimated phases Ψ_k for 2/10 and 4/02 are not exactly the same. The differences between the estimated phases are shown in the Appendix (Table A.3, column 5), and are in the range –0.7° to 0.3°. To check the consistency of the phases the tower returns from either days were decoded with each estimated phase codes for the other day. The data 4/02 decoded with the phase estimated for the data 02/10, and the data 2/10 decoded with estimated phase from 4/02, are shown in Figure 5.4a and 5.4b respectively. The estimated phase spectrum is below the commanded phase spectrum indicating lower noise.

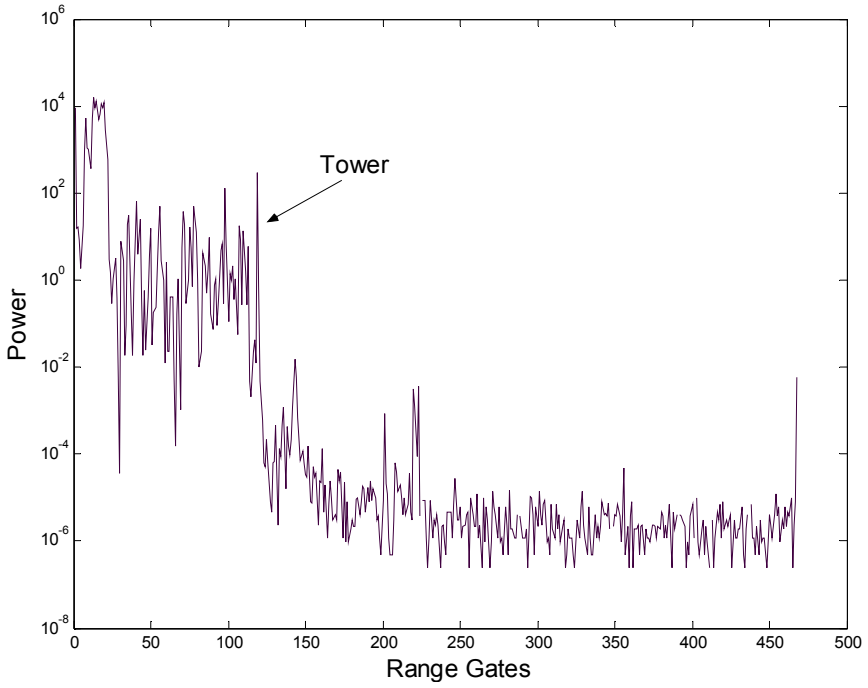

a

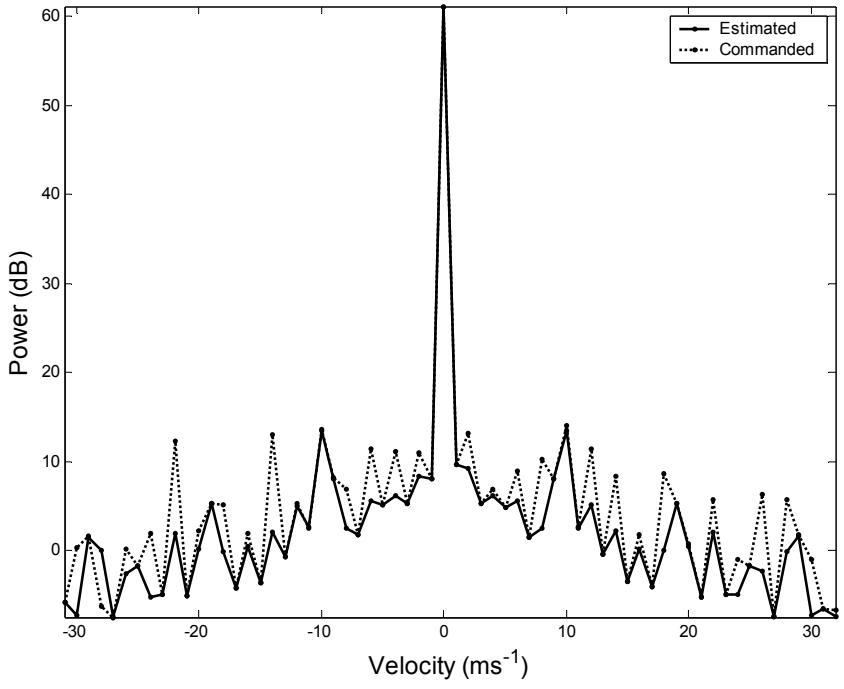

b

Figure 5.3: Data 4/02.
(a) The power of the return signals for one record 4/02. (b) The power spectra of the indicated tower. The dotted and solid line show spectrum of the signal decoded with the commanded and estimated phases, respectively.

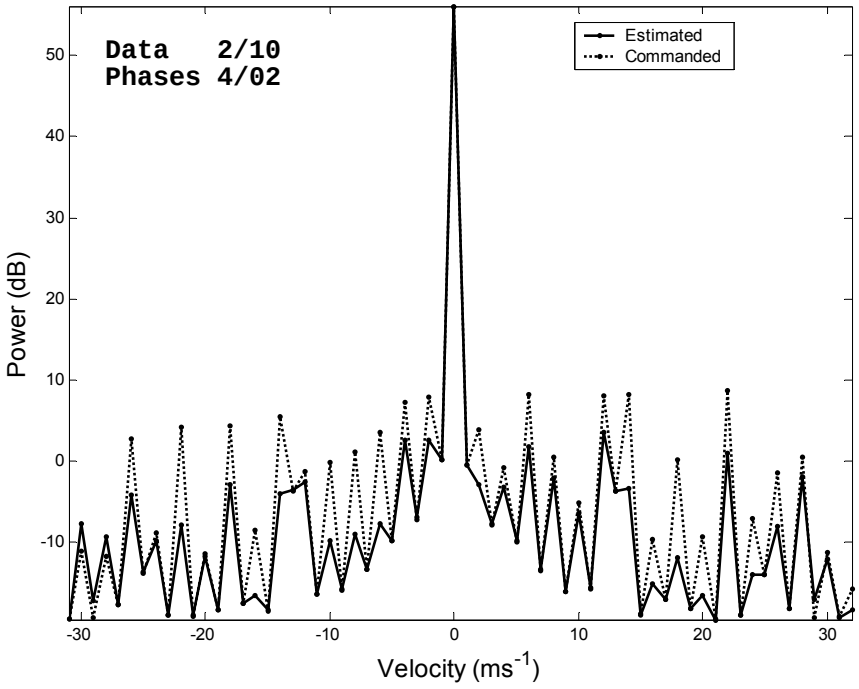

a

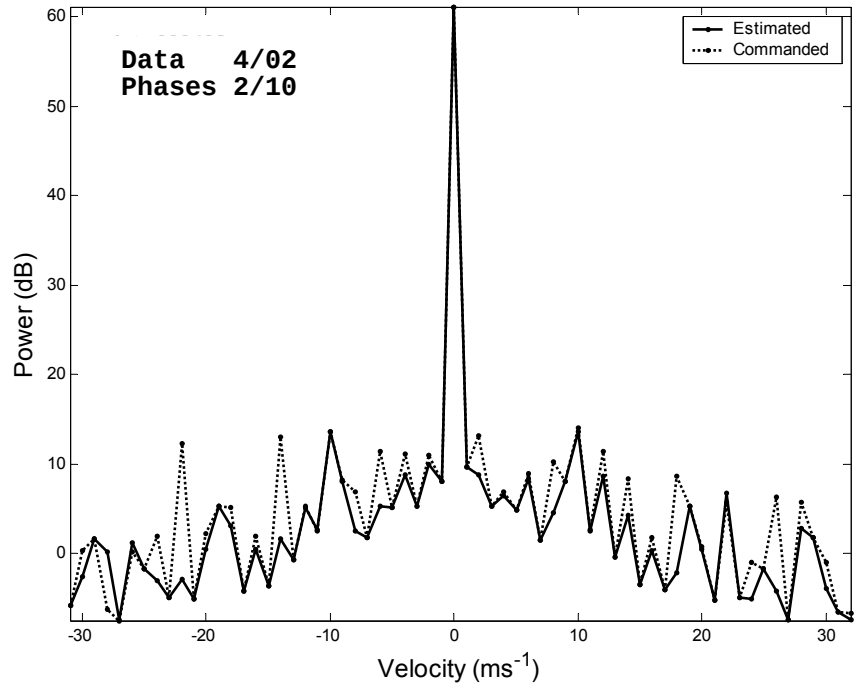

b

Figure 5.4: The power spectra of a tower return.
(a) The spectra from data 2/10 decoded with phases estimated on 4/02. (b) The spectra from data 4/02 decoded with phases estimated on 2/10. Dashed lines show spectra of the signals decoded with commanded phases. Solid lines show spectra of the signals decoded with estimated phases.

5.3 Summary of decoding results

To compare of the coding technique the tower return were collected with no-coding and with phase coding options. Figures 5.5a and 5.5b show spectra of the tower return decoded with (1) commanded phases, (2) average of estimated phases, (3) estimating phases for each record, and spectra of the signal collected without phase coding. It is noteworthy that on both days the commanded phases produced the largest spectral side lobes, about 45 dB below the peak. Decoding of the time series data with phases estimated for each radial dwell of time series data (64 pulses) (labeled one by one in the figures) produces the lowest side lobes. The values of SNR are summarized in Table 5.2.

Table 5.2: SNR summary

	For data 2/10				for data 4/02			
	No Coding	Com-manded Phase	Estimated Phases		No Coding	Com-manded Phase	Estimated Phases	
			Average	Individual			Average	Individual
DC	420078	401092	401147	401151	420078	401092	401147	401151
SNR dB	24247 43.85	5951 37.75	32146 45.07	52928 47.24	5773 37.61	4838 36.47	7850 38.94	50234 47.01
1/*SNR*	0.006	0.013	0.006	0.004	0.013	0.015	0.011	0.005
Maximum difference compare to Commanded phase (°)			1.14	2.20			1.02	4.52
$\Delta\Psi_{rms}$ (°)			0.67	0.74			0.45	0.98
Improved (dB)			7.32	9.49			2.47	10.54

Use of the commanded phases consistently results in the lowest SNR which are comparable for the two days. Also comparable are the SNRs if the measured phase sequence of each record is applied to decode the record.

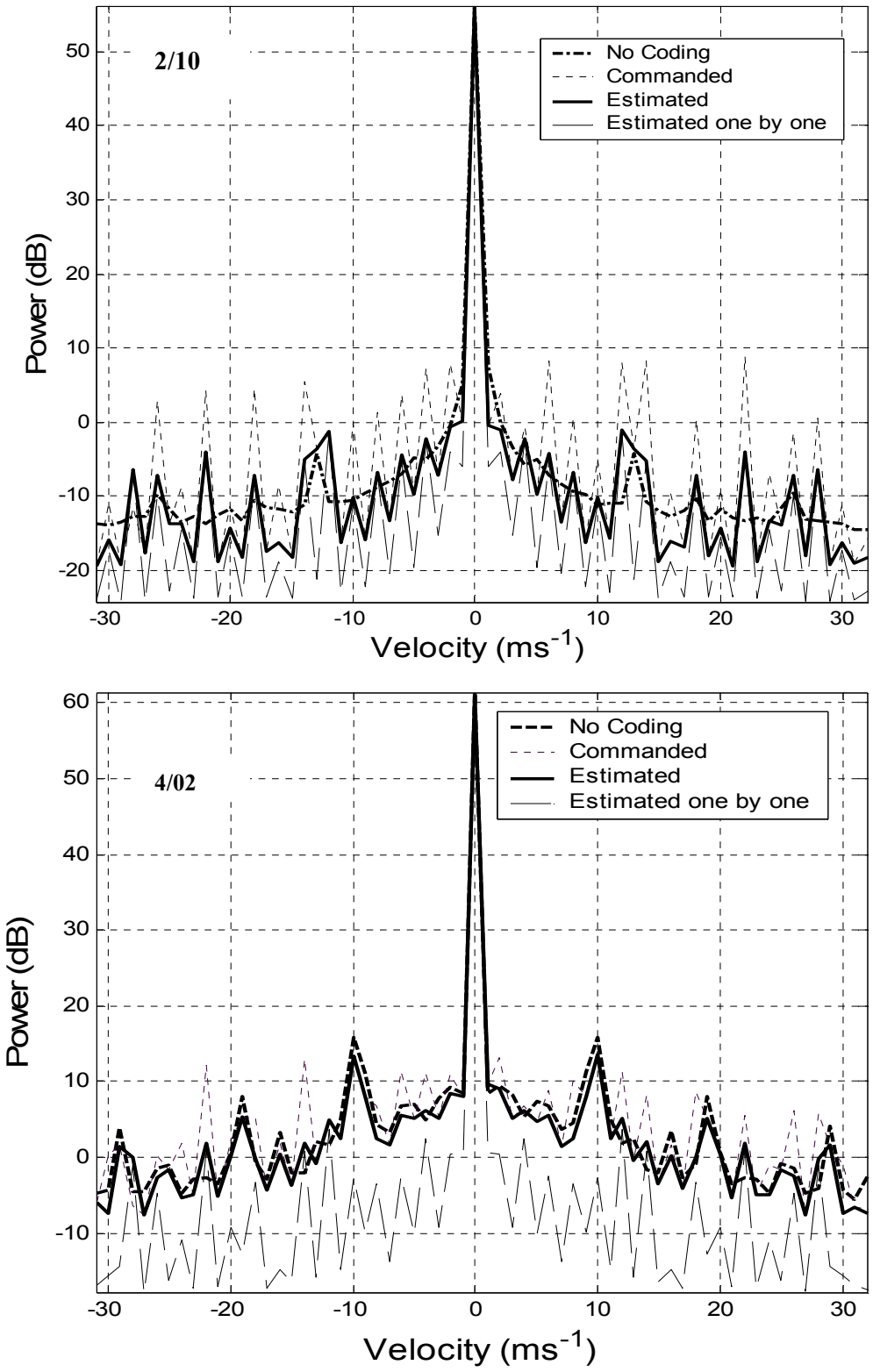

Figure 5.5: Power spectra of sequences decoded using various phase estimates. Top plots show spectra for tower 2/10, bottom plots show spectra for tower 4/02.

This is expected as such individual correction may compensate for some propagation effects. Improvements in the SNR with respect to the lowest values (obtained with commanded phases) for the two days are listed in the last row of Table 5.2. The phase shifter is stable. The reasons for significant difference in the SNRs between the two days and for the cases where there was no phase coding and when the average of estimates was used are not known. The fact that individually measured (over the record equal to the code length of 64 samples) phases gives the best SNR suggests that instantaneous sampling of the phase of the transmitted signal (such as done by the RVP-8 processor, Sigmet) might be the best solution.

5.4 Conclusion

The ground clutter return was used to test the overall phase stability of the radar as well as the quality of phase shifter. Because phase shifting is required for generation of systematic codes to mitigate range and velocity ambiguities, it was important to determine phases of the existing phase shifter. Reported test and spectral analysis demonstrated that the phase shifter is stable, but the realized phases differ systematically although slightly from the commanded phases. It was demonstrated that the ground clutter return can be used to determine exact phases for decoding that allow accomplishing up to 10 dB of SNR improvement. For the NEXRAD system the ground clutter returns obtained with a stationary antenna can be used to test the overall phase stability thus calibrating the radar and improving SNR.

6. Concluding remarks

6.1 Summary

This thesis investigates echo and spectral signatures of non-meteorological point scaterrers, particularly airplanes, birds, and ground clutter in the planetary boundary layer (PBL). It is determined that

- Airplanes
  - ✓ can be distinguished by their spectra, due to unique features corresponding to the physical specifications of each craft;
  - ✓ can be tracked by weather radars.
- Spectral signatures of birds
  - ✓ are evident even in the background wind;
  - ✓ can be used to recognize and track isolated birds at close ranges;
  - ✓ can be used for correcting bird-contaminated wind profiles;
  - ✓ do not depict the wing beating frequency.
- Spectral signatures of ground clutter
  - ✓ can be used to determine phases for decoding phase-coded data, allowing up to 10 dB SNR improvement;
  - ✓ can be used to to test overall phase stability for calibrating radar.

6.1.1. Airplanes

An airplane has features in its spectra corresponding to the physical specifications of the craft. Categories of airplanes (e.g. with or without a propeller, large or small) could be distinguished by their spectra. The simple model of an airplane

demonstrated a decent prediction of target characteristics. The TWS (track while scan) systems could probably avoid confusion caused by crossing target tracks by adding a procedure that examines spectral signatures which could possibly be associated with each individual aircraft.

Tracking a small airplane in PBL demonstrated the possibility for detection and application of weather radar for tracking non-cooperative planes. The tracking can be done using rapid consecutive scan. The airplane was easy to detect in both spectra and PPI at close ranges. Nonetheless tracking at WSR-88D volume updates rates (~5 min) might be difficult and will need association from volume scan to volume scan and might confuse airplanes with large birds or moving automobiles (from side lobe).

6.1.2 Birds

The hypothesis that a signature of beating wings would appear as a shouldered sidelobe on the bird spectra was not confirmed. The simulation demonstrated that only wing-beating frequency more then 8 Hz would be distinguishable.

Large solitary birds (e.g. hawk) isolated in flight at close ranges (about 7 km) were tracked over a considerably long period of time 2.5 minutes (rapid consecutive scan). Bird spectral signatures are evident even in the background wind, some time ground clutter, and noise. Nocturnal (e.g. passerine) birds covering 30 km range so that every resolution volume had one or few birds in it (sometimes none) were observed, and distinguished from the wind and clutter (Section 4.3).

The simple model of a bird verified the understanding of bird flight and body characteristics. Bird signatures can be observed in spectra and therefore, might be

removed with appropriate filtering techniques from the weather signals, or separated and amplified for observing bird behavior in ornithological studies.

6.1.3. Ground Clutter

A strong point ground clutter signal can serve for the radar calibration, and effective SNR improvement. The phase coded echo from a stationary point scatterer was examined to determine uncertainties in radar oscillator phase. The determined phases were used for decoding phase-coded data, allowing up to 10 dB SNR improvement.

6.2 Further Work

Outlining further work I would like to emphasize the importance of spectral analysis and the necessity to correctly identify spectral signatures for improving the interpretation of signals and procedures for data censoring. The following ideas for future work come to mind.

1. Constructing an algorithm for distinguishing and tracking airplanes with weather radars.
2. Building the airplane signatures bank.
3. Creating a filtering-enhancing technique based on the obtained spectral information, for example, a technique for correcting bird-contaminated wind profiles.
4. Spectral analysis of bird signatures needs to be supported by the ornithological data and actual observation that will help completely understand the phenomena.
5. A strong point ground clutter (e.g. radio tower) return should be investigated in different wind conditions for its vibration signature.

Bibliography

[1] Achtemeier G. L., 1990: *The Use of Insects as Tracers for "Clear-Air" Boundary-Layer Studies by Doppler Radar*. J. Atmos. Ocean. Tech., Vol. 8, pp. 746-765.

[2] Battan, L. J., 1973: *Radar Observations of the Atmosphere*. University of Chicago Press, 324 pp.

[3] Doviak, R. J. and D. S. Zrnić, 1984: *Doppler Radar and Weather Observations*. Academic Press, 458 pp.

[4] Doviak, R. J. and D. S. Zrnić, 1984: *Matched Filter Criteria and Range Weighting for Weather Radar*. IEEE Vol. AES-14, 6, 925-930.

[5] Campistron, B., 1975: *Characteristic distributions of angel echoes in the lower atmosphere and their meteorological implications*. Boundary-Layer Meteorology 9: 411-426.

[6] Larkin R.P., W.R. Evans, and R. H. Diehl, 2001: *Nocturnal Flight Calls of Dickcissels and Doppler Radar Echoes over South Texas in Spring*. J. Field Ornithol. 73(1): 2-8

[7] Larkin R.P., and R. H. Diehl, 2001: *Spectrum Width of Birds and Insects on Pulsed Doppler Radar*. Illinois Press, 20 pp

[8] Mueller E. A., and R. P. Larkin, 1984: *Insects observed Using Dual-Polarization Radar*. J. Atmos. Ocean. Tech., 2, 49-54.

[9] Mueller E. A., 1983: *Differential Reflectivity of Birds and Insects*. Edmonton, Canada. Amer. Meteor. Soc.

[10] Sachidananda, M. and D. S. Zrnić, 1999: *Systematic Phase Codes for Resolving Range Overlaid Signals in a Doppler Weather Radar*. J. Atmos. Ocean. Tech., 16, 1351-1364.

[11] Vaughn C. R., 1985: "Birds and insects as radar targets: A review," Proc. IEEE, 73, 205-227, Feb. 1985.

[12] Riley J. R., 1985: "Radar cross section of insects," Proc. IEEE, 73, 228-232, Feb.1985

[13] Rabin, R. M., R. J. Doviak, 1989: *Meteorological and astronomical influences on radar reflectivity in the convective boundary layer*. J. Appl. Meteor., 28, 1226-1235

[14] Wilczak J. M., R. G. Strauch, F. M. Ralph, B. L. Weber, D. A. Merrit, J. R. Jordan, D. E. Wolf, L. K. Lewis, D. B. Wuertz, J. E. Gaynor, S. A. McLaughlin, R. R. Rogers, A. C. Riddle, and T.S. Dye 1995: *Contamination of wind profiler data by migrating birds: Characteristics of corrupted data and potential solutions*, J. Atmos. Ocean. Tech., 12, 449-467.

[15] Wilson, J. W., Weckwerth, T. M., Vivekanandan, J., Wakimoto, R. M., Russell, R.W., 1994: *Boundary layer clear-air radar echoes: origin of echoes and accuracy of derived winds*. J. Atmos. Ocean. Tech. 11:1184-1206.

[16] Zrnić D. S, and A. V. Ryzhkov, 1998: *Observation of Insects and Birds with Polarimetric Radar*. IEEE Trans. Geosci. Remote Sens., 36, No. 2, 661-668.

[17] Zrnić D. S, and Mahapatra 1985: Two methods of ambiguity resolution in pulsed Doppler weather radars. IEEE Trans. Aerospace Electr. Syst., 21, 470-483

[18] Zrnić D. S, and M. Sachidananda, 1986: *Recovery of spectral moments from overlaid echoes in a Doppler weather radar*. IEEE Trans. Geosci. Remote Sens., 24, 751-764

[19] Personal communications with Zrnić D. S, September 2003.

Appendix

Table A1: Data 2/10. The phases, their difference, and the standard deviation for the tower

1	2	3	4	5
k	Commanded Phase (degrees)	Estimated Phase (degrees)	Difference [3]-[2] (degrees)	Standard Deviation (degrees)
1	0	0	0	0
2	-22.5	-21.5447	0.9553	0.9715
3	-112.5	-112.4008	0.0992	0.2268
4	45.0	45.0811	0.0811	0.2231
5	45.0	45.0203	0.0203	0.2124
6	-157.5	-158.4123	-0.9123	0.9307
7	112.5	111.9415	-0.5585	0.6130
8	90.0	89.8464	-0.1536	0.3178
9	90.0	89.8114	-0.1886	0.3143
10	67.5	67.9936	0.4936	0.5508
11	-22.5	-21.4976	1.0024	1.0250
12	135.0	134.4742	-0.5258	0.5919
13	135.0	134.4190	-0.5810	0.6464
14	-67.5	-66.5753	0.9247	0.9724
15	-157.5	-158.4108	-0.9108	0.9536
16	180.0	178.9186	-1.0814	1.1069
17	180.0	178.8632	-1.1368	1.1770
18	157.5	156.8656	-0.6344	0.7031
19	67.5	68.0014	0.5014	0.5848
20	-135.0	-135.3065	-0.3065	0.4071
21	-135.0	-135.3887	-0.3887	0.4643
22	22.5	22.5191	0.0191	0.2909
23	-67.5	-66.5941	0.9059	0.9549
24	-90.0	-88.9298	1.0702	1.1082
25	-90.0	-88.9571	1.0429	1.0714
26	-112.5	-112.4027	0.0973	0.2450
27	157.5	156.9293	-0.5707	0.6324
28	-45.0	-44.0539	0.9461	0.9916
29	-45.0	-44.0982	0.9018	0.9469
30	112.5	112.0190	-0.4810	0.5570
31	22.5	22.5154	0.0154	0.2738
32	0	0.0237	0.0237	0.3144
33	0	0.0226	0.0226	0.3281
34	-22.5	-21.5263	0.9737	1.0189
35	-112.5	-112.4115	0.0885	0.3150
36	45.0	45.0769	0.0769	0.2941
37	45.0	45.0144	0.0144	0.3234
38	-157.5	-158.4388	-0.9388	1.0009
39	112.5	111.9217	-0.5783	0.6772
40	90.0	89.8152	-0.1848	0.3973
41	90.0	89.8135	-0.1865	0.3930
42	67.5	67.9805	0.4805	0.6320
43	-22.5	-21.4864	1.0136	1.0925
44	135.0	134.4600	-0.5400	0.6614
45	135.0	134.4071	-0.5929	0.6957
46	-67.5	-66.5765	0.9235	0.9878
47	-157.5	-158.3987	-0.8987	0.9699
48	180.0	178.9430	-1.0570	1.1221
49	180.0	178.8859	-1.1141	1.1809
50	157.5	156.9017	-0.5983	0.7130
51	67.5	68.0369	0.5369	0.6566
52	-135.0	-135.2968	-0.2968	0.5187
53	-135.0	-135.3857	-0.3857	0.5786
54	22.5	22.5291	0.0291	0.4014
55	-67.5	-66.5886	0.9114	0.9872
56	-90.0	-88.9195	1.0805	1.1516
57	-90.0	-88.9111	1.0889	1.1587
58	-112.5	-112.3874	0.1126	0.4264
59	157.5	156.9397	-0.5603	0.6939
60	-45.0	-44.0765	0.9235	1.0064
61	-45.0	-44.1269	0.8731	0.9581
62	112.5	111.9904	-0.5096	0.6679
63	22.5	22.4851	-0.0149	0.4469
64	0	0.0042	0.0042	0.4309
rms			0.67	0.74

Table A2: Data 4/02. The phases, their difference, and the standard deviation for the tower

1	2	3	4	5
k	Commanded Phase (degrees)	Estimated Phase (degrees)	Difference [3]-[2] (degrees)	Standard Deviation (degrees)
1	0	0	0	0
2	-22.5	-21.6502	0.8498	1.0168
3	-112.5	-112.5322	-0.0322	0.8747
4	45.0	44.9247	-0.0753	0.9080
5	45.0	44.8409	-0.1591	1.0216
6	-157.5	-158.3160	-0.8160	1.1928
7	112.5	111.8618	-0.6382	0.8921
8	90.0	89.6101	-0.3899	0.7225
9	90.0	89.5985	-0.4015	0.9218
10	67.5	67.9115	0.4115	1.0932
11	-22.5	-21.5697	0.9303	1.3523
12	135.0	134.6499	-0.3501	1.0598
13	135.0	134.6559	-0.3441	0.8732
14	-67.5	-66.6952	0.8048	0.9891
15	-157.5	-158.2264	-0.7264	1.0485
16	180.0	179.4035	-0.5965	1.1815
17	180.0	179.3872	-0.6128	1.2441
18	157.5	157.5204	0.0204	1.0694
19	67.5	67.9358	0.4358	1.0265
20	-135.0	-135.3983	-0.3983	0.8502
21	-135.0	-135.5324	-0.5324	0.7974
22	22.5	22.4569	-0.0431	0.8598
23	-67.5	-66.7793	0.7207	1.3241
24	-90.0	-88.9767	1.0233	1.4689
25	-90.0	-89.0676	0.9324	1.4246
26	-112.5	-112.4897	0.0103	0.7895
27	157.5	157.5255	0.0255	0.6232
28	-45.0	-44.1145	0.8855	1.0925
29	-45.0	-44.1513	0.8487	1.2340
30	112.5	111.9338	-0.5662	1.1560
31	22.5	22.4896	-0.0104	1.0692
32	0	0.0712	0.0712	1.0482
33	0	0.0720	0.0720	0.8603
34	-22.5	-21.6160	0.8840	1.0813
35	-112.5	-112.4401	0.0599	0.7932
36	45.0	44.9536	-0.0464	0.9936
37	45.0	44.9263	-0.0737	1.0499
38	-157.5	-158.3122	-0.8122	1.3720
39	112.5	111.8961	-0.6039	1.1900
40	90.0	89.6116	-0.3884	0.8695
41	90.0	89.5824	-0.4176	0.7221
42	67.5	67.9500	0.4500	0.9156
43	-22.5	-21.5791	0.9209	1.3501
44	135.0	134.6690	-0.3310	1.1045
45	135.0	134.5944	-0.4056	1.1461
46	-67.5	-66.7499	0.7501	1.1810
47	-157.5	-158.3387	-0.8387	1.1453
48	180.0	179.3656	-0.6344	0.9764
49	180.0	179.3462	-0.6538	1.1105
50	157.5	157.5235	0.0235	0.9635
51	67.5	67.9379	0.4379	1.1017
52	-135.0	-135.4104	-0.4104	0.9962
53	-135.0	-135.4908	-0.4908	0.9109
54	22.5	22.4261	-0.0739	0.5446
55	-67.5	-66.7692	0.7308	1.0182
56	-90.0	-89.0160	0.9840	1.3502
57	-90.0	-89.0271	0.9729	1.4073
58	-112.5	-112.5126	-0.0126	1.0583
59	157.5	157.5697	0.0697	0.9504
60	-45.0	-44.1322	0.8678	1.2019
61	-45.0	-44.1961	0.8039	1.1101
62	112.5	111.8796	-0.6204	1.1339
63	22.5	22.4296	-0.0704	1.0875
64	0	0.0624	0.0624	1.0493
		rms	0.57	1.06

Table A3: Summary for data 2/10 and 4/02. Phases are in degrees.

1	2	3	4	5
k	Commanded Phase (degrees)	Estimated Phase 030210 (degrees)	Estimated Phase 030402 (degrees)	Difference [3]-[4] (degrees)
1	0	0	0	0
2	-22.5	-21.5447	-21.6502	0.1055
3	-112.5	-112.4008	-112.5322	0.1313
4	45.0	45.0811	44.9247	0.1564
5	45.0	45.0203	44.8409	0.1794
6	-157.5	-158.4123	-158.3160	-0.0963
7	112.5	111.9415	111.8618	0.0797
8	90.0	89.8464	89.6101	0.2362
9	90.0	89.8114	89.5985	0.2129
10	67.5	67.9936	67.9115	0.0821
11	-22.5	-21.4976	-21.5697	0.0721
12	135.0	134.4742	134.6499	-0.1757
13	135.0	134.4190	134.6559	-0.2368
14	-67.5	-66.5753	-66.6952	0.1199
15	-157.5	-158.4108	-158.2264	-0.1844
16	180.0	178.9186	179.4035	-0.4849
17	180.0	178.8632	179.3872	-0.5240
18	157.5	156.8656	157.5204	-0.6548
19	67.5	68.0014	67.9358	0.0656
20	-135.0	-135.3065	-135.3983	0.0918
21	-135.0	-135.3887	-135.5324	0.1436
22	22.5	22.5191	22.4569	0.0621
23	-67.5	-66.5941	-66.7793	0.1852
24	-90.0	-88.9298	-88.9767	0.0469
25	-90.0	-88.9571	-89.0676	0.1105
26	-112.5	-112.4027	-112.4897	0.0871
27	157.5	156.9293	157.5255	-0.5962
28	-45.0	-44.0539	-44.1145	0.0606
29	-45.0	-44.0982	-44.1513	0.0532
30	112.5	112.0190	111.9338	0.0852
31	22.5	22.5154	22.4896	0.0258
32	0	0.0237	0.0712	-0.0475
33	0	0.0226	0.0720	-0.0494
34	-22.5	-21.5263	-21.6160	0.0897
35	-112.5	-112.4115	-112.4401	0.0285
36	45.0	45.0769	44.9536	0.1233
37	45.0	45.0144	44.9263	0.0880
38	-157.5	-158.4388	-158.3122	-0.1266
39	112.5	111.9217	111.8961	0.0256
40	90.0	89.8152	89.6116	0.2036
41	90.0	89.8135	89.5824	0.2311
42	67.5	67.9805	67.9500	0.0305
43	-22.5	-21.4864	-21.5791	0.0928
44	135.0	134.4600	134.6690	-0.2090
45	135.0	134.4071	134.5944	-0.1873
46	-67.5	-66.5765	-66.7499	0.1733
47	-157.5	-158.3987	-158.3387	-0.0600
48	180.0	178.9430	179.3656	-0.4226
49	180.0	178.8859	179.3462	-0.4603
50	157.5	156.9017	157.5235	-0.6217
51	67.5	68.0369	67.9379	0.0990
52	-135.0	-135.2968	-135.4104	0.1136
53	-135.0	-135.3857	-135.4908	0.1052
54	22.5	22.5291	22.4261	0.1030
55	-67.5	-66.5886	-66.7692	0.1806
56	-90.0	-88.9195	-89.0160	0.0965
57	-90.0	-88.9111	-89.0271	0.1160
58	-112.5	-112.3874	-112.5126	0.1251
59	157.5	156.9397	157.5697	-0.6300
60	-45.0	-44.0765	-44.1322	0.0557
61	-45.0	-44.1269	-44.1961	0.0692
62	112.5	111.9904	111.8796	0.1108
63	22.5	22.4851	22.4296	0.0555
64	0	0.0042	0.0624	-0.0582
			rms	0.23